



**This electronic thesis or dissertation has been  
downloaded from Explore Bristol Research,  
<http://research-information.bristol.ac.uk>**

*Author:*

**Gillespie, Calum**

*Title:*

**Optical control of electrostatic actuators using amorphous silicon**

**General rights**

Access to the thesis is subject to the Creative Commons Attribution - NonCommercial-No Derivatives 4.0 International Public License. A copy of this may be found at <https://creativecommons.org/licenses/by-nc-nd/4.0/legalcode>. This license sets out your rights and the restrictions that apply to your access to the thesis so it is important you read this before proceeding.

**Take down policy**

Some pages of this thesis may have been removed for copyright restrictions prior to having it been deposited in Explore Bristol Research. However, if you have discovered material within the thesis that you consider to be unlawful e.g. breaches of copyright (either yours or that of a third party) or any other law, including but not limited to those relating to patent, trademark, confidentiality, data protection, obscenity, defamation, libel, then please contact [collections-metadata@bristol.ac.uk](mailto:collections-metadata@bristol.ac.uk) and include the following information in your message:

- Your contact details
- Bibliographic details for the item, including a URL
- An outline nature of the complaint

Your claim will be investigated and, where appropriate, the item in question will be removed from public view as soon as possible.



**This electronic thesis or dissertation has been  
downloaded from Explore Bristol Research,  
<http://research-information.bristol.ac.uk>**

*Author:*  
**Gillespie, Calum**

*Title:*  
**Optical Control of Electrostatic Actuators using Amorphous Silicon**

**General rights**

Access to the thesis is subject to the Creative Commons Attribution - NonCommercial-No Derivatives 4.0 International Public License. A copy of this may be found at <https://creativecommons.org/licenses/by-nc-nd/4.0/legalcode>. This license sets out your rights and the restrictions that apply to your access to the thesis so it is important you read this before proceeding.

**Take down policy**

Some pages of this thesis may have been removed for copyright restrictions prior to having it been deposited in Explore Bristol Research. However, if you have discovered material within the thesis that you consider to be unlawful e.g. breaches of copyright (either yours or that of a third party) or any other law, including but not limited to those relating to patent, trademark, confidentiality, data protection, obscenity, defamation, libel, then please contact [collections-metadata@bristol.ac.uk](mailto:collections-metadata@bristol.ac.uk) and include the following information in your message:

- Your contact details
- Bibliographic details for the item, including a URL
- An outline nature of the complaint

Your claim will be investigated and, where appropriate, the item in question will be removed from public view as soon as possible.

# Optical Control of Electrostatic Actuators using Amorphous Silicon

By  
Calum Gillespie



Department of Aerospace Engineering  
UNIVERSITY OF BRISTOL

A dissertation submitted to the University of Bristol in accordance with the requirements of the  
degree of Doctor of Philosophy in the Faculty of Engineering.  
September 2021

Word Count: 42535

## Abstract

Research in the field of soft robotics has looked to develop compliant devices which integrate methods of control and sensing into the body of the device. The aim of this PhD research is to reduce the need for traditional electrical componentry and increase the overall compliance of the robot. In this thesis the use of amorphous silicon (a-Si) as a functional material with electrostatic actuators is presented. The semiconductor properties of a-Si allow it to provide methods of optical activation of electrostatic actuators such as dielectric elastomer actuators (DEAs).

In this work methods of fabricating a-Si are developed using a clean room facility to create solid state devices that can be used with soft robotic actuators. Various characterisation techniques have been explored including, scanning electron, atomic force microscopy and ellipsometry, to evaluate the fabrication process of a-Si. In addition, characterisation of the electrical and photonic properties of a-Si are presented to help inform the electrical response of a-Si at high voltage as well as the design of optically controlled actuators.

Initial development of an optically controlled dielectric elastomer actuator (DEA) using a-Si is presented and optical control of a DEA actuator with a voltage swing of 865V across the DEA was achieved from increasing light intensity, leading to recorded displacements of 2.2 $\mu\text{m}$ . It was also demonstrated that the optically controlled DEA showed repeatability in actuation as well as low latency of response.

The optically controlled DEA was developed to generate larger displacements under different light intensities by exploiting unstable wrinkling of the DEA membrane. The onset of unstable wrinkling of a DEA design was investigated and used to develop an optically controlled DEA that has the potential to achieve larger displacement changes between ambient and illuminated states by transitioning between stable and unstable actuation. The use of this DEA membrane geometry allowed for increases in actuation of 16% between ambient and illuminated states. Although wrinkling of the optically controlled DEA was not observed due to saturation of the driver electronics output, predictions of the applied voltage range required to achieve this actuation window are presented. As well as opportunities for potential designs of active DEA windows and a DEA eye that could exploit the optical control methods presented.

A compliant electrostatic zipping actuator that integrated a-Si as an active electrode was fabricated using thin film deposition of a-Si onto a flexible polyimide (Kapton) substrate. In contrast to the optically controlled DEA, the a-Si was fully embedded in the actuator structure. The a-Si zipping actuator showed a maximum change in curvature of 0.007 $\text{mm}^{-1}$  between ambient and illuminated



lighting conditions. The compliant a-Si zipping actuator was shown to have increases in displacement of up to 300% in a simple harmonic oscillator conformation. The a-Si oscillator achieved larger change in displacement by exploiting changes in light intensity to move the simple harmonic oscillator from a low to high displacement mode.

This thesis demonstrates the first steps in developing actuators that demonstrate novel methods of optical control of compliant actuators through the use of a-Si, reducing the need for conventional wired control systems.

## Acknowledgments

I would like to take this opportunity to thank my supervisors. Andrew Conn and Jonathan Rossiter who have been there for me both academically and personally over the course of my research providing expertise and help week in and week out. I could not have asked for a better support network for this project. I would also like to thank Fabrizio Scarpa for always keeping the project going in the right direction and Asier Marzo who's undying enthusiasm allowed for this project to become a reality.

I would also like to thank the technical staff at both the Bristol Robotics Laboratory and the Clean room who provided essential support throughout my research. A warm thank you to my colleagues in the Soft lab for making my PhD experience so enjoyable.

I would like to acknowledge the Engineering and Physics Research Council for their support through the ACCIS CDT program.

Finally, I would like to thank my parents, Wilma and Keith, who's never ending support and love has allowed me the opportunity to pursue my passions.

## Covid-19 Mitigation statement.

The COVID-19 pandemic had a significant impact on this thesis. The work covered in this thesis was almost entirely experimental and the lab closures and restrictions had a significant impact on research. The impact of the COVID-19 pandemic on this thesis include:

- Access to specialised lab facilities – high voltage testing.
- Access to specialised finite element analysis software - Comsol multiphysics.
- Closure of specialist fabrication facilities – Cleanroom.
- Further experimental work to demonstrate onset of wrinkling of a dielectric elastomer actuator with the use of an a-Si switch.
- Experimental work to develop working demonstrators of integrated a-Si actuators. Such as the active blinds and deployable structures.

Where possible the use of numerical methods and extrapolation from results taken prior to the pandemic have been used as an alternative to this experimental work. However, these are not direct substitutes for the experimental work that was planned. Further details of the future work surrounding these impacted areas of study are discussed in Chapter 7 of this thesis.

## Author Declaration

I declare that the work presented in this thesis was conducted in accordance with the requirements of the University of Bristol's regulations and code of practice for research degree programs. The work presented in this thesis has not been submitted for any other academic award. Work done with the assistance or collaboration with others is indicated. The work is the candidate's own work. Any views and opinions expressed in this thesis are those of the author.

SIGNED:..........

DATE: 15/9/21

# Table of Contents

<i>Abstract.....</i>	<i>i</i>
<i>Acknowledgments.....</i>	<i>iii</i>
<i>Covid-19 Mitigation statement.....</i>	<i>iv</i>
<i>Author Declaration .....</i>	<i>v</i>
<i>List of acronyms .....</i>	<i>ix</i>
<i>Chapter 1 Introduction .....</i>	<i>1</i>
1.1 Motivation .....	1
1.2 Research Questions .....	2
1.3 Contributions .....	2
1.4 Publications .....	3
1.5 Thesis outline .....	3
<i>Chapter 2: Literature review.....</i>	<i>5</i>
2.1 Introduction .....	5
2.2 Soft and compliant actuators.....	7
2.3 Dielectric elastomer Actuators .....	9
2.4 Dielectrophoretic liquid zipping (DLZ).....	11
2.5 PEANO HASEL .....	13
2.6 Tuneable flexible and resilient robots driven by electrostatic actuator .....	14
2.7 Functional materials.....	16
2.8. Wireless control .....	23
2.9 Emerging research opportunities.....	25
2.10 Summary .....	26
2.11 Conclusions .....	28
<i>Chapter 3: Manufacturing, Experimental Methods and Characterisation.....</i>	<i>29</i>
3.1 Introduction .....	29
3.2 Amorphous Silicon .....	30
3.3 Manufacture method of a-Si.....	31
3.4 Microscopy of a-Si .....	33

3.5 Ellipsometry .....	37
3.6 Characterising the electrical response of a-Si at low voltage .....	40
3.7 Characterising the electrical response of a-Si at high voltage.....	42
3.8 SEM images post breakdown .....	53
3.9 Numerical modeling of A-Si .....	55
3.10 Characterisation Summary .....	61
3.11 Conclusion.....	62
<i>Chapter 4: Control of dielectric elastomer actuators using amorphous Silicon .....</i>	<i>63</i>
4.1 Introduction .....	63
4.2 Dielectric elastomer actuators.....	64
4.3 Development of an optically controlled DEA with a-Si .....	71
4.3.1 Methodology.....	72
4.3.3 Quasistatic tuning of the voltage swing across the DEA.....	74
4.4 Results.....	77
4.5 Discussion .....	77
4.6 Conclusions .....	79
<i>Chapter 5: Improving the actuation of an optically controlled DEA using wrinkling. ....</i>	<i>80</i>
5.1 Introduction .....	80
5.2 DEA Wrinkling.....	81
5.3 Wrinkling of an aperture DEA .....	83
5.4 Exploiting wrinkling in an optically controlled DEA .....	89
5.5 Conclusions .....	94
<i>Chapter 6 a-Si Kapton actuator.....</i>	<i>96</i>
6.1 Introduction .....	96
6.2 Manufacturing of a-Si thin films.....	98
6.3 A-Si cantilever.....	100
6.4 Manufacturing of a-Si cantilever actuator.....	101
6.5 Image processing .....	102
6.6 Results.....	105
6.7 Discussion .....	107

6.8 a-Si Kapton oscillator.....	108
6.9 Future applications.....	113
6.10 Conclusions .....	115
<i>Chapter 7: Conclusions and future work.....</i>	<i>117</i>
7.1 Conclusion.....	117
7.2 Discussion and future work .....	120
<i>References .....</i>	<i>123</i>
<i>Appendix.....</i>	<i>130</i>
Appendix A: ITO ramp test .....	130
Appendix B: Figure 4.2 Experimental method.....	131
Appendix C: High frequency testing of wrinkling DEAs .....	131

## List of acronyms

**a-Si** – Amorphous Silicon

**DEA** – Dielectric elastomer actuator

**MOSFET** – Metal oxide semiconductor field effect transistor

**SMA** – Shape memory alloy

**DLZ** - Dielectrophoretic liquid zipping

**HASEL** – Hydraulically amplified self-healing electrostatic actuator

**EAP** – Electro active polymer

**VHB** – Very high bonding

**PZT** – Lead zirconate titanate

**LDR** – Light dependent resistor

**SEM** – Scanning electron microscope

**AFM** – Atomic force microscope

**PECVD** – Plasma enhanced chemical vapour deposition

**ITO** – Yttrium tin oxide

**LED** – Light emitting diode

**DAQ** – Data acquisition device

**PCB** – Printed circuit board

**PVC** – Poly-vinyl chloride



# Chapter 1 Introduction

In biological systems there are several environmental responses that are involuntary. In the case of humans these include the dilation of pupils in response to light and the contraction of muscles in response to pain. These responses utilise methods of triggering actuation that circumvent the typical neural pathways. In soft robotics, actuator responses can be controlled by external systems that vary the outputs of the actuator by an input control signal. In this work photo-responsive amorphous silicon (a-Si) is used to provide a method of transducing changes in resistance from applied light. A change in the electrical resistance of a-Si in response to changes in light intensity is used to enable remote activation of robotic actuators and to explore potential methods for their environmental responsiveness. In this thesis, the manufacturing and characterisation of a-Si will be presented and used to inform the development of light responsive electrostatic actuators.

## 1.1 Motivation

There is a motivation to integrate control into soft robotic actuators using functional materials rather than relying on external circuitry. This could lead to robotic devices with increased compliance as well as a degree of autonomy with regards to actuation. The field of soft robotics is targeting the development of new actuators with increased functionality whilst still maintaining an overall compliant structure. This can lead to the robot having the desired functionality whilst reducing the overall complexity of the system, which allows for greater overall compliance. Currently, to control a system of actuators several external electrical components are required such as a microcontroller, relays and MOSFETs. These electrical components are not soft or compliant enough to be directly integrated into an actuator design. To achieve a compliant actuator design, functional materials can be used to provide methods of switching using external energy sources.

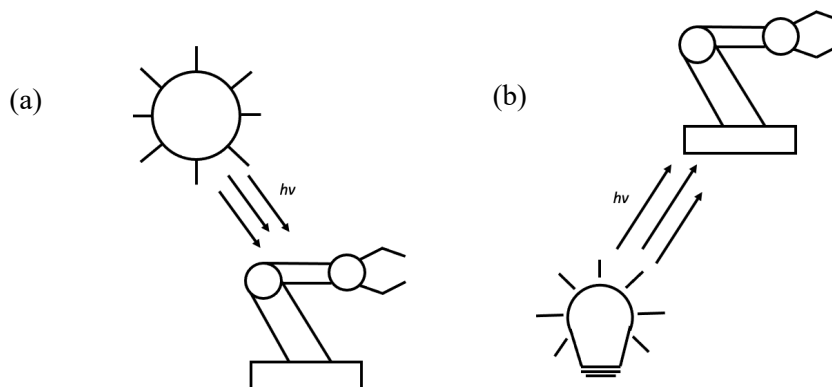


Figure 1.1: (a) Environmental stimulus used to control an optically functional soft robotic actuator. (b) Remote artificial stimulus used to control an optically functional soft robotic actuator.

The resistance response of a-Si from the change in light intensity can be separated into two potential methods of activation of a soft robotic actuator. The first is using changes in the environmental light intensity to provide the stimulus to trigger actuation of the device as seen in figure 1 (a), allowing a device to adapt to its environment. Alternatively, remote methods of stimulus could be used, such as a handheld light source, to trigger the optically functional actuator shown in figure 1 (b), providing a method of wireless control. These two approaches to control an actuator could lead to applications including environmentally triggered deployable structures and remote control of soft robotic devices in areas that are hazardous to humans such as those encountered during search and rescue.

## 1.2 Research Questions

This thesis explores the characterisation and development of a-Si as a functional material in robotic actuators. We look to exploit material properties to provide novel alternatives to traditional activation methods for electrostatic actuators, where integrated and compliant solutions are desired. In order to tackle this task, there are a number of questions that must be addressed:

- How can functional materials be manufactured to be used with existing electrostatic actuators actuator designs?
- Can a functional material such as a-Si cope with the high voltage requirements of electrostatic actuators?
- How can we use the photo resistive characteristics of a-Si for actuator applications?
- What is the potential control available through the use of a-Si as a photo-resistive element?
- How can a-Si be integrated into a compliant actuator design?

This thesis will focus on using a-Si as a functional material and investigating its potential benefits to the research field of soft robotic actuators. Initial characterisation of a-Si within the context of actuator applications will be conducted, then methods of using a-Si alongside existing electrostatic actuators will be explored before finally developing an integrated concept for an optically activated electrostatic actuator using a-Si.

## 1.3 Contributions

In answering the research questions above, the following contributions have been made to the soft robotics field:

- A characterisation of the electrical and photonic properties of a-Si within the context of actuator applications.
- The development of a-Si as a solid-state photo-resistive unit with a high voltage electrostatic actuator.

- Generating increases in actuation from a dielectric elastomer actuator using changes the resistance in a-Si through changes in light intensity.
- Increase the magnitude of output from an optically controlled dielectric elastomer actuator by exploiting wrinkling instabilities to generate a snap through response.
- Integrate a-Si into a stand-alone actuator design
- Demonstrate separation of power and control signals using a-Si.

#### 1.4 Publications

The following papers were published during this research.

1. Gillespie, C., Marzo, A., Scarpa, F., Rossiter, J. & Conn, A. T., 26 Apr 2020, Switching of amorphous silicon thin-film actuators for optically functional robotic devices. *Proceedings of the SPIE, Electroactive Polymer Actuators and Devices (EAPAD) XXII*. Society of Photo-Optical Instrumentation Engineers (SPIE), Vol. 11375. 113751O (2020)
2. Gillespie, C., Marzo, A., Scarpa, F., Rossiter, J. & Conn, A., 4 Apr 2019, High-voltage photonic switching of dielectric elastomers with amorphous silicon thin-films. *Electroactive Polymer Actuators and Devices (EAPAD) 2019*. Washington, USA: Society of Photo-Optical Instrumentation Engineers (SPIE), Vol. 10966. 109661Z. (Electroactive Polymer Actuators and Devices (EAPAD); vol. 10594).

#### 1.5 Thesis outline

The structure of this thesis is described below:

- Chapter 2 introduces the state of research in the field of soft robotics actuators and where this thesis fits within that research space. A number of different examples of functional materials in soft robotics literature are discussed, as well as background theory on amorphous silicon and electrostatic actuators.
- Chapter 3 presents methods of manufacturing amorphous silicon (a-Si) components and characterisation of the manufacturing process through microscopy. The low and high voltage responses of a-Si are presented and compared to a light dependent resistor. Finally, numerical modelling is used to establish the photonic response of a-Si from the characterisation data presented in the chapter and used to predict the theoretical change in resistance of a-Si at increased light intensities.

- Chapter 4 demonstrates the use of a-Si as a solid-state photo-resistive component in series with a dielectric elastomer actuator (DEA). Manufacturing of the actuator and optimisation of the electrical circuitry are presented alongside experimental testing and analysis of the results.
- Chapter 5 builds on the observations of the a-Si and DEA testing to develop methods of exploiting the onset of wrinkling instabilities in DEA membranes to achieve increased actuation from an actuator in series with a-Si. In this chapter the onset of wrinkling for a controlled DEA geometry is established and then tested using the change in resistance of a-Si to trigger this onset. Analysis of the results are made, and a hypothesis is developed as to how this can be improved in future work.
- In chapter 6 methods of manufacturing thin films of a-Si on flexible polyimide (Kapton) substrates are explored. This flexible thin film is then used in a standalone electrostatic zipping actuator. The theory of electrostatic zipping is discussed as well as remote analysis of actuation using image processing of video frames. Testing of the a-Si electrostatic cantilever design is presented as well as an oscillator design that uses a weighted a-Si driven pendulum to achieve larger displacements through switching in and out of higher displacement oscillation with changes in light intensity.
- Chapter 7 concludes the thesis by collating the research contributions made in this work and presents potential areas in which future work can be conducted.

## Chapter 2: Literature review

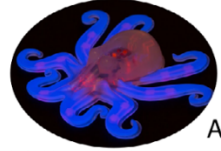
### 2.1 Introduction

Functional materials are defined as materials that exhibit properties other than mechanical load bearing capabilities. They can provide a large range of responses which can be exploited to create functional devices [1]. Within the field of actuators, functional materials have been utilised to create actuators which can convert external stimulus into dynamic actuation [2]. There is a hope that functional materials can also provide methods of control for soft and compliant actuators.

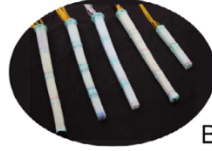
Typically, control of actuators can be achieved using conventional electronic components such as relays and metal oxide semiconductor field effect transistors (MOSFET) which are widely available and used in conventional robotic devices. There are two ways in which a functional material can be used alongside an actuator. It can either be in a ‘solid state’ electrical component, synonymous with conventional electronics such as the aforementioned MOSFETs, or used as an integrated component of the actuator design. The former benefits from the easier implementation with pre-existing actuator technologies whereas integration will require significant consideration of the actuator design and may affect the performance. There are emerging opportunities to use functional materials to provide alternative methods of control to electronic components. This has the benefit of easier integration into an actuator design and can therefore help to maintain the softness or compliance desired for soft robotic applications.

An important distinction to make for this review is the difference between softness and compliance and how they are implemented in the soft robotics field. Softness is a material property that refers to the resilience to indentation or scratching, whereas compliance relates to how stiff a material or section is. Compliance can be engineered whereas softness is an inherent property of the materials used. This is often misconstrued in the field of soft robotics, with compliant robots being described as soft. There are a few papers that look to establish a definition for the field [3][4] and a simple tier system defining the ‘softness’ of robotic devices is proposed ranging from tier 1 (conventional robots) to tier 4 (entirely soft robots). See figure 2.1 for an outline of a proposed tier system for soft robotic designs.

**Tier 4** - Entirely soft robots, independent of any hard elements.



**Tier 3** - Entirely soft robots relying on external hard components.



B



C



D

**Tier 2** - Robots with primary functions fully or partially achieved through soft elements making up a significant portion of their body.



E



F



G

**Tier 1** - Conventional robots modified to achieve compliance actively through controlled joint impedance or passively through compliant structural elements.



H



I

Figure 2.1: Proposed tiers of softness for robotic design. Reproduced from [3]. Images of different examples are given for each tier. A [5], B [6], C [7], D [8], E [9], F [10], G, H [11], I [12].

There is a drive amongst research to develop tier 4 robots that are entirely soft to maximise the benefits that soft materials bring, such as robustness (higher impact resistance due to the soft nature of the materials used) and being able to interact with fragile or sensitive objects such as soft grippers for medical applications. As will become apparent over the course of this chapter, many of the current state of the art soft robotic actuators would be defined as tier 2-3. This is because they rely on conventional electronic components to aid with the control of actuation or to supply power to the device. Therefore, there is an opportunity to exploit the properties of functional materials to reduce the reliance on rigid electronic components and move towards tier 4 soft robotics. One of the benefits of using functional materials to provide wireless control whilst maintaining wired power is increased efficiencies from the wired power supply. This can also increase the overall compliance as wireless control could reduce the number of onboard components. In the future there could be scope to implement wireless power in such devices to improve their overall compliance.

With the drive of soft robotic research towards more compliant designs for actuators the potential opportunity to use functional materials as a means of providing methods of control has been established, whilst potentially increasing the compliance of the overall actuator. In this chapter the literature surrounding the three key areas of functional materials, compliant actuators and soft robotics will be considered. The design space for this thesis can be represented by a Venn diagram of these three research areas in figure 2.2.

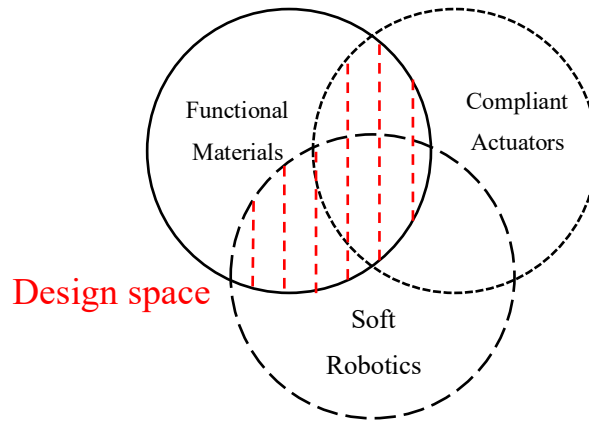


Figure 2.2: Venn diagram showing the key areas of research and the novel design space targeted by this thesis.

In this chapter we look to review the state of the art for each of the research fields highlighted in figure 2.2. Figure 2.2 also shows the design space in which this research focuses, at the intersections of functional materials, compliant actuators and soft robotics. The literature from each of the research areas will be discussed, highlighting potential opportunities for novel research.

## 2.2 Soft and compliant actuators

Soft and compliant actuators are a subset of actuators used in the robotics field. They are usually fabricated from materials that are inherently soft or flexible. These range from electrostatic actuators such as dielectric elastomer actuators (DEA) [13] to shape memory alloys [14] and pneumatic actuators such as the McKibben artificial muscled [9], [15]. One of the attractions of these actuators is their large work output relative to their weight (specific energy), making them comparable in some cases to mammalian skeletal muscle. This provides a huge benefit to the field of robotics research as there is a growing push towards lightweight, robust and powerful actuators over conventional mechanical actuators such as servos and stepper motors.

Table 2.1: Commonly-used soft and compliant actuators and their key properties

Property	Skeletal muscle[13]	Dielectric elastomer[13]	Ferroelectric polymers[13]	Conducting Polymers[13]	NiTi Shape Memory Alloys[13]	DLZ*[16]	PEANO HASEL[17]
Strain (%)	20-40	10-100	3-10	2-12	1~8	99.84	18
Stress (MPa)	0.1-0.35	0.1-2 typical, 3-9 maximum	20-45	1-100	200	0.04077	6
Work density (kJ/m <sup>3</sup> )	8-40	10-150 typical, 3400 maximum	1000	70-100	>1000	44.17	
Density (kg/m <sup>3</sup> )	1037	~1000	2000	1300	6450		
Strain rate (%/s)	>50	450 in VHB, 34 000 in silicone	>2000 at 0.1% strain	1-12	300	1985	890
Continuous power (W/kg)	50-280	~500	>1000	150	>1000	103.41	50
Electromechanical coupling (%)	<40	30 typical, 90 maximum	10-40	<10	<5		
Cycle life	>10 <sup>9</sup>	106 at 50% strain		800 000 best to date	300 at 5%, 107 at 0.5%	<1000	20000
Modulus (MPa)	10-60	0.1-3	400-1200	500	20 000-80 000	190000	
Voltage (V)	<1V**	>1000	1000	2	Low	5-8K	8-13K
Softness Tier	2	3	3	2	2	2	3

\*Actuator configuration was optimised for stress and strain

\*\* Voltage applied to skeletal muscle is a control signal and does not provide power for actuation.

### 2.2.1 Work density comparison

Work density is a means of comparing actuators by their specific mechanical output. Considering the actuators compared in table 2.1, it can be seen that shape memory alloys (SMA) have the highest work density. SMAs such as NiTi have low response frequency which can limit their applications. A plot of the typical actuator force as a function of response speed is shown in the figure 2.3.



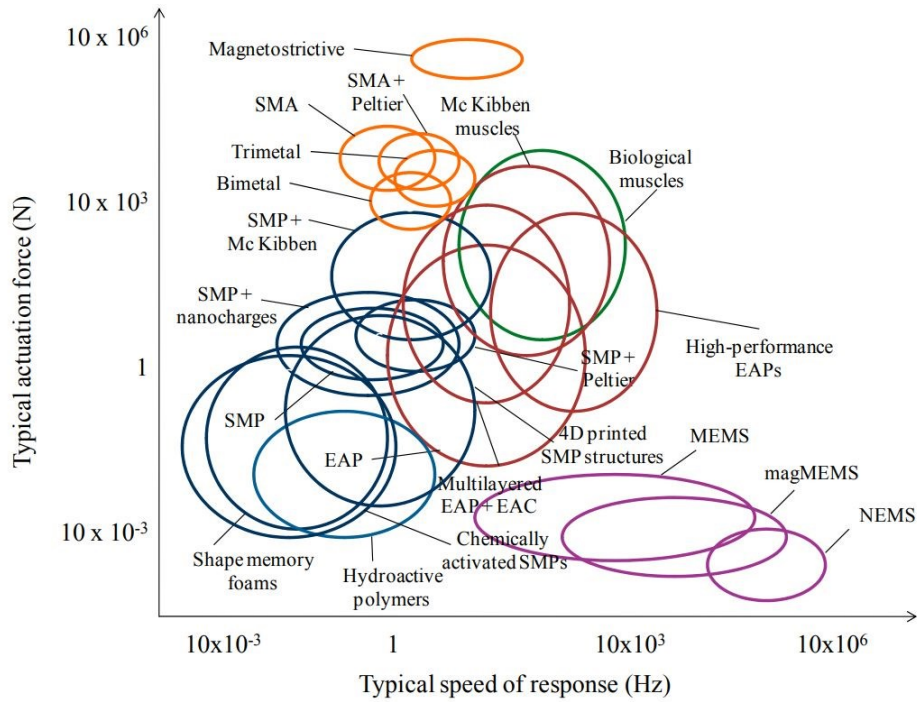


Figure 2.3: Plot of actuator force as a function of speed of response for a range of typical actuators. Reproduced from [18].

As can be seen from figure 2.3, high force actuators such as shape memory alloys (SMA) and magnetostrictive materials have considerably slower response speeds compared to biological muscle which can be used as a base line for comparison for effective soft and compliant actuators. Therefore, this suggests that high performance electroactive polymers (EAPs) could provide a good starting point for integrating functional materials as they already share similar output metrics to the base line biological muscle.

### 2.3 Dielectric elastomer Actuators

Electrostatic actuators use high electrical charges between two electrodes to develop a motive force between them. Electrostatic actuators such as electro active polymers (EAP) use dielectric materials such as silicon oil and acrylic based 3M VHB (very high bonding) tape. Materials with high dielectric constants are used to increase the dielectric field between the two opposing actuator plates and thus increase force of the actuator due to the increase in Maxwell pressure [13]. Currently one of the factors limiting the force output of these actuators is the relatively low dielectric constant of ‘soft’ dielectric materials. These actuators exhibit a number of capacitor effects such as charging, discharging and energy storage, which can lead to promising opportunities for electrostatic actuators to act as sensors as well as energy harvesters. There are a number of examples of the electrostatic modeling of electroactive polymers with varying degrees of complexity [19]. Most commonly found in literature are dielectric elastomer actuators (DEA) which show high specific force outputs and have potential for both self-sensing and energy harvesting applications [20] [21].

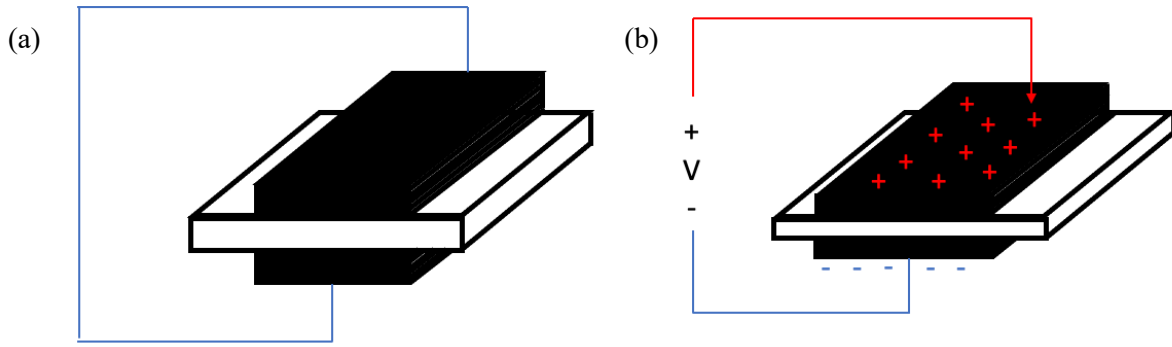


Figure 2.4: (a) Schematic of a DEA with no applied voltage. (b) Schematic of a DEA under applied voltage.

Dielectric elastomer actuators (DEAs) are a class of electrostatic actuators that are capable of producing high strains and can be engineered to achieve multiple degrees of freedom [22]. As shown in the schematic in figure 2.4 the DEA has two compliant electrodes that are separated by the dielectric elastomer membrane. A potential is applied across the electrodes generating an electric field dependent Maxwell pressure,  $P$ , highlighted in figure 2.4 (b), which generates a through thickness compression of the pre-strained dielectric elastomer membrane [13],

$$P = \epsilon_r \epsilon_0 (V/T)^2. \quad (1)$$

The Maxwell pressure equation for a DEA is shown in equation (1) where  $\epsilon_r$  is the relative permittivity of the DEA,  $\epsilon_0$  is the permittivity of free space,  $V$  is the applied voltage across the DEA and  $T$  is the thickness of the DEA membrane. Typical electric fields applied across the DEA are of the order of  $100\text{V}/\mu\text{m}$ , which for DEAs with thicknesses in the order of  $10\text{s of } \mu\text{m}$ , leads to a typical operational voltage of between 1 and  $10\text{kV}$ . The maximum operational voltages are limited by the dielectric breakdown strength of the elastomer, since too high a voltage can lead to dielectric breakdown of the actuator as well as arcing between the actuator and closely placed conductive materials. Some designs have been shown to operate with voltages as low as  $300\text{V}$  by reducing the membrane thickness to  $3\mu\text{m}$  through a pad-printing fabrication technique [23]. Getting the operational voltages of DEAs to similar voltages as other actuators such as piezoelectric devices would allow the use of industrially available electronic components to be drive DEA technologies.

DEAs have been designed in numerous versatile configurations, notable examples of which include; (i) stacked DEAs which provide large out of plane displacements [24] and (ii) conical designs which have been used to demonstrate antagonistic movements that can be used to create DEA pump designs

[25][26] as well as devices with multiple degrees of freedom [27]. There are opportunities with DEAs for a large variety of actuator configurations to achieve a wide range of responses to suit multiple engineering applications.

#### 2.4 Dielectrophoretic liquid zipping (DLZ)

Alongside DEAs, the state of the art in the electrostatic actuator field also includes novel actuators centered around electrostatic zipping. Electrostatic zipping actuators focus on two electrodes separated by an insulating material [28].

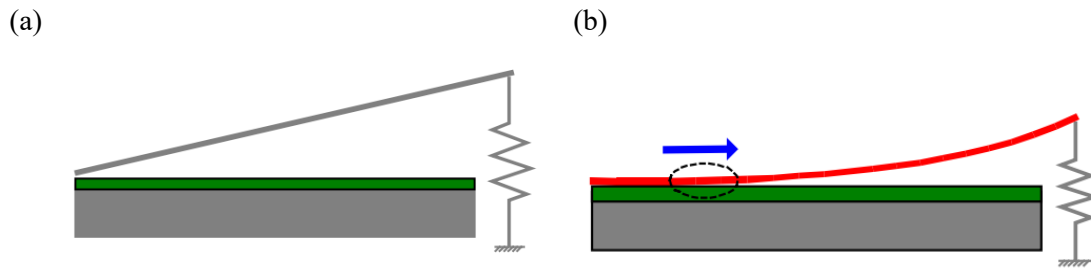


Figure 2.5: A schematic of a zipping actuator (a) before applied voltage and (b) after a voltage has been applied. The grey areas represent the electrodes and green area is the separating dielectric.

Reproduced from M. Brenner et al. [28]

The electrodes are held together at a ‘zippering point’ as shown in figure 2.5 (a) and under an applied field across the electrodes the zippering point will move along the two electrodes as they become attracted to one another as shown in figure 2.5 (b). This can be approximated by considering the electrodes as a number of interstitial point sources separated by a distance,  $r$ , and charged uniformly ( $q_1 = -q_2$ ). When considering the electrostatic forces between each point charge it can be assumed that there is no interaction between neighboring charges.

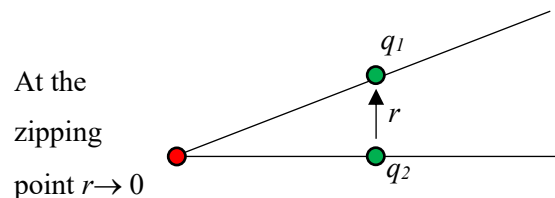


Figure 2.6: Diagram showing a simplified point charge model for an electrostatic zipper and governing equation.

Figure 2.6 shows a model of the electrostatic forces between two point charges in an electrostatic zipper. In this model it is assumed that neighboring charges do not interact. The force between the two point charges,  $q_1$  and  $q_2$  can be represented by Coulomb’s law,

$$F = K \frac{q_1 q_2}{r^2}. \quad (2)$$

Where  $F$  is the closing force,  $q_1$  and  $q_2$  are the point charges,  $r$  is the distance between the charges and  $K$  is the Coulomb constant. The electrostatic force is dependent on the inverse square of the distance between the electrodes at any given point along the zipper. At the zipping point the force is at its maximum, which causes the electrodes to pull together and thereby move the zipping point along the two electrodes. This in turn reduces the distance between the electrodes, therefore increasing the electrostatic force until the zipper fully closes. Electrostatic zipping is a well-established method of actuation [29][30], in recent years there have been novel designs to improve the force output of these style of actuators by implementing dielectrophoretic effect in the case of the electro-ribbon actuators proposed by Majid Taghavi et al. [16]. The actuator features two steel shim electrodes separated by a polyvinyl chloride (PVC) insulating layer. On the application of an electrostatic field the two electrodes are attracted to one another due to their opposite charged and the electrodes ‘zip’ together from the corners of the actuator. This actuator uses dielectrophoretic liquid in the corner of the zipping region to increase the zipping force by a theoretical maximum of 120-fold by amplifying the field effects at the zipping point [16]. This allowed an example actuator to produce a force of 12.91N, with a maximum contraction of 99.84%. The highest energy density achieved was  $44.17 \text{ kJ m}^{-3}$  which is comparable to mammalian skeletal muscle, when optimised for each configuration.

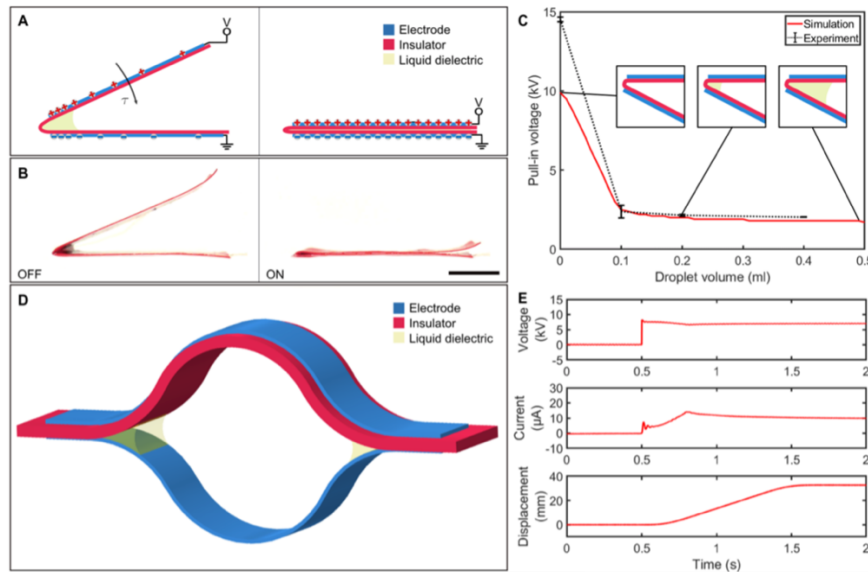


Figure 2.7: Electro-origami (A) and electro-ribbon actuator (D) concept. (B) Photographs of actuated electro-origami fold. (C) Effect of droplet volume on pull-in voltage for a zipping electro-origami fold. (D) Diagram of electro-ribbon actuator. (E) Voltage, current, and displacement during isotonic actuation of an electro-ribbon actuator. (reproduced from [16])

Figure 2.7 shows the fabrication and operation of the DLZ actuator and plots of the effect of the droplet volume on the pull in voltage of the actuator and the voltage, current and displacement plots of the actuator in use. The DLZ actuator has a very high specific power which makes it extremely attractive for robotic applications. This unique design allows for relatively simple fabrication techniques in comparison to those of DEA actuators, demonstrated in [16] by the fabrication of a DLZ actuator using paper and graphite pencil electrodes, since all that is required is a compliant electrode and insulating material. The simple and compliant base components of the actuator also open up opportunities for unique multi-actuator designs such as the grippers, cilia and locomotive robot demonstrated in [16]. The potential for folded origami actuators creates ample opportunities for novel research alongside work in engineering origami [31], such as deployable solar cells and other aerospace structures where specific force is a desired characteristic. However, the use of dielectric fluid to increase the closing force creates a unique challenge in trying to keep the fluid in place for repeated actuations.

## 2.5 PEANO HASEL

An electrostatic actuator design that solves the issue of encapsulation of the dielectric fluid (a challenge for the DLZ actuator) is the PEANO hydraulically amplified self-healing electrostatic actuator (HASEL) [17]. This actuator consists of repeating units of rectangular pouches of flexible and inextensible polypropylene polymer film filled with dielectric fluid and heat sealed. Electrodes are placed either side of the dielectric fluid pouches and separated by the polypropylene films. This encapsulation of dielectric fluid can be thought of as a fluidic capacitor.

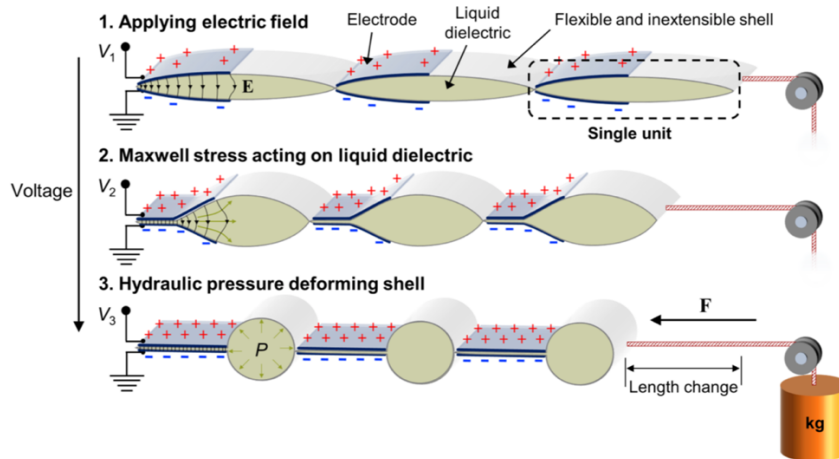


Figure 2.8: Schematic diagram of the cross-section of a Peano-HASEL actuator. Multiple actuators can be produced in series to increase the force output. Reproduced from [17].

Figure 2.8 shows a schematic diagram of the HASEL actuator which operates when an applied voltage of the order of 8 kV is applied across the liquid dielectric pouches. Due to the increase in Maxwell stress, the liquid dielectric is forced out from between the electrodes where it deforms the polypropylene

shell from an elliptical to circular cross section. This generates a global linear contraction much akin to that of muscle contractions. One difficulty for this actuator design is strain limitations due to the geometry of the polymer pouches. As the film pouches are limited by the final circular cross section there is a finite limit to the theoretical effective strains which this actuator can produce (~36%). Although more publications by the group has focussed on improving the effective strain response [32] and blocking force [32], the HASEL actuator show extremely high stress of 6MPa and it is easily implementable in engineering applications due to its encapsulated design.

## 2.6 Tuneable flexible and resilient robots driven by electrostatic actuator.

A more recent publication which explores electrostatic actuators was on a tunable flexible robot by Jin et al. [33]. The actuator was found to deform by 68% of its height, using electrostatic attraction between two Kapton layers with gold deposited electrodes separated by an insulating layer. This is very similar to the morphology of the DLZ actuator by Majid Taghavi et al., this work does not exploit dielectrophoretic effects to increase the closing force. This reduces the maximum output of the actuator however it increases the practicality of the design by removing the need for a dielectric fluid. One electrode is pre buckled which provides the restoring force for the actuator after the voltage is removed. Frequencies achieved where in the range of 5-40Hz for locomotion with speeds of 40 mm<sup>s</sup> in both crawling and turning. Lower operational voltages of 500V-1kV where utilised in comparison to the electrostatic zipping actuators previously mentioned in this chapter.

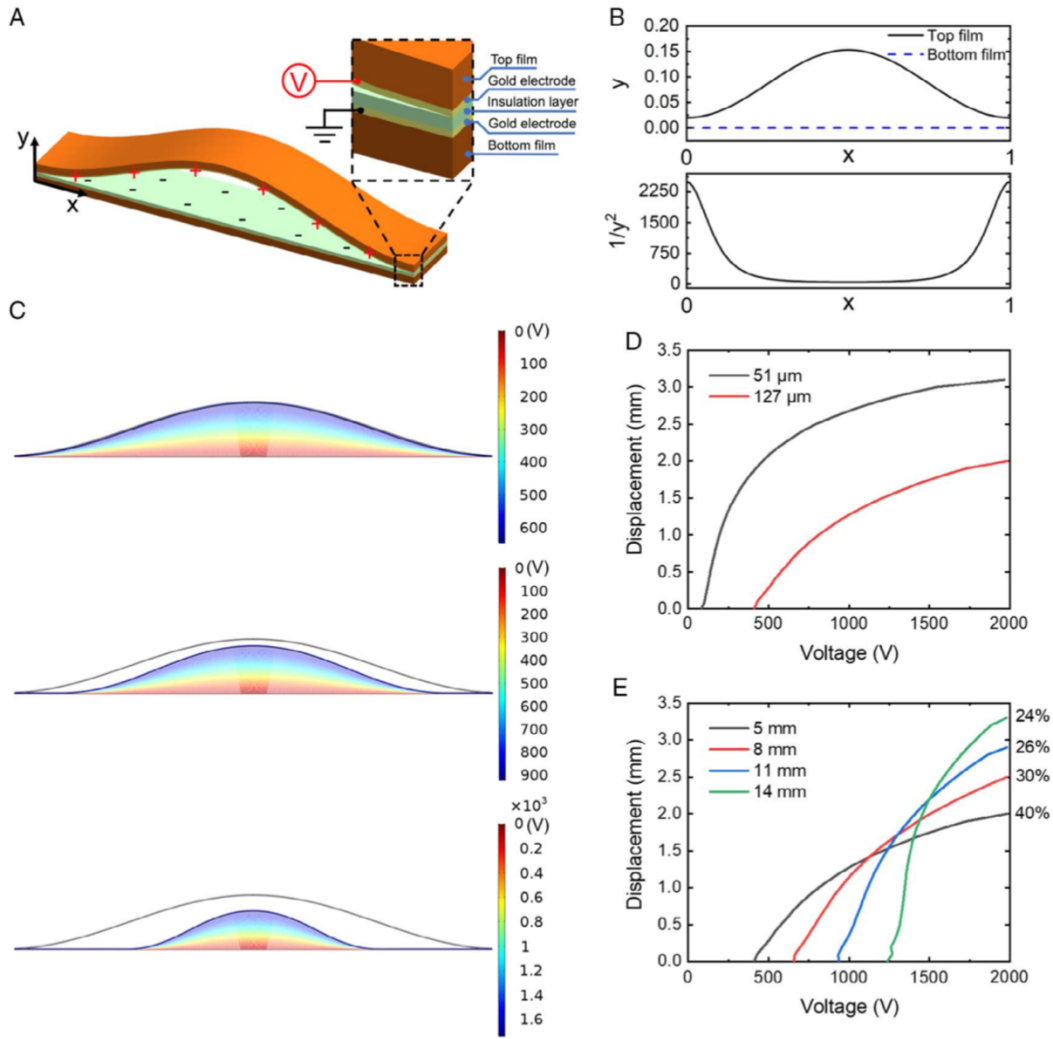


Figure 2.9: A) 3D model of the zipping actuator. B) Top: cross-section schematic of the actuator, bottom: electrostatic force. C) COMSOL model showing the voltage field between the top and bottom layers during contraction. D) Displacement of the centre point on the top film for top layers of two different thicknesses E) Displacement of the centre point of the top film for actuators of differing heights, with the relative traveling distances as a percentage. Reproduced from [33]

As can be seen from figure 2.9 above, finite element analysis (COMSOL) was used to create a model of the actuator which couples the electrical and mechanical responses of the device. This provides a solid basis of understanding the voltage distribution during compression of the actuator. This work does not mention issues with the actuator returning to its unactuated state. The Kapton substrate used is a polyimide with a high molecular density which has been noted in literature to have a high polarisability [34]. This can lead to unexpected effects during actuation such as the ‘kicking’ of the origami wings of the DLZ/Kapton actuator proposed by Taghavi et al [16], or slow ‘peel off’ time due to residual electrostatic forces between the polyimide (Kapton) support material. This effect may have had a lesser impact in this work due to the lower actuation voltage, 500V, in comparison to the DLZ actuator. This actuator shares a lot of the simplicities of fabrication that come from a compliant zipping actuator like

the DLZ. This reduction in complexity could provide an opportunity for the integration of functional materials in a compliant zipping actuator to further help push these devices into the higher tiers of soft and compliant robotic design.

## 2.7 Functional materials

Functional materials can be thought of as a transducer i.e., converting one type of energy into another such as an electrical signal. Methods of transduction include optical, thermal and mechanical. Functional materials are materials that exhibit novel properties, such as piezoelectric, electromagnetic and photovoltaic responses. The novel properties of functional materials could provide opportunities for research in the field of soft robotic actuators as they can provide a convenient method of transduction of energy. This transduced energy can then be used as an input signal to provide novel methods of control for the actuator. In this section we will discuss a number of functional materials to explore their potential with soft robotic actuators.

*Piezoelectric - Materials that generate internal electric charge from the application of mechanical stress. Conversely the application of electrical charge to the material can create a mechanical stress or displacement.*

*Electromagnetic/magnetic – Materials that produce a magnetic field in response to an electrical current. Magnetic materials are ones which can be polarised by a magnetic field.*

*Photovoltaic – Materials that generate an electrical charge from the application of energy in the form of light. Different materials can respond to different wavelengths of light.*

*Shape memory alloys (SMA) – are materials which can be mechanically deformed and then will return to their original conformation on the application of thermal energy.*

### 2.7.1 Piezoelectric

Piezoelectrics have been shown to provide the core of some compliant actuator designs [35], [36]. The Piezoelectric effect stems from the material's crystal structure, where the central charged atom in the Perovskite unit cell of the material can be controllably offset from oppositely charged surrounding lattice. This offset can either lead to a mechanical stress or an electrical charge across the lattice depending on whether electrical or mechanical stimulus is used.



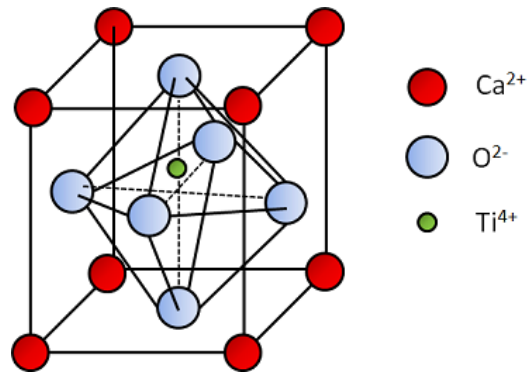


Figure 2.10: Diagram of the Perovskite unit cell with offset  $\text{Ti}^{4+}$  ion. Reproduced from [37].

Figure 2.10 shows the typical Perovskite unit cell of a piezoelectric material. Piezoelectric materials have been used as stand-alone actuators and are typically they are used in engineering situations where precise consistent movements are required [35]. Due to the nature of the piezoelectric effect, the displacement for a given voltage is small (of the order of  $100\mu\text{m}$  to  $1\text{mm}$  strokes) and this can be improved by stacking several layers of piezoelectric material together to achieve greater displacements [38].

The ability to stack piezo actuators means that they can span a number of length scales and avoid the scaling issues that other actuators face. This is important to consider when evaluating functional materials for actuator devices. Certain functional responses are most suited to certain actuation types, and they can perform extremely well at smaller length scales such as in micro electromechanical systems (MEMS) but are challenging to scale up to large sized devices. It is important to consider the application of the actuator when trying to evaluate the most beneficial functional material to integrate into the actuator.

Piezoelectric materials are typically ceramics which are brittle, leading to issues with regards to compliant devices. In compliant piezoelectric actuators the compliance is generated by the mechanism geometry rather than the inherent material properties [39]. From classical beam theory, the bending stiffness of a beam is dependent on both thickness and material stiffness [40]. Therefore, materials with a higher material stiffness can be used in compliant structures if the thickness of the section is sufficiently small. There is potential for piezoelectric materials in compliant actuators, however due to their hardness they are unlikely to meet the needs of soft applications. A common design in the literature is a lead zirconate titanate (PZT) bimorph, this comprises of laminated thin layers of PZT ceramic which can be actuated separately to create a bending moment [35], [36] These bimorph configurations have been shown to have self-sensing characteristics [35].

A major difficulty facing the use of piezoelectric materials is one of environmental safety. The best performing ceramics typically contain lead, which poses potential hazards to health if the material breaks down. This could pose difficulties in some soft or compliant actuators which are designed to operate in a natural environment to undertake a desired task and then be left to breakdown or be recycled [41].

### 2.7.2 Electromagnetic materials

Electromagnetic materials are easily polarisable by an applied magnetic field, and they fall into two classes, hard and soft magnetic materials. The magnetic dipoles in a hard-magnetic material are fixed in position and form a permanent magnet. Soft magnetic materials have dipoles that are free to move and orientate with magnetic fields and are typically found in electromagnetic devices. Electromagnetic materials can lead to extremely precise control of implantable medical devices such as drug delivery modules [42]. Groups such as Bradley J. Nelson's have used ferro magnetic material in the design of structures such as artificial bacteria flagella [43]. The ferro magnetic materials are controlled by using a series of electromagnetic coils.

The response of electromagnetic materials has been controlled using 3D printing technology to deposit electromagnetic composite materials with their magnetic polarisation manipulated by the application of an electromagnetic field during deposition and curing [44]. This allows for complex displacements and out-of-plane movements from extremely small untethered devices [44][45]. In work by Yoonho Kim et al., printing of these ferromagnetic domains in a controlled manner allowed for the designs shown in figure 2.11 [44].

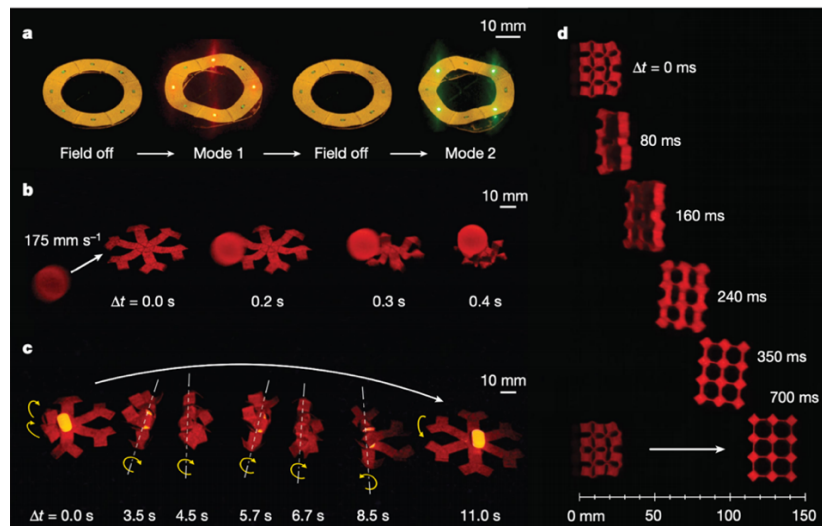


Figure 2.11: 3D printed ferromagnetic structures by Kim et al.: (a) a reconfigurable annular ring (b) hexapedal structure that can stop a fast-moving object (c) controlled rolling of the hexapedal structure (d) horizontal leap of a 3D auxetic structure. Reproduced from [44].

Despite having a large amount of localised control at the millimeter length scale, it can be argued that the use of the term untethered in [44] is slightly misleading because the soft devices demonstrated in figure 2.11 require large and bulky external electromagnets to achieve the precise control. This restricts the applications of the devices to localised tasks such as drug deliver and other medical applications where the range of the device is limited to a fixed region leading to restrictions in the design space. However, this branch of soft robotic research is one of the few that in the current state of the art can achieve tier 4 devices, which are both compliant and untethered.

### 2.7.3 Shape memory alloys (SMA)

Shape memory alloys (SMA) are materials that can be deformed and then revert to their original shape with thermal energy. Heating the SMA leads to deformation that can be reversed through mechanical stress.

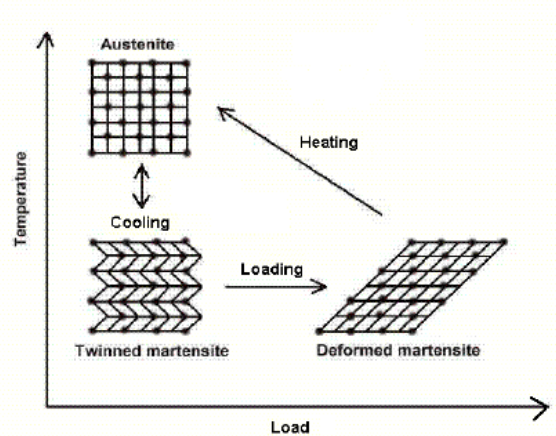


Figure 2.12: Diagram showing the phase transformations of typical SMA materials under different load and temperature conditions. Reproduced from [46].

Figure 2.12 shows the phase transformation of a typical SMA material. In SMA materials, applied loading causes the material atomic crystal structure to ‘twin’ between two different martensitic phase structures. When the material is heated, it is taken to an austenitic phase, shown in figure 2.12, which with stored mechanical stress returns the material back to the original martensitic phase. This process is repeatable indefinitely.

SMA's have been used extensively in compliant actuators. Typically, as wires they can provide axial contraction which can be easily encapsulated in a soft structure such as silicone [47] or braided fibrous sleeves [48][14]. With localised heating or segmented actuator elements, SMA actuators have found success in ‘inchworm’ actuators for locomotion. Mencias et al. have published a number of papers on this design looking at the biological model of an earthworm as the inspiration for the SMA actuator

[47][49][50]. This design used a three-wire module that allowed for contraction and bending of the soft shell which contained several hook-like feet to provide sufficient friction to allow for locomotion. It is important to note that the design also includes several heat sinks to allow for sufficient thermal transfer. This may be a draw-back of using SMA materials due to insufficient thermal regulation leading to poor hysteresis effects.

One difficulty in using thermal energy in the control of an actuator is fidelity of response due to the nature of the phase transformation mechanism. Temperature transitions occur within a range of temperatures and can be impacted greatly by the environment as well as the surrounding material's thermal properties, leading to variability in cooling rates. SMAs and other thermally transitioning materials operate best in a binary switching mode, having an 'on' and 'off' displacement which can be switched between through heating and cooling. This enables bi-stable actuator designs that require energy input in order for the actuator to 'snap through' to a different stable energy configuration. Examples of this are bimorph structures and pump valves [51]. One disadvantage of SMAs is the high currents required to actuate, which can cause practical difficulty in situations where large numbers of actuators are to be used in a system. Alongside this, their slow actuation speed limits their applications in the field of soft robotics with high frequency actuation such as muscle responses difficult to replicate.

#### 2.7.4 Photovoltaic

Photoactive materials exhibit the photovoltaic effect: an electrical voltage is produced across the bulk of the material when exposed to photons. Typically, this response is most commonly seen in semiconducting materials [52]. Semiconducting materials that exhibit this effect have been used in a wide number of electronic devices that are used extensively in industry in both low and high voltage applications such as light dependent resistors, photovoltaic cells and optoisolators.

Light dependent Resistors (LDRs) are electrical components that provide variable resistances with changes in applied light intensity. Examples in robotics include line tracking and phototaxis [53]. They primarily consist of a photo-resistive ceramic material, such as cadmium selenide/telluride and zinc oxide [53], and two electrodes. Ceramic powders can be deposited as thin ceramic films; however, without significant additives ceramics are typically brittle, and suffer the same limitations highlighted with piezoelectric materials in section 3.1. This is important when selecting materials to implement in actuator devices as additives will need to be used to achieve the desired compliance.

Semiconducting materials, the most common of which is silicon also exhibit photovoltaic responses. Typically doping is used to provide a range of electrical and photonic properties. There are three categories of commercially available silicon; single crystal, arranged polycrystalline and amorphous.

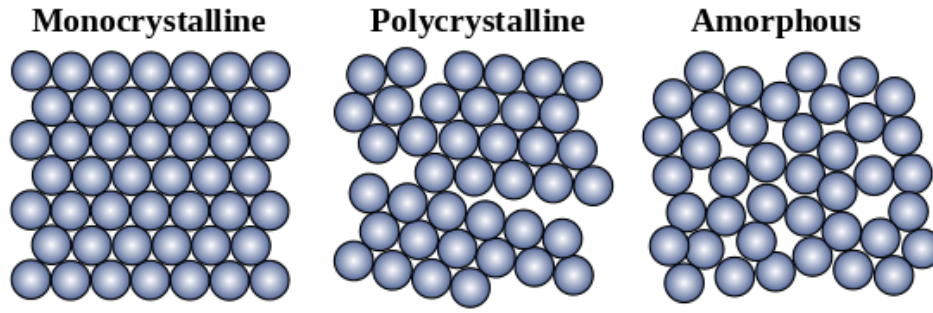


Figure 2.13: Diagram showing the different crystalline structures of Silicon [54].

The different forms of commercial silicon are shown in figure 2.13. Amorphous, polycrystalline and monocrystalline silicon vary by having increasing amounts of randomized grain structure, from monocrystalline to amorphous. Amorphous silicon has the lowest manufacturing cost and are often found in small solar powered electronic devices.

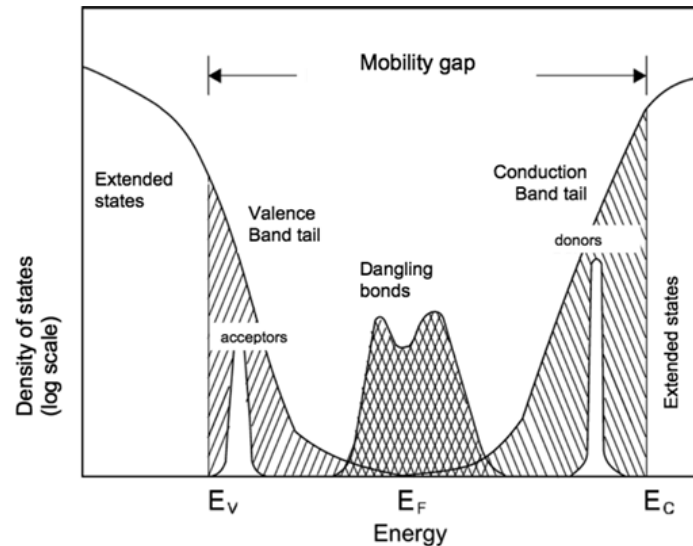


Figure 2.14: Diagram of the electron energy levels and band gap for amorphous silicon (reproduced from [55]).

Amorphous silicon (a-Si) has no long-range orientation of the crystal grain structure rather than being a truly amorphous material [10]. In semiconductor materials the electrons sit in energy levels. These levels are grouped together to form energy bands, the bands for a-Si are shown in figure 2.14. The valence band is at a lower energy and the conduction band at a higher energy level where the electrons are free to move and conduct. The difference in energy between the valence and conduction band is known as the mobility gap and in semiconducting materials this is proportional to the wavelength of photons. This means that when photons with sufficient energy ( $h\nu$ ) are absorbed by the material the electrons in the valence band are excited energetically and are promoted to the higher energy conduction band where they are free to move and conduct. In some semiconducting materials impurities such as

hydrogen can provide dangling bonds which are found in the energy levels between the valence and conduction band. This can provide an intermediate site for recombination of electrons before promotion to the conduction band and a lower energy pathway to the extended states where electron transport occurs. Materials with an increased number of dangling bonds include hydrogenated amorphous silicon. The availability of free moving electrons in the a-Si structure has been reported in the literature to lead to a “short ambipolar electron diffusion length of less than 115nm” [56]. Therefore, a-Si should be responsive to optical stimulus with enough sensitivity to allow for conduction localised to the area of stimulus, as seen in the narrow wave guides in [57].

Semiconductor materials are atomically ‘doped’ with impurities to have more donor impurities (n type) and acceptor impurities (p type). Semiconductors are used to create a variety of electronic equipment using a p-n junction such as photovoltaic cells. In a photovoltaic cell the energy from the incoming photons is sufficient to allow for electron mobility across the p-n junction, producing an electrical current. These devices can also be reverse biased by applying a voltage across them [58]. This serves to bias the p-n junction so that the electrons are forced away from the junction itself making it difficult for recombination to occur across the junction and therefore the photovoltaic cell behaves analogously to a resistor. The controllable resistance achieved from reverse biasing a p-n junction has the potential to provide control in the context of actuated devices. There are several instances of the use of reversed biased solar cells in literature [59] as well as reverse biasing being a method for treating solar cells to improve efficiencies [58] however the potential use of reverse biasing as a method of controlling an actuator is yet unexplored.

Some of the actuators discussed in section 2.2 require high voltages to achieve actuation such as DEAs. In these cases, consideration to the configuration of a functional material in relation to the high voltage supply would need to be made in order to provide potential control methods. For a semiconductor to be used in series with a high voltage actuator the semiconductor would need to provide sufficient resistance to avoid electrical breakdown. If a sufficiently high resistance change from the application of light to a semiconductor material is also achievable, then there is the potential opportunity for these materials to be used in series with high voltage actuators such as DEAs. An example of commercially available semiconductor electronics that is designed for use with high voltage is the class of optoisolators sometimes referred to as optocouplers. Optoisolators use semiconductor materials to isolate circuits from high voltage supplies by using the high inherent resistance of the semiconductor material. This resistance can be lowered by sending light signals to the optoisolator. This shows that semiconductors can be in high voltage (1-5kV) applications and supports the potential opportunity for research on the use of semi conducting materials to provide control for electrostatic actuators.

## 2.8. Wireless control

Control systems can be separated into two methodologies, centralised and de-centralised control [60]. Centralised control schemes involve a central unit which receives all state feedback signals and determines the control signal for each actuator [61]. De-centralised control uses localised sensory and feedback information to directly control actuators. De-centralised control avoids a single point of failure but relies on emergent system-level behavior, which may be less stable and reliable [61]. It is proposed in this work that functional materials can provide integrated points of interaction between neighboring actuators in a system to allow for the implementation of de-centralised control between multiple soft actuators.

Separating control signals from the power supply lines has a major benefit for actuators that require high voltages. Electrostatic actuators such as dielectric elastomer actuators (DEA) and electrostatic zippers show very high strokes but require high voltages to operate as discussed in section 2.4. Currently the most common way to activate and de-activate these actuators is to use a high voltage MOSFET or by separating the control signal from the main power by using a combination of step down and step-up transformers and sufficient insulation such as optoisolators. The latter poses the risk of increasing the noise of the control signal and both options require significant use of rigid electronic components. This causes a large constraint on the design of compliant or soft structures as these rigid components counteract the benefits of such a design approach and therefore current soft robotics systems tend to fall into the lower tier 2 and 3 softness proposed in figure 2.1.

Wireless control can also be referred to as ‘remote’ control where a known signal is transmitted and received to activate an actuator. This would be beneficial in remote locations or hostile environments such as search and rescue. Wireless power transfer is also possible (e.g. induction charging) but the focus here is on the control signal. The use of functional materials can also benefit the integration of control mechanisms in actuators helping the drive towards more compliant and untethered devices. This can be done using the transducer properties of functional materials to convert a stimulus into a measurable output signal without the need for external componentry, which limit the compliance of the system.

### 2.8.1 Phototaxis

Phototaxis is a form of locomotion where devices are either attracted to or repelled from a light source. This type of taxis occurs in nature when organisms optimise orientation to light sources for various reasons such as the case of photosynthesis in plants, but this effect is also seen in some insects [62] and jellyfish [63]. There are opportunities to use functional materials to potentially emulate phototaxis. Examples of phototaxis in soft robotic devices include an autonomous soft actuator driven by phototaxis to allow for self-locomotion [64]. This opens opportunities for deployable devices such as active lenses

[65] and solar cells which can follow the sun [66] with opportunities for autonomous control through the use of light.

### 2.8.2 Soft computing

The ‘Soft matter computer’ by Garrad *et al.* is an example of integrated alternatives to wired control signals for actuators and other soft robotic devices [67]. In this work a soft computational mechanism was developed using a conductive fluidic receptor (CFR) which responded to a conductive saltwater fluid being passed through capillaries at controlled intervals. Control of the conductive fluid spacing allows for a Turing complete soft computer which can be configured to perform several computational operations. Another example of creating logic with soft devices is work done by Nemitz *et al.* in which a method of creating non-volatile memory was proposed using a bistable soft robotic pump [68]. This system can store binary information states even if the systems pressure is disrupted. Both this work and the work by Garrad *et al.* show a very exciting opportunity to integrate logic into soft structures without requiring rigid electrical components.

### 2.8.3 Example of wireless control in soft robotics

Functional materials have already been implemented in soft robotic design, an example of which is the innervated adaptive fully soft robot [69]. This actuator design uses a thermally responsive carbon doped liquid crystal elastomer controlled by a silicon photodetector to allow for complex actuation with multiple degrees of freedom. The liquid crystal elastomer composite bimorph deforms due to the generation of heat from a flexible heating element. This was used in an inchworm design to create a compliant robot device. Photodetector were was used to show a compliant robot with autonomous control of locomotion through sensing environmental changes [69]. Different wavelengths of light (red and green) were used to stimulate the Si photodetectors on the compliant robot which allowed for simultaneous control of different areas of the actuator, leading to locomotion.



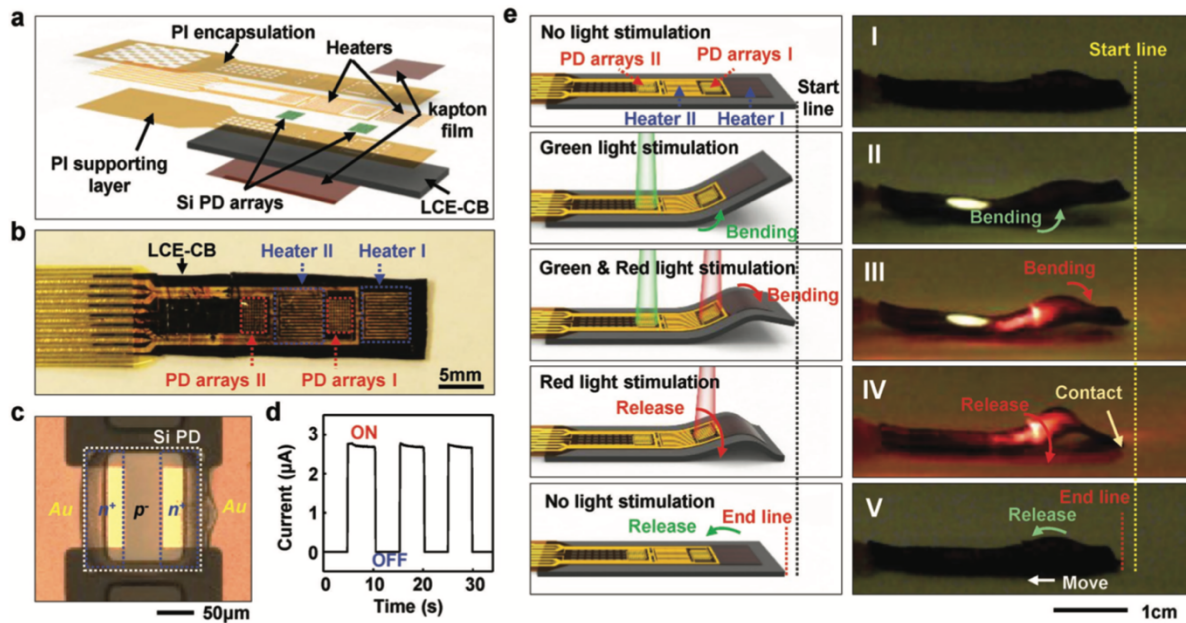


Figure 2.15: Sensing and response of an adaptive compliant robot: a) exploded view. b) The adaptive compliant robot. c) Microscope image of a Si photodetector. d) Dynamic photoelectrical response of the Si photodetector array. e) The compliant robot in locomotion. Reproduced from [69].

The use of an optical stimulus for the control of different areas of a compliant actuator is a very exciting area of control to explore within the field of robotics. Light as a mode of control has a number of parameters that can be varied including intensity, wavelength and frequency. This gives the potential to simultaneously control multiple actuators by exploring methods of stimulating functional materials, such as the silicon used in the compliant actuator shown in figure 2.15, with differing controlled parameters of light.

## 2.9 Emerging research opportunities

In this chapter the state of the art for several different actuator types has been explored. Electrostatic actuators such as the DEA, DLZ and HASEL designs show high achievable strains and adaptable conformations that lend themselves to compliant actuator designs. By looking at the literature for these electrostatic actuators we can establish the emerging research opportunities for novel control. In table 2.2 a number of commonly used electrostatic actuators are listed with the associated method of control and control signal type seen in literature.

Table 2.2: Commonly used electrostatic actuators and associated methods of control.

Actuator	Electronic control signal	Photonic control signal	Centralised control	De-centralised control
DLZ [16]	Controlled voltage signal	Research Gap	Frequency and amplitude of applied voltage provides power and control	Research Gap
HASEL [17]	Controlled voltage signal			
Electrostatic zipper [33]	Applied voltage			
DEA [13]	Controlled voltage signal			
Innervated adaptive soft robot [69]	N/A	Controlled wavelength of light	N/A	Applied voltage and optical control separated.

From table 2.2 it is clear that there is a gap in research using photonic signals to control the majority of commonly used electrostatic actuators as well as an opportunity to research the use of de-centralised control methods for electrostatic actuators. Therefore, it is proposed that the research gap that this thesis will address is the use of photonic control signals to provide methods of de-centralised control for electrostatic actuators. In this thesis we will explore the use of functional semiconducting materials to provide a means of switching electrostatic actuators with photonic stimuli.

## 2.10 Summary

There are a number of different actuator methods reviewed in this chapter which could aid in the progress of the field of soft robotics. Electrostatic actuators serve as a strong starting point for potential novel integration of functional materials due to the actuator's potential for self-sensing, allowing for complimentary integration alongside functional materials and the development of de-centralised control methods.

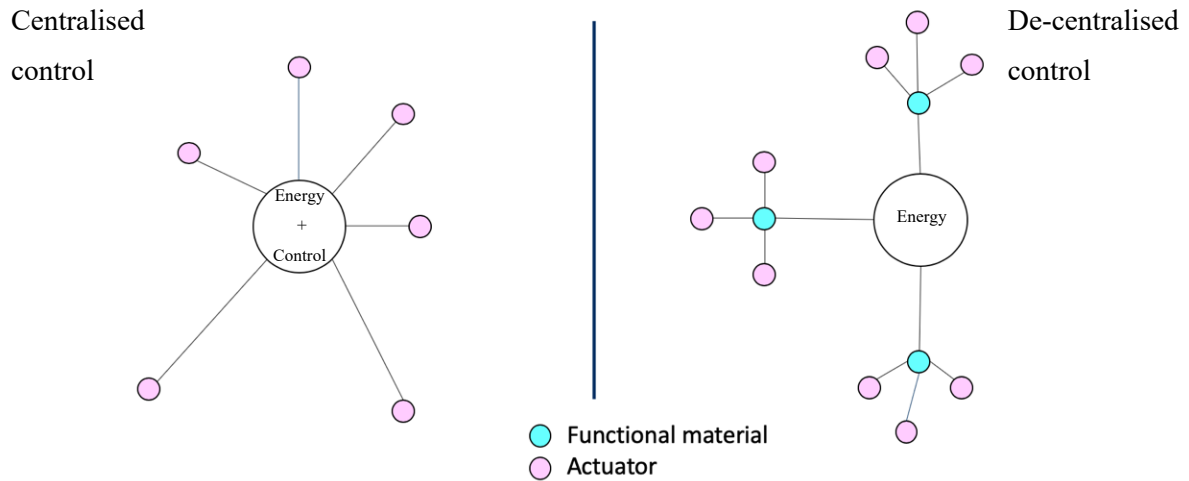


Figure 2.16: Proposed use of functional materials for the control of multiple actuators.

Figure 2.16 shows a summary of centralised and de-centralised control of multiple actuators. The design and optimisation of single actuators often form the focus of research. However, the field of soft robotic devices has an outlook towards creating larger scale systems that can utilise the benefits of increased compliance. It is therefore important to also focus on how multiple actuators can be controlled remotely in a way that is complimentary to the soft or compliant design.

If a functional device is placed in an environment, the response of the device to a stimulus can be measured in order to give a feedback or ‘awareness’ of the environment it is in. This has the potential to open up the design space of functional soft and compliant actuators to employ de-centralised responses such as environmentally responsive self-deploying mechanisms. The biological analogs of which could be unfurling of flowers or the dilation of the pupil of an eye. Alongside the self-sensing characteristics of a number of the electrostatic actuators considered in this review there is potential for novel environmentally responsive actuators. The use of functional materials adds the potential for research into soft and compliant actuators that share beneficial characteristics with biological systems.

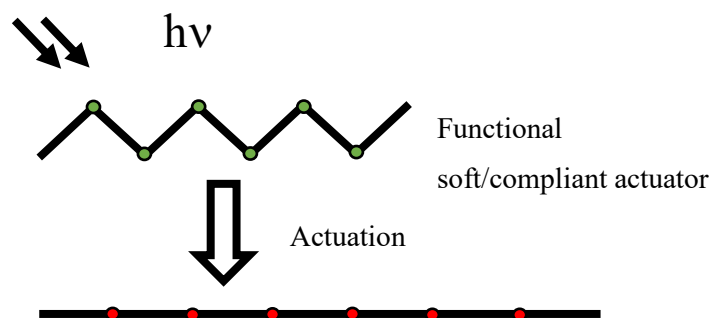


Figure 2.17: Proposed mode of actuation by environmental stimulus (light) for functional soft and compliant actuators.

Figure 2.17 shows a proposed mode of autonomous actuation using environmental stimulus using functional materials integrated into a compliant actuator. Functional materials have been used in a number of engineering applications for stand-alone solid-state devices. There is an opportunity to utilise the transducer properties of functional materials to allow for more integrated designs of actuators that are less reliant on traditional electronic components to support the soft or compliant actuator. Of the functional materials considered in this chapter, we suggest that photovoltaics are the most complimentary to electrostatic actuators because of the opportunity to utilise the transduction of photonic energy by the photovoltaic material to provide methods of de-centralised and autonomous control. In addition, there are a number of parameters of light that can be explored to develop control such as wavelength, intensity and frequency. There is a space in robotic research for the integration of functional materials with soft and compliant actuators which has yet to be explored. As this chapter highlights, there are opportunities to further the field to develop completely soft and integrated robotic devices.

### 2.11 Conclusions

In this chapter we have highlighted that there is a research gap in the use of functional materials as a means of providing control for actuator devices. By considering the state of the art of functional materials it was highlighted that there is significant opportunity for novel research in the use of photo responsive functional materials such as semiconductors to control electrostatic actuator devices such as the DEA. This provides opportunities to explore methods of de-centralised and autonomous control of electrostatic actuators which reduce the need for traditional control methods and allow for more compliant actuator designs.

From the conclusions made in this review, there is a research opportunity in exploring the use of photovoltaic materials with electrostatic actuators to provide opportunities for novel control. From the materials and actuators considered in this review, we suggest that a-Si and DEA are the material and actuator that can provide a starting point for this research. From the literature it was established that semiconducting materials, such as a-Si have the potential to operate at the high voltage requirements of a DEA. As well as showing sensitivity to photonic stimulus, allowing for potential application of control. The DEA has been selected due to the high achievable strains as well as the potential to achieve in-plane and out-of-plane actuation. One of the research gaps highlighted in this review is a characterisation of semiconducting materials such as a-Si with respect to their use at high voltage. Therefore, in the next chapter we look to characterise the electrical, photonic and mechanical properties of a-Si with respect to their use with DEAs.

## Chapter 3: Manufacturing, Experimental Methods and Characterisation

### 3.1 Introduction

As highlighted in the literature discussed in chapter 2 there are significant opportunities to explore the use of photovoltaic material such as the amorphous silicon (a-Si) [56] with electrostatic actuators. In this chapter an empirical characterisation of a-Si will be conducted to establish a basis for the structural, optical and electrical properties of a-Si and then we will propose the most suitable confirmation to use alongside electrostatic actuators. As evident from the literature discussed in chapter 2, a-Si can generate large changes in resistance in response to an optical input. However, with little research surrounding the use of a-Si at high voltages this chapter looks to establish the basis of the fundamental optical and electrical responses.

Functional materials can provide an opportunity to advance electrostatic actuator design to increase functionality and reduce reliance on solid state electronic components that are difficult to integrate into a soft design. Other materials such as photo voltaic ceramics found in light dependent resistors (LDRs) will be tested alongside a-Si as a baseline reference that is widely used in both industry and research.

#### 3.1.1 Chapter outline

The material selection process in this chapter will involve the following characterisation steps;

- A basic outline of the theory surrounding the material properties of a-Si.
- Outline of the fabrication process of a-Si samples.
- Characterisation of the structural properties of the a-Si samples including surface quality using scanning electron microscopy (SEM) and atomic force microscopy (AFM).
- Characterisation of the layer thickness of a-Si and the optical properties using ellipsometry.
- Low and high voltage testing of a-Si to ascertain the electrical properties at the two operational domains.
- Two-layer numerical model of the a-Si developed to support the findings of the real-world electrical testing and predict optimal layer thickness as well as the lowest achievable resistance.

To better understand the potential of a-Si, characterisation techniques can be used to establish the effectiveness of this material for use with electrostatic actuators. Microscopy techniques such as atomic force microscopy and scanning electron microscopy can shed light on the surface quality of the material deposited and establish potential causes of defects in the material. The photonic response and the precise thicknesses of the a-Si layer can be measured using ellipsometry. These results will then be supported by both modeling of the a-Si layer and electrical testing of the a-Si.

## 3.2 Amorphous Silicon

### 3.2.1 Background Theory

Amorphous Silicon (a-Si) is a form of polycrystalline silicon wafer with no long-range crystallographic orientation. This means that all the crystallographic grains in the Silicon are randomly orientated. This differs from other amorphous materials which have no crystallographic grains and are instead ‘frozen’ in a glassy state. This amorphous grain structure is largely due to interstitial hydrogen atoms, which lend the material a lot of its unique properties. Amorphous Silicon is often referred to as a-Si:H to denote this hydrogenation.

There are three main forms of silicon that are widely used, amorphous, poly-crystalline and single crystal: a-Si containing randomly orientated grains; polycrystalline containing directionally orientated grains; and single crystal being formed from a single grain of silicon. Each form respectively has improved electrical properties, but the manufacturing process is increasingly complex and expensive. Amorphous silicon was chosen for this project due to its simplified manufacturing process, however there is scope to use different forms of silicon in future work if significantly improved electrical properties are desired.

### 3.2.2 Electronic energy levels

As mentioned in the previous chapter, a-Si is a semi conducting material. This means that the band gap of electron energy levels between the valence band and conduction band is small enough to be equivalent to the energy of a photon. With the stimulation of photonic energy, the electrons in the a-Si can be promoted from the valence band to the conduction band and become mobile. The hydrogenation of a-Si allows for short electron diffusion lengths by providing interstitial electronic energy levels between the valence and conduction bands for Silicon. As mentioned by P.Y. Chiou et al. “the large number of electronic defect states in undoped a-Si:H results in a short ambipolar electron diffusion length of less than 115nm”[56].

### 3.2.3 Summary

The amorphous nature of a-Si not only lends itself to ease of manufacturing and lower component cost, but the amorphous grain structure gives the material a higher inherent resistance than other crystallographic conformations. This can provide a unique opportunity for larger relative changes in resistance as the semi conducting properties are exploited by moving the material from a high resistance passive state to a low resistance state by increasing the photonic stimulus. In this chapter both electrical testing and numerical modeling will be used to establish the magnitude of this resistance change.

### 3.3 Manufacture method of a-Si

#### 3.3.1 Sample preparation

For the characterisation process a standardised a-Si sample size was designed to ensure consistency and comparability between tests. Glass substrates were used due to their high melting points and the high operating temperature (250°C) of the plasma enhanced chemical vapor deposition (PECVD). There are two different glass substrates onto which a-Si was deposited. The first is a plain glass substrate and the other is a glass substrate coated in a conducting Indium Tin Oxide (ITO) layer, shown in figure 3.1 (a) as used in the work by P.Y. Chiou et al [56]. This can help to improve the conduction across the sample by reducing the electrical pathway between the two electrodes by conducting through the thickness of the a-Si layer rather than across the layers surface. Samples of both substrates were cut to the dimensions shown in figure 3.1 ready for deposition.

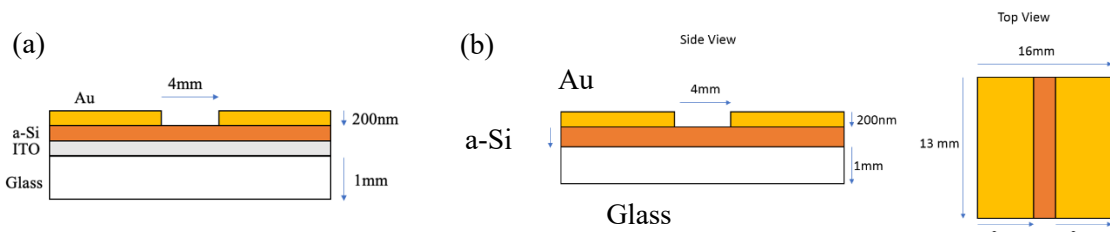


Figure 3.1: (a) Schematic of the a-Si and gold electrode layers deposited on ITO coated glass substrates (b) Schematic of the a-Si and gold electrode layers deposited on glass substrates.

Figure 3.1 shows the schematic for the standardised a-Si samples. The separation gap for the two-gold surface electrode was 4mm in line with literature which suggests a general guideline (IPC-2221A [70]) of 1.5-2kV per 5mm to avoid sparking between the two electrodes.

To deposit a-Si onto a substrate a process known as plasma enhanced chemical vapor deposition (PECVD) is used. This process is conducted in clean room conditions to reduce the risk of surface contamination and ensure a high-quality deposition layer. In this research a class 10000 cleanroom facility was used to manufacture all samples (21C +/- 1C; 50% +/- 5% humidity). In the PECVD process the substrate is first cleaned using isopropanol and acetone in an ultrasonic bath to remove any surface contaminants. The clean substrate is placed in a vacuum chamber, with elevated temperatures (250°C) and an applied voltage between the substrate plate and the deposition plate to cause the gaseous a-Si precursor to form a plasma. The opposing charge between the substrate and the inlet cause the particles in the plasma to be attracted to the substrate and deposited on the surface. A schematic of the Oxford Instruments Plasmapro System 100 PECVD used in this research is shown in figure 3.2.

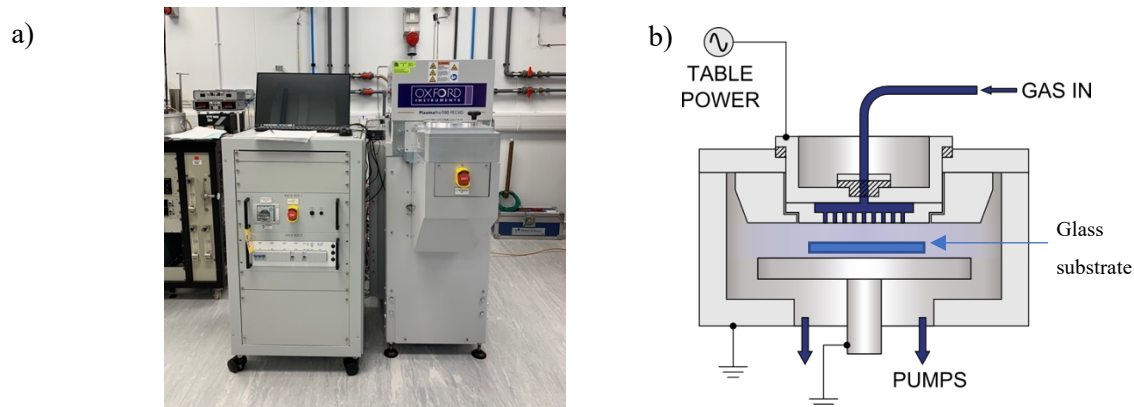


Figure 3.2: a) Oxford Instruments Plasmapro System 100 PECVD b) Schematic of the deposition chamber of the PECVD Reproduced from [71].

Depositing the a-Si in a lab environment allows the control of the layer thickness. The PECVD machine shown in figure 3.2 deposits material at a rate of  $\sim 28\text{nm}$  per minute. Three deposition times were selected: 15 minutes, 30 minutes and 50 minutes resulting in deposition thickness of  $420\text{nm}$ ,  $840\text{nm}$  and  $1400\text{nm}$  respectively. These deposition times were selected based on the deposition limits of the PECVD machine and the thicknesses were measured using an ellipsometer.

After deposition of the a-Si, the samples were then masked with a photo resist in an ultra-violet photolithographic process ready for the deposition of gold electrodes. A  $4\text{mm}$  mask between the electrodes was used to leave a large enough distance to reduce the chance of sparking between the electrodes at the expected test voltages. Gold electrodes were then sputtered onto the surface using a sputter coater (Moorfield Minilab125 Sputter coater). These electrodes consisted of a  $400\text{nm}$  titanium layer followed by a  $200\text{nm}$  gold surface layer. The photo resist was then removed in an etching process with acetone and isopropanol using an ultrasonic bath to assist the lift off.



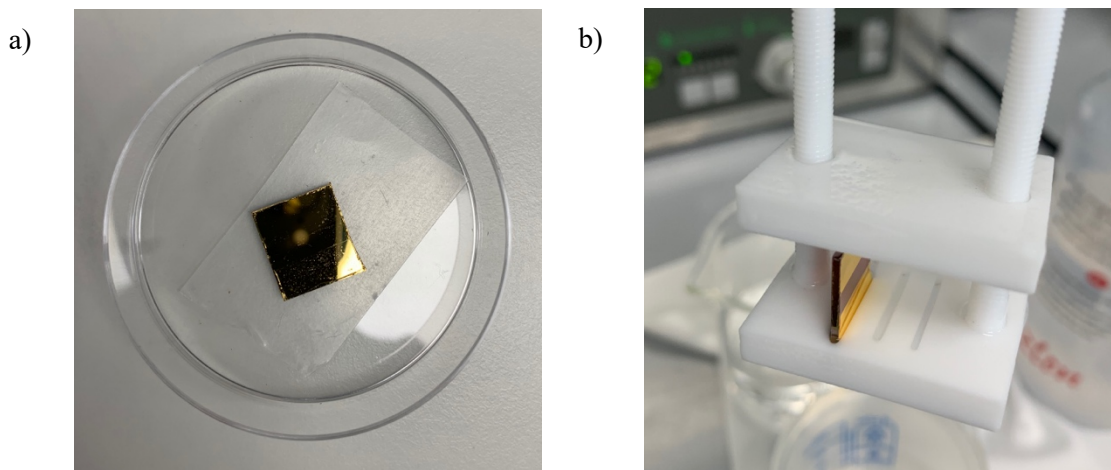


Figure 3.3: a) Image of a-Si sample after the sputter coating of gold electrodes b) Image of the final samples after etching to lift off the masked region.

The images in figure 3.3 show an a-Si sample at two stages of the manufacturing process. Image a) shows the a-Si after the deposition of the gold electrodes. The top surface of the sample is still entirely coated with gold from the sputtering. The central section of the sample which contains the photo resist is then etched away removing the gold using acetone and isopropanol. This process is shown in figure 3.3 b).

### 3.2.2 Summary

The manufacturing process defined above was repeated for a number of samples with differing a-Si layer thicknesses and substrate preparations. These can be summarised by two categories: a-Si samples with plain glass substrates and a-Si samples with ITO coated glass substrates. For each substrate, samples of three different deposition times were made: 15, 30, and 50 minutes. For each deposition time four samples were manufactured, totaling 12 samples with plain glass substrate and 12 samples with an ITO coated glass substrate.

## 3.4 Microscopy of a-Si

### 3.4.1 Atomic Force Microscopy (AFM)

Atomic force microscopy is a characterisation process in which an atomically sharp electrically charged point is brought over the surface of the sample being imaged. The atomic force interaction between the materials surface and the point of the microscope is measured and used to give nanometer resolution images of the topography of a materials surface. This data can be resolved into an image and can be used to show surface roughness and potential defects associated with the topography of the materials surface.

### 3.4.2 A-Si ITO substrate

Initially a-Si samples with a conductive ITO layer between the glass substrate as shown in figure 3.1 (a) and the a-Si deposited layer were imaged using the AFM. The topographical image of the area of the sample resolved from the AFM can be seen in figure 3.4:

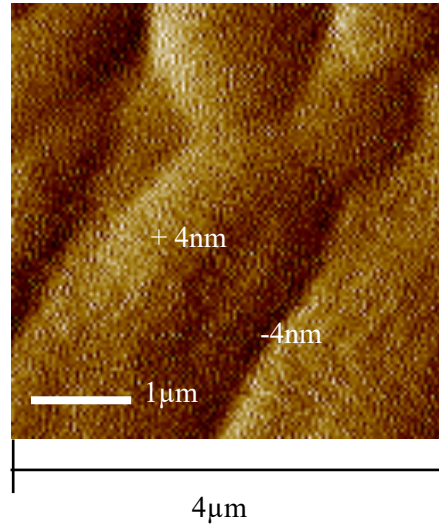


Figure 3.4: AFM image of a-Si layer of a-Si sample deposited on ITO coated glass substrate.

As can be seen from the image in figure 3.4 there is a very rough boulder like structure to the surface of the a-Si, the surface roughness was measured to be  $\pm 4\text{nm}$  from the midpoint of the layer thickness ( $0.84\mu\text{m}$ ). This roughness is unexpected from a-Si and is likely due to the underlying ITO layer which has a very rough surface topography. This could cause potential issues with poor adhesion of the a-Si due to the surface roughness making it difficult to deposit a uniform layer thickness of a-Si on the surface of the ITO, as well as sites for defect formation. All of which would be non-beneficial for high voltage applications and may cause electrical breakdown, but this shouldn't be as much of an issue at lower voltages.

### 3.4.3 A-Si Glass substrate

Secondly, a-Si deposited on a plain glass substrate was imaged using the AFM and the topographical image is shown in figure 3.5.

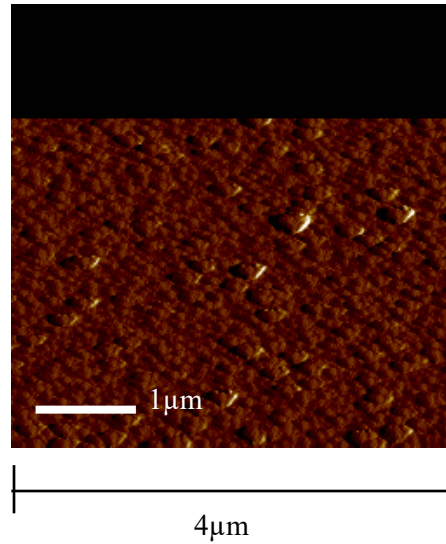


Figure 3.5: AFM image of the surface topography of a-Si layer deposited onto a glass substrate.

As can be seen from figure 3.5 the a-Si layer deposited on a glass substrate has a very regular surface topography. In comparison to the AFM image shown in figure 3.4 of the a-Si layer deposited on ITO the glass substrate sample does not show the same irregular surface roughness. There is still some surface roughness present due to the natural roughness present from clusters of a-Si atoms, but it is on a much smaller length scale than the roughness seen in figure 3.4. Leading to the hypothesis that the addition ITO, is causing the observed increase in roughness. Future work would be required to test this hypothesis, however from the images shown in figure 3.4 and figure 3.5 and high surface roughness of ITO being a known factor in literature [72] an argument can be made that the use of ITO has a potential impact of the uniformity of the deposited a-Si layer.

#### 3.4.4 Scanning electron microscopy (SEM)

Scanning electron microscopy (SEM) is a characterisation technique that uses a high-power electron beam that is scanned over the surface of the material with the scattered and reflected beams from the surface of the imaged sample are recorded and used to produce the image. This can give extremely detailed micrometer resolution images of a material surface. This gives less information on the surface topography in comparison to AFM. However, SEM shows more detail of larger features on the surface of the a-Si. In this research SEM techniques were used to image the surface of the a-Si samples deposited on ITO coated glass and plain glass substrates. Example images from the microscopy are shown in figure 3.6 (ITO) and figure 3.7 (glass).

### 3.4.5 a-Si ITO substrate

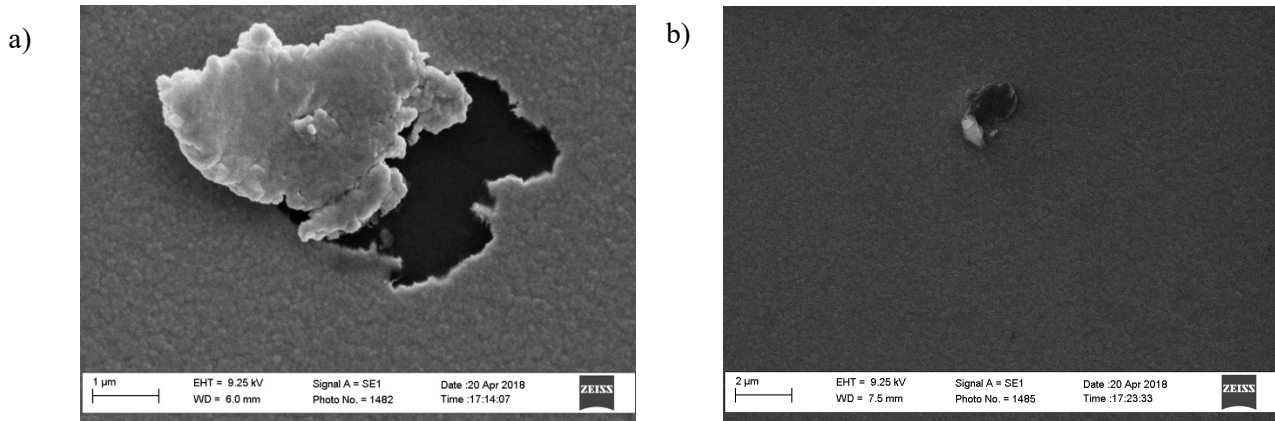


Figure 3.6: a) Detailed SEM image of defect in a-Si layer of ITO coated glass substrate. b) Example of Defect in Au electrode layer of a-Si sample deposited on ITO glass substrate.

As can be seen from figure 3.6 there are clear examples of micron sized defects in the a-Si layer. Although small a number (5 counted) of defects of this size were observed across the a-Si surface. Figure 3.6 a) clearly shows an area of a-Si that has completely separated from the substrate below. This complete separation of the a-Si from the ITO layer below would suggest that there are areas across the a-Si of poor layer adhesion which is supported by the example defects observed such as that shown in figure 3.6 b).

### 3.4.6 a-Si Glass substrate

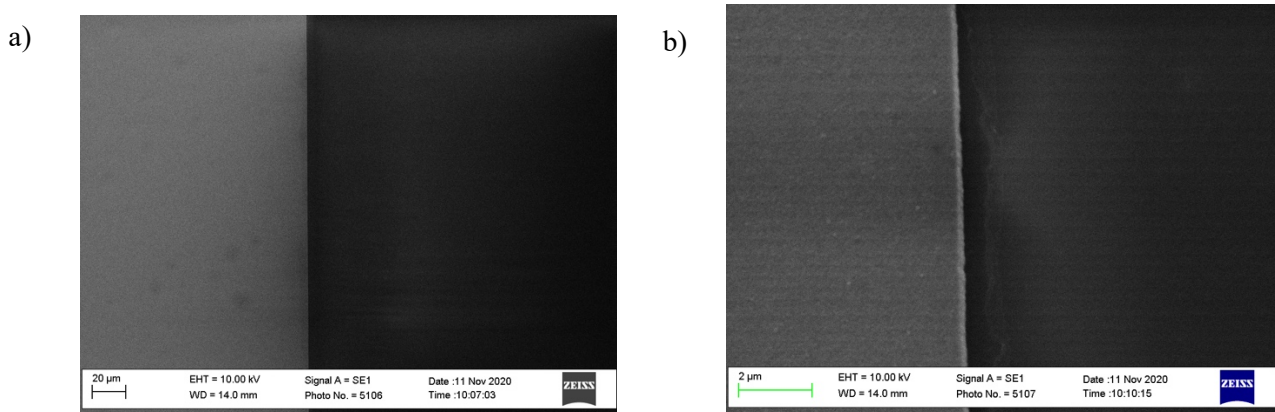


Figure 3.7: a) SEM image of the Au/a-Si interface. b) SEM image of the magnified Au/a-Si interface deposited on a glass substrate.

As can be seen from the SEM images in figure 3.7 the use of glass as a substrate provides a much higher quality surface with a little to no noticeable defects when compared to the SEM images of the ITO substrate shown in figure 3.6. Figure 3.7 a) shows the surface interface between the deposited gold electrode on the left and the a-Si on the right, these images show clearly that at a 20 micron scale there

is no evidence of potential surface defects and the samples are of a high enough manufacturing quality to advance to high voltage testing.

#### 3.4.7 Summary

The images from the AFM showed a distinct difference in surface quality between the ITO coated substrate and the plain glass substrate. With the ITO coated sample having a larger surface roughness than the plane glass. This suggests that the addition of the conducting ITO layer has a negative impact on the achievable surface quality.

The findings from the AFM images shown in figure 3.5 are supported by those shown in the SEM images in figure 3.6 where a number of areas of complete separation of the a-Si from the underlying ITO substrate are shown. The cause of this may be the roughness of the interstitial ITO layer made evident by AFM leading to poor adhesion of the a-Si to the substrate below. In low voltage applications it would likely not be an issue having defects this small (3 microns). However, the high voltage required for electrostatic actuators such as dielectric elastomer actuators (DEA) are more likely to cause issues with small scale defects such as this. As high voltage will create a larger differential in charge between the a-Si and the lower conductive ITO there is a risk of shorting through the thickness of the sample to the lower resistance ITO layer beneath. This is because at higher potential differences a small defect will provide a path of considerably lower resistance than the inherent resistance of the thickness of the a-Si.

#### 3.5 Ellipsometry

Ellipsometry is a characterisation technique which measures the reflected and refracted light from an incident beam of light and compares them against a known database of reference materials. This technique is extremely powerful and uses numerical modeling to fit the data to that of known material samples, giving precise film thicknesses as well as optical properties of the thin film. This technique is used to obtain a better understanding of the layer thickness deposited by the PECVD to ascertain if it is consistent with the manufacturer's specifications. The optical properties of the different thickness of a-Si samples were measured and compared to that of a bulk a-Si reference to gain a better understanding whether edge effects, due to the thinness of the deposited films, need to be considered. In this investigation a spectroscopic ellipsometer (J A Woolam RC2) was used.

To interpret the data from the ellipsometer, a numerical model is fitted to the data recorded. For the thickness measurements of the a-Si layer a Lorentz model was used [73]. This was fitted to the data collected from the 15, 30 and 50 minute deposition time samples. The layer thicknesses are shown in table 3.1:

Table 3.1: Comparison of measured a-Si layer thickness (not including substrate) using ellipsometry and the manufacturers claimed values.

Sample deposition time (mins)	Ellipsometer thickness (nm)	Manufacturer's prediction (nm)	% Difference
15	410	420	2.4%
30	816	840	2.9%
50	1350	1400	3.6%

As table 3.1 shows there is a slight over estimation by the PECVD manufacturer with regards to the deposited layer thicknesses. However, in the scope of this research and considering the scale of the actuators that are being designed, nanometer variations in thickness are unlikely to cause significant variation in optical and electrical properties between samples of the same deposition time. The Lorentz model was used for fitting the data to give the film thickness of the a-Si layer. And Newton-Raphson model method was used to obtain optical function of the thin film

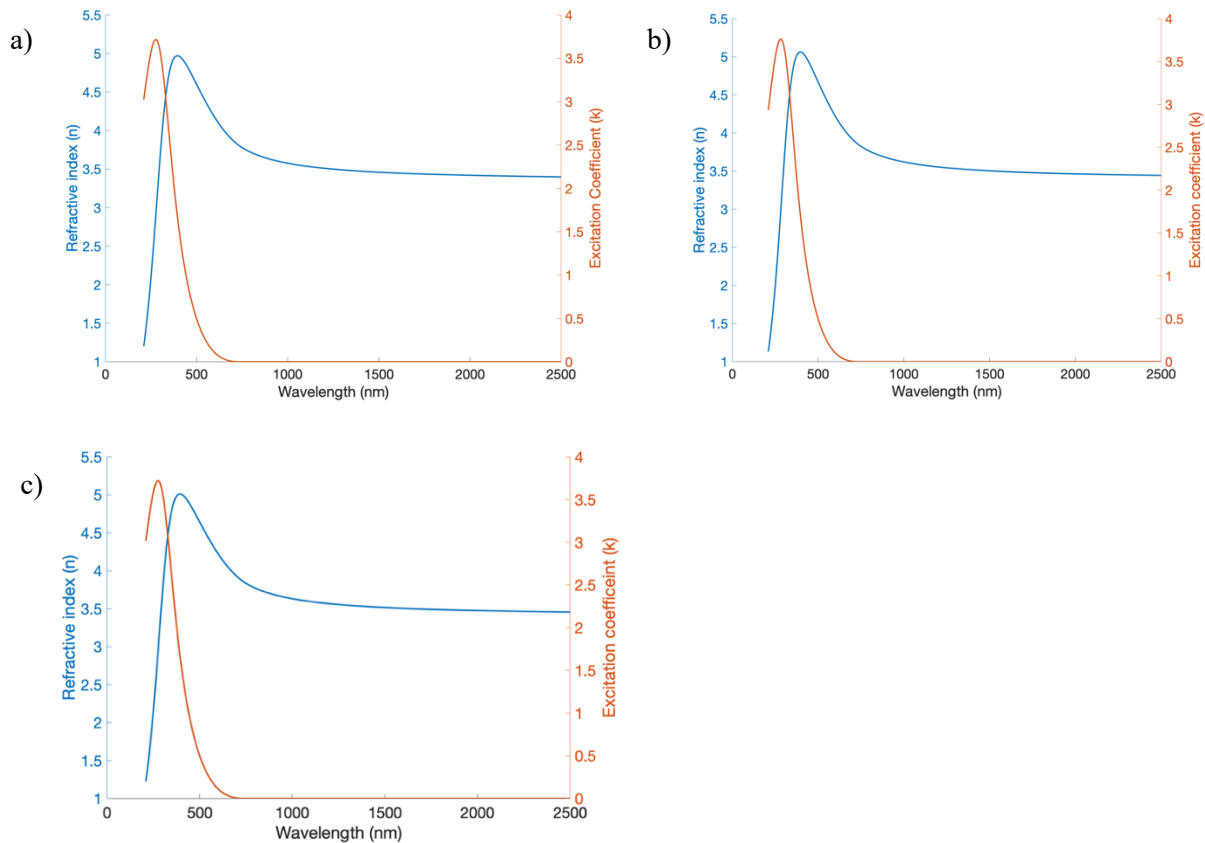


Figure 3.8: Optical functions from ellipsometry data using a Newton-Raphson model. A) 410nm B) 816nm C) 1350nm

### 3.5.1 Discussion

The optical function plots shown in figure 3.8 are plots of two optical parameters, the refractive index,  $n$ , and the excitation coefficient,  $k$ , as a function of wavelength of incident light. Both these parameters give valuable information about the optical response of the a-Si. By increasing the layer thickness of the a-Si there is little change in the peak excitation coefficient for the layer (3.71 for 410nm thickness, 3.75 for 816nm thickness and 3.39 for 1350nm thickness), peaking at 269nm, 276nm and 310nm wavelength respectfully. This corresponds to ultraviolet light, which encompasses the 300-400nm range of wavelengths. This means that the greatest excitation of the a-Si layer occurs in the ultraviolet part of the visible spectrum. However, it is also important to consider that there are associated risks to using ultraviolet sources such as damage to operators' skin and eyes as well as risk of material degradation due to prolonged exposure. A safer source of light would fall into the visible spectrum which extends from around 400nm to 700nm but would still achieve high excitation values. From looking at the plots in figure 3.8 it would be expected that the use of visible light will still lead to excitation of the a-Si samples. However, the extent of the excitation will 1.45 at 400nm compared to a peak value of 3.39 at 312nm for a 1350nm thick layer of a-Si, therefore the expected voltage swing will be lower.

When compared to a reference sample of bulk a-Si it can be seen from figure 3.8 that as the layer thickness increases to 1350nm the samples optical response becomes more representative of bulk material model used in the ellipsometry calculation for a-Si. Therefore, it can be considered that a layer thickness of around 1350nm will be less likely to be affected by edge effects during testing. This is a tentative prediction however as high voltage behavior of these materials is an area with little literature and predictions of the high voltage response of a-Si is relatively undocumented, except in the case of 'burning in' electronic components, where the component is subjected to a high voltage to improve the performance of the device, much akin to the annealing process in metals.

### 3.5.2 Summary

With both characterisation of the a-Si samples established from microscopy as well as the optical properties of the a-Si layer measure by ellipsometry there is enough understanding of the material properties of a-Si to begin electrical testing. The data from the ellipsometry suggests that to achieve the greatest excitation coefficient, a thicker layer of a-Si is preferable. However, when comparing to bulk a-Si reference used in the software of the spectroscopic ellipsometer (J A Woolam RC2), thickness past the 1350nm deposited are unlikely to improve this coefficient further. Therefore, electrical testing will be conducted using the 50 minute (1350nm) deposition time to ensure the best optical properties. However, there is scope to investigate thinner films in order to improve the flexibility of the a-Si for better integration with soft robotic devices.

### 3.6 Characterising the electrical response of a-Si at low voltage

Low voltage ( $<10\text{V}$ ) testing of a-Si is important to develop an understanding of the electrical response of the material at voltage ranges of commonly used electronic devices. Further to this, research around electrostatic actuators, such as the DEA, looks to reduce the high operational voltages [23]. Therefore, it is important to develop a robust characterisation of a-Si at all voltage ranges to understand its potential alongside all actuator technologies. For this test the ITO sample was tested as the plain glass sample showed large amounts of noise on signals at low voltage (even when tested in a Faraday cage to remove the ambient 50Hz noise from surrounding electrical components).

#### 3.6.1 Experimental set up

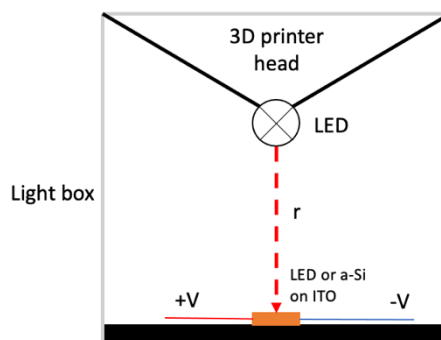


Figure 3.9: Schematic of the motorised stage with an LED Light source used to test the low voltage response of a-Si. Where  $r$  is the distance between the LED and the test sample.

In this test an enclosed motorised stage (modified 3D printer shown in figure 3.9) with an LED light source (365nm LZ1-10UV00) mounted to it was used to slowly move the LED towards the sample from an initial light intensity of 10kLux to the lowest intensity of 55Lux at 250mm from the sample. The light intensity was measured using a handheld light meter (Urceri MT-912). The samples were supplied with a current of 0.01A and the voltage was measured across the sample using a data acquisition device (DAQ) (National Instruments BNC-2111).



### 3.6.2 Results

To compare the effectiveness of a-Si as a light dependent switch for low voltage applications a commercially available LDR (Shenzhen Haiwang MJ20528) was used as a reference.

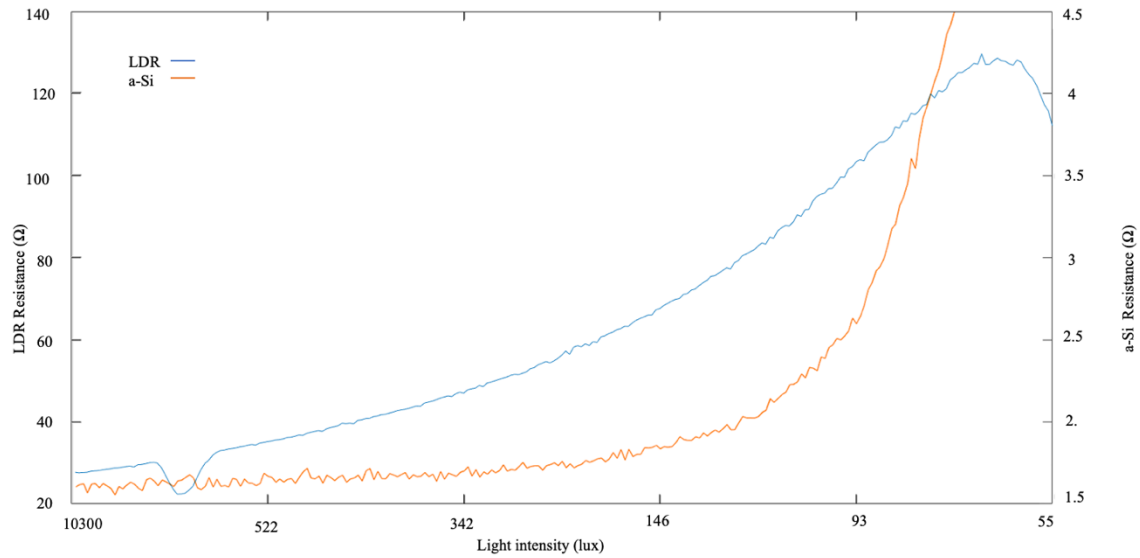


Figure 3.10: Resistance of the LDR and a-Si/ITO samples as a function of light intensity of the LED.

Figure 3.10 shows the voltage response of the LDR tested. As can be seen from figure 3.10 the starting voltage at 55Lux is around  $28\Omega$  with a maximum voltage achieved at 10kLux of  $127\Omega$ . The a-Si on ITO substrate sample was tested using the same motorised LED stage and experimental set up as the LDR. Figure 3.10 also shows results from the a-Si sample on ITO coated glass substrates as it was found that the plain glass substrates had a considerably greater resistance above the maximum resistance of a  $40M\Omega$  multimeter. Which lead to high levels of noise which dominated the measurements even when tested in a faraday cage (Department of Electrical Engineering at University of Bristol), highlighting that the inclusion of an interstitial ITO layer can serve to reduce the overall resistance of the system by providing a path of lower resistance for the current to flow through the sample as shown in figure 3.11.

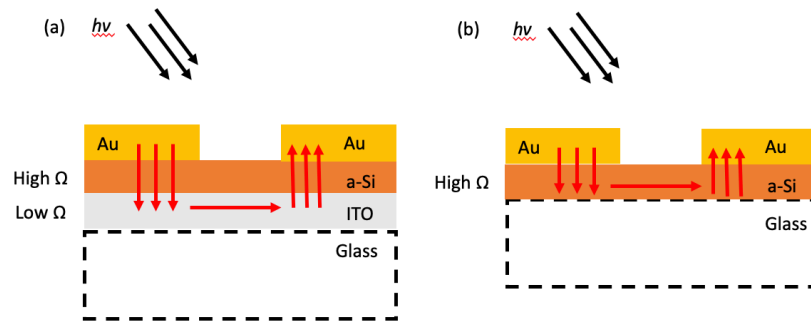


Figure 3.11: (a) Schematic of the current pathway through a-Si on an ITO substrate. (b) Schematic of the current pathway through a-Si on a plain glass substrate.

From looking at figure 3.10 the response of the a-Si has a more exponential response to light intensity than the linear response shown by the LDR. At 55Lux the resistance measured was  $1.6\ \Omega$ , which is an order of magnitude lower than that of the LDR. The resistance increases slowly until it exponentially increases to a maximum resistance of  $4.5\ \Omega$  at 10kLux.

### 3.6.3 Discussion

In comparison to the LDR the maximum resistance of the a-Si sample was two orders of magnitude less than the maximum resistance of the LDR. This could be due to the constant current being applied to the samples during testing, as the a-Si/ITO sample will have a considerably shorter current path of resistance ( $84\mu\text{m}$  through the thickness of the a-Si layer) compared to the millimeter length scale of the current path for the LDR. What is of interest from figure 3.10 is the comparison of the shape of response between a-Si and the LDR. What we can see from figure 3.10 is an approximately linear response from the LDR and a near exponential response in resistance from the a-Si. Therefore, for low voltage actuator applications a-Si may not be as effective as the LDR as a light-responsive resistor. However, this exponential resistance response of a-Si would suggest that a-Si can be more beneficial as an optical switch rather than an optical variable resistor.

### 3.7 Characterising the electrical response of a-Si at high voltage.

There are a number of potential electrostatic actuators that require high operational voltages such as the DEA and the DLZ. Therefore it is important to test the electrical response of the a-Si samples under these conditions. This is an area of research that has not been explored greatly and will provide key information for the development of novel research opportunities to provide means of de-centralised optical control to electrostatic actuators.

### 3.7.1 Experimental set up

The standard samples sizes of a-Si shown in figure 3.1 were connected to the high voltage amplifier (Ultravolt 5HV-A23-BP1) and the samples were tested at increasing voltage steps from 1kV to 5kV under three different lighting conditions. An ambient lab condition (62Lux), a low-level illumination (4.4kLux) and a high intensity (41kLux). The light intensity of each condition tested was measured using a handheld light meter (Urceri MT-912).

### 3.7.2 High voltage testing of a-si on ITO coated glass substrate

The results from the SEM (section 3.4.4) and AFM microscopy (section 3.4.1) of a-Si on an ITO coated substrate raised concerns about its ability to operate at high voltages. Therefore, a preliminary test was conducted where a sample of a-Si on ITO coated substrate was connected to a high voltage amplifier (Ultravolt 5HV-A23-BP1). Under ambient lab lighting conditions (62Lux), the sample was tested at increasing voltages. However, the ITO samples showed electrical breakdown as early as an applied voltage of 500V.

This is due to the low resistance of ITO providing an alternative electrical pathway through the thickness of the a-Si rather than along the layer shown in figure 3.11, reducing the distance across which sufficient potential can build up leading to breakdown. Therefore, it was concluded that ITO substrates were not suitable for the high voltage research applications.

### 3.7.3 High voltage testing of LDR reference

Common electrostatic actuators such as dielectric elastomer actuators currently require high voltages (>1kV) and low currents to operate. The relatively high current of the tested LDR was found not to be suitable for use with the DEA actuators intended to be explored in this research. Results of these preliminary tests can be found in the appendix A. Following this, a-Si on a plain glass substrate was chosen to be the basis for the functional device to be developed.

### 3.7.4 Ramp testing of a-Si on glass substrate

The SEM and AFM results would suggest that the higher quality of the deposition of a-Si on the untreated glass substrate would be more effective than the ITO coated samples at higher voltage. In order to be used alongside high voltage electrostatic actuators the a-Si must be stable at a voltage range of kV without electrical breakdown. To test this, the a-Si sample was connected to a high voltage amplifier and a voltage ramp was applied from 0.2 to 2.2kV.

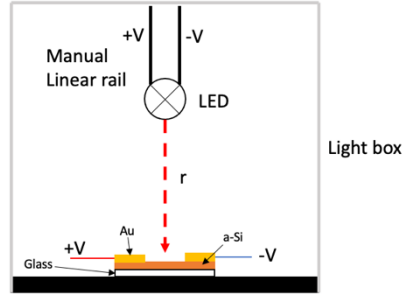


Figure 3.12: Schematic of the experimental set up for electrical ramp testing of a-Si on a glass substrate. where  $r$  is the distance from the LED to the a-Si sample.

A mechanical stage with a manually operated linear rail was used to mount an LED above the sample as shown in figure 3.12, and it was adjusted to increase the light intensity. The light intensity was measured using a handheld light meter (Urceri MT-912). The dark state (0 Lux) was taken by placing the sample in an enclosed space, in terms of applications an ambient lab condition (approximately 62 Lux) may be more representative of a baseline lighting condition for most applications.

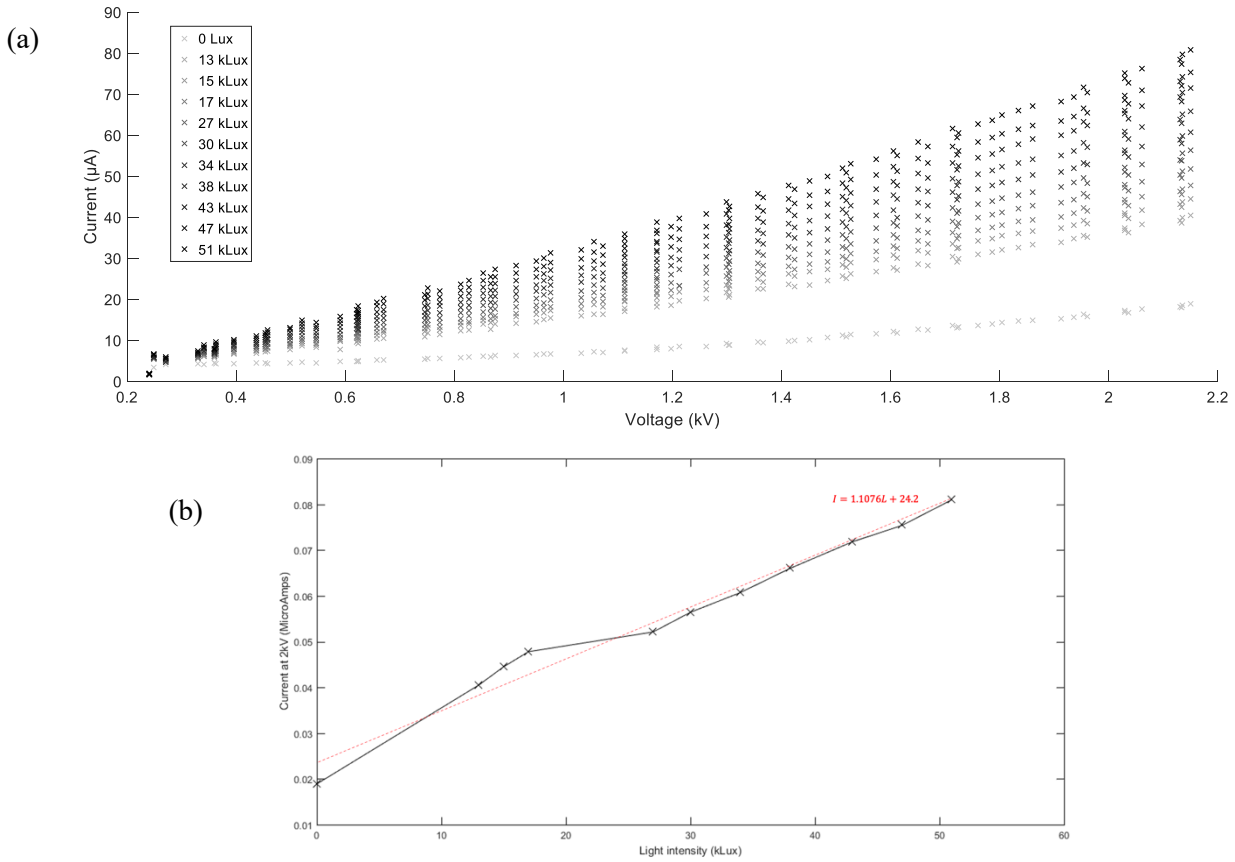


Figure 3.13: (a) Current measured across the a-Si as a function of voltage for differing light intensities. (b) Linear regression fitted to measured current at 2kV for differing light intensities.

Figure 3.13 shows that at all light intensities the current across the a-Si increases linearly with the increased voltage. In addition, the a-Si on a glass substrate was shown to be completely stable at all voltages tested. By taking the maximum currents recorded at 2.18kV for each light intensity a relationship between current and the light intensity applied can be assumed to be linear and a linear regression can be fitted to this data with a norm of residuals of 8.68, shown in figure 3.13 (b). The equation of this linear fit is as follows:

$$I = 1.1076L + 24.2 \quad (1)$$

Where  $I$  is the current and  $L$  is the light intensity

Therefore, as 
$$R = \frac{V}{I} \quad (2)$$

From this we can calculate the resistance of the a-Si in terms of Light intensity (Lux).

$$R = \frac{2.18}{1.1076L + 24.2} \quad (3)$$

### 3.7.5 Time dependent pulse testing

With the context of use alongside electrostatic actuators it is important that a-Si is not only stable at high voltage but also able to withstand a basic square wave input voltage that is typical for actuation. To test this a sample of a-Si on a glass substrate was connected to the high voltage amplifier with the same mechanical stage used to mount the LED above the sample as used previously. A simple square wave of voltage was applied to the sample with an off period of 10 seconds and an on period of 30 seconds as shown in figure 3.14. The current at increasing voltages was measured using a DAQ (National Instruments BNC-2111).

### 3.7.6 High voltage pulse testing at ambient lab conditions (62Lux)

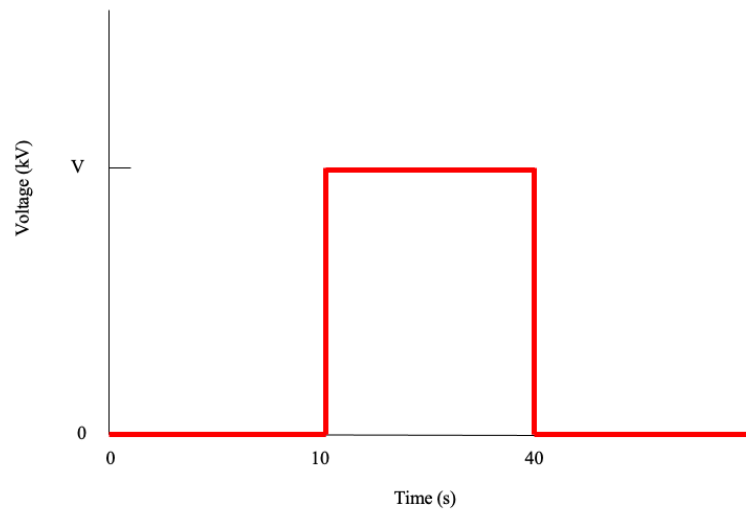


Figure 3.14: Example plot of the square wave voltage input applied to the a-Si where  $V$  is the applied voltage.

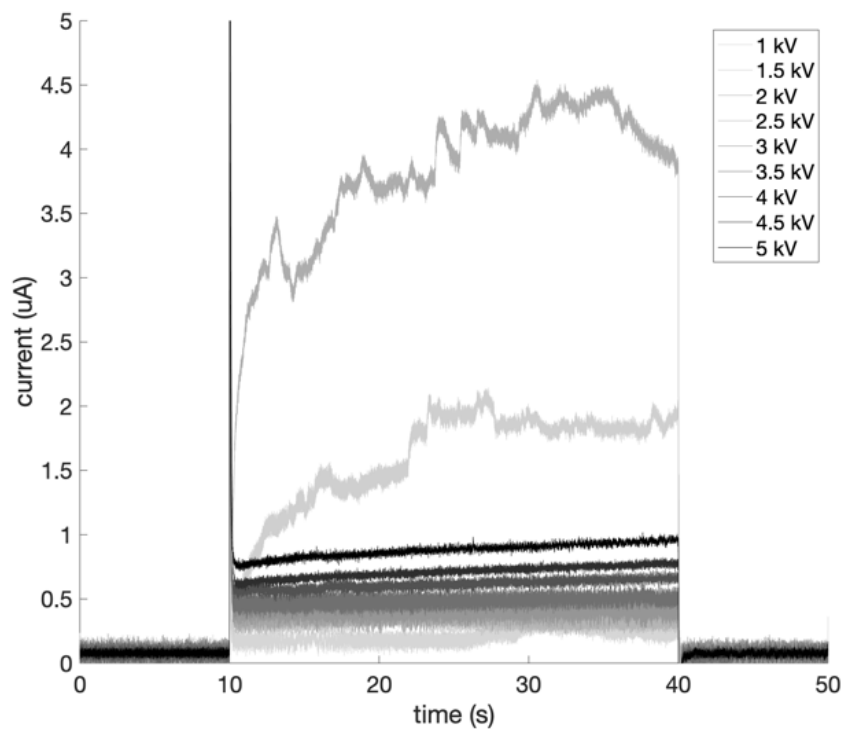


Figure 3.15: Plot showing the current response of a-Si on glass substrate from 1-5kV as a function of time at 62 Lux

As can be seen from figure 3.15, the current across the a-Si increased with each 500V intervals up to a maximum of just under 1 $\mu$ A. To be noted are the tests at 1.5 and 2kV which show significantly higher

and less stable current responses than recorded at any other voltage. This can also be seen in the 1kV curve after 25 seconds where there is a small rise in current until 40 seconds. It was noted during testing that crackling noises and small sparks were observed during these two tests. This is likely to be small dust particles on the surface of the sample allowing a path of lower resistance until they are destroyed by the high voltage. Despite the best efforts to control the environment of the high voltage test rig it is impossible to reduce the chance of small contaminants on the sample's surfaces. This is an issue that is often faced by electrostatic actuators that use high voltage to operate. However, as is evident in figure 3.15, despite this surface sparking the samples continued to operate as expected at increased voltages.

At low light intensities such as the 62Lux ambient lab room condition shown in figure 3.13 it is expected that a-Si would have a considerably higher resistance.

Table 3.2: Calculation of resistance change of a-Si at a light intensity of 62Lux using Ohm's law.

Voltage (kV)	Current ( $\mu\text{A}$ )	Resistance ( $\text{G}\Omega$ )
1	0.1	10
3	0.5	6
5	0.9	5.6

Using the DAQ outputs an estimation of the resistance changes of a-Si of the order of  $10\text{G}\Omega$  to  $5\text{G}\Omega$  as the voltage is increased from 1-5kV can be made. All presented data has been processed to reduce the signal noise where appropriate.

### 3.7.7 High voltage pulse testing at 13kLux

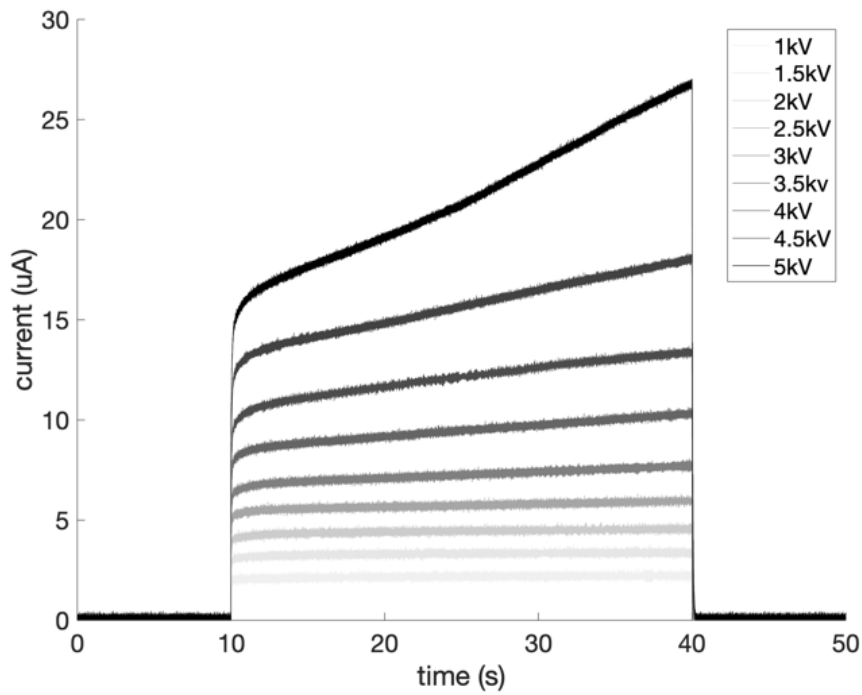


Figure 3.16: Plot showing the current response of a-Si on glass substrate from 1-5kV as a function of time at 13kLux.

Figure 3.16 shows the results of the pulse test at a higher light intensity of 13kLux, similar to that of a bright studio's lighting. As can be seen in figure 3.16 the current increases with voltage steps from  $2\mu\text{A}$  at 1kV to a maximum of  $27\mu\text{A}$  at 5kV. This would correspond to an effective resistance change from  $0.5\text{G}\Omega$  to  $0.19\text{G}\Omega$ . This is not as large a change as that observed in table 3.2 however what is noticeably different about this lighting scenario is the time dependent current profile noted at 3kV-5kV. At these higher voltages we see a departure from the continuous current response with respect to time and instead the current across the a-Si begins to increase linearly with time.



### 3.7.8 High voltage pulse testing at 41kLux

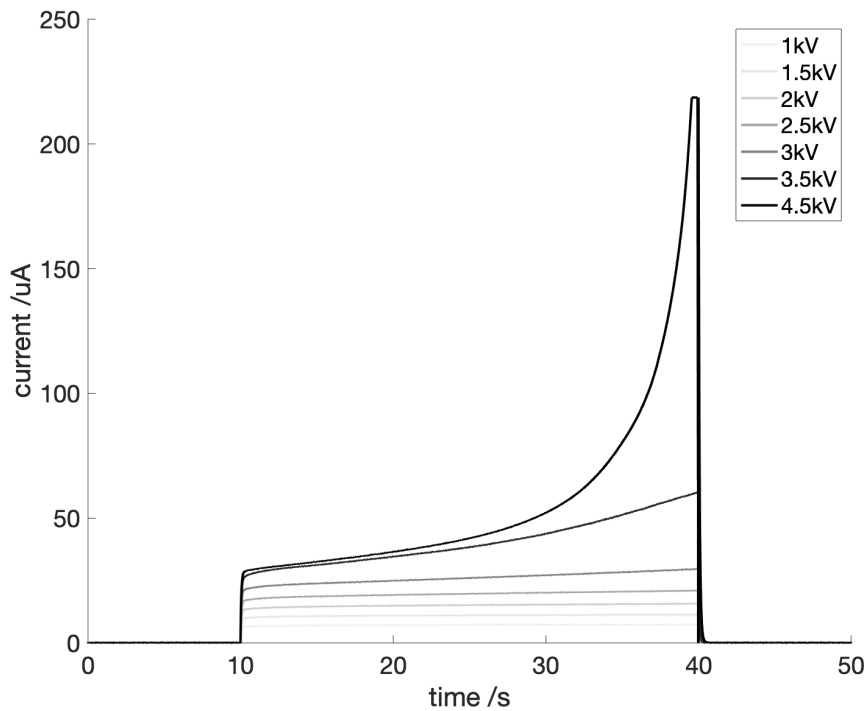


Figure 3.17: Plot showing the current response of a-Si on glass substrate from 1-5kV as a function of time at 41kLux

Figure 3.17 shows the high voltage testing of a-Si at the highest light intensity tested (41kLux) from 1kV to 4.5kV. The 5kV test has been omitted from this figure as the sample shorted across the electrodes at this voltage. The sample was then tested again at lower voltage and was found to operate as previously after the electrical breakdown. Noticeably in figure 3.17 the current values at this light intensity are significantly higher than recorded at the lower light intensities tested. At lower voltages (1kV-3kV) we see a flat response from the measured current over the time period of the pulse. As the voltage is increased, the current shows deviation from this linear response to a non-linear response. This is most apparent in the 5kV test where a strong exponential increase in current is seen over the 40 second test reaching the maximum current limit of the high voltage amplifier (225μA).

### 3.7.9 Discussion

The relatively slow time constant of this increase in current such as the one observed in the 5kV plot in figure 3.14 suggests that this is potentially either a capacitive effect or polarisation of the a-Si. Although future investigations would be needed to fully characterise this response it can be hypothesised that it is unlikely to be a capacitive charging of the a-Si as a discharge spike would be expected in figure 3.17 once the voltage was removed at 40 seconds. A potential explanation could be polarisation of the a-Si.

In this section we present a hypothesis for the observed resistance change seen in a-Si at high voltage. This is supported by research showing a-Si to exhibit large drain voltages in transistor applications at high voltages [74], the drain voltage is a measure of the voltage across the gate of a transistor. However, in electronics research the reference to ‘high voltage’ usually refers to voltages in the order of hundreds of volts ( $\sim 400\text{V}$ ) [75], there is little research surrounding the behavior of a-Si at voltages of the order of kV as seen in figure 3.17. Therefore, we propose a hypothesis for the behavior shown in figure 3.17 with further investigation into the physics of a-Si at high voltage being an area of future research.

The material structure of a-Si is polycrystalline, with a large number of randomly organised grains with no long-range organisation that you would expect from a polycrystalline material. These randomly orientated grains will have an associated dipole that could become polarised from the high voltage and over time as more grains become polarised and more current can flow through the a-Si.

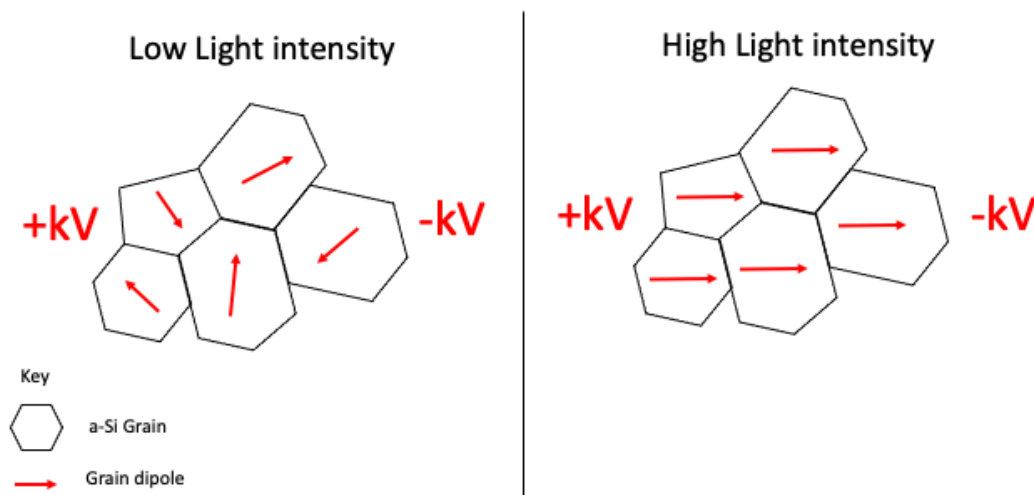


Figure 3.18: Schematic of the hypothesised polarisation of a-Si grain dipoles showing the hypothesised transition from low to high light intensity.

As seen in figure 3.18 one potential explanation for this increase in current over time at higher light intensities is increased alignment of the electrical dipoles of the crystallographic grains of the a-Si triggered by this increase in optical intensity. Initially, due to the amorphous structure of the silicon the grains would have randomly orientated dipoles which would increase the electrical current path and in turn the resistance of the material. At higher light intensities these grains will have a higher energy associated with them and there is potential for these dipoles to move more freely and orientate with the global potential difference applied to the material leading to a reduction in resistance.

From the increasing exponential response seen in figure 3.17 the question arises that if the sample was exposed to a lower light intensity for a longer time period would the same exponential increase in current occur. Assuming that the hypothesis of increased light intensity allowing for more rapid polarisation of the a-Si is valid, it would suggest that eventually polarisation would also occur at lower light intensities. This could highlight an area of potential future work. Within the context of electrostatic actuators, high time periods for large resistance changes leading to slow actuation of a device are less desirable than the response seen in figure 3.17.

The non-linear current response at high voltage would suggest that as the voltage is increased to 4.5kV the resistance of the sample tested is decreasing. We observe an exponential reduction in resistance, something that has previously been noted in the work by P.Y. Chiou et al. [56]. This shows the potential of a-Si to change from a high resistance state to a considerably lower resistance state. This is extremely desirable for use with DEAs as it may cause a large voltage swing across the actuator, leading to large changes in displacement.

Table 3.3: Lowest measured resistance at 5kV different light intensities.

Light intensity (Lux)	Lowest measured Resistance at 5kV ( $\Omega$ )
62	$5 \times 10^9$
$1.3 \times 10^4$	$1.9 \times 10^8$
$4.1 \times 10^4$	$2 \times 10^7$

Table 3.3 collects the lowest measured resistance for a-Si at each light intensity measured. This shows that between an ambient room environment (62Lux) and high light intensity (41kLux) a resistance change of two orders of magnitude can be expected. This is very promising for DEAs and should provide enough of a change to achieve a noticeable actuation.

#### 3.7.10 Quantifying the transition from linear to non-linear response

To better understand the relationship between light and resistance, linear and exponential fits were applied to the data in figure 3.17 to establish this transition from linear to a nonlinear resistance response. A two-term function was fitted to the current data from each voltage step measured at 41kLux. The fitting function included a linear component and an exponential component as show in equation 4. Where  $y$  is fitted to the current and  $x$  is fitted to time for the data presented in figure 3.17:

$$y = ax + be^x \quad (4)$$

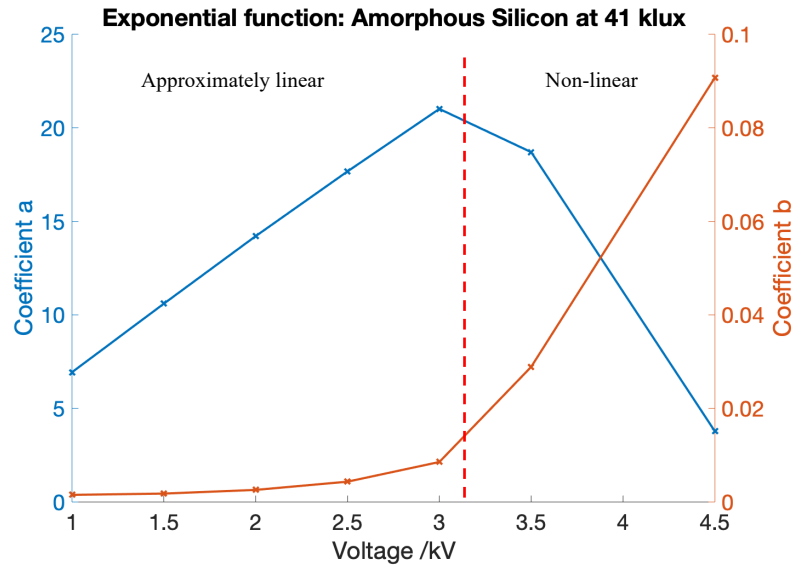


Figure 3.19: Plot of the exponential coefficients of equation (4) fitted to each voltage test for 1-4.5kV at 41kLux light intensity.

The coefficient  $b$  (exponential coefficient) will dominate, i.e. be large with respect to the non-linear coefficient  $a$ , when the data has an exponential relationship. Figure 3.19 shows that coefficient  $a$ , the linear coefficient, dominates the function from 1-3kV, after which a decline to 4.5kV is observed at which point the exponential coefficient increases and begins to dominate. This shows that there is a threshold around 3-3.5kV where the a-Si transitions from a linear current response to a non-linear current response with respect to time. By controlling both the voltage and the light intensity applied to the a-Si sample we are able to switch between a linear and nonlinear response. This is potentially beneficial in the context of DEAs, where the multiple order of magnitude changes in resistance shown in figure 3.17 can act as a switching mechanism for the actuator.

### 3.7.11 Thermal response

One consideration is that the reduction in resistance of a-Si seen in figure 3.12 could be a consequence of other forms of energy transfer other than photonic. The main form of energy that could also be transferred during testing is thermal energy from the LED light source being at close proximity to the sample. To test this the same ramp test was performed at the highest light intensity (51kLux approximately touching the a-Si sample). The a-Si sample was left under the LED source for three different lengths of time (0, 5 and 10 minutes) until the ramp test was started.

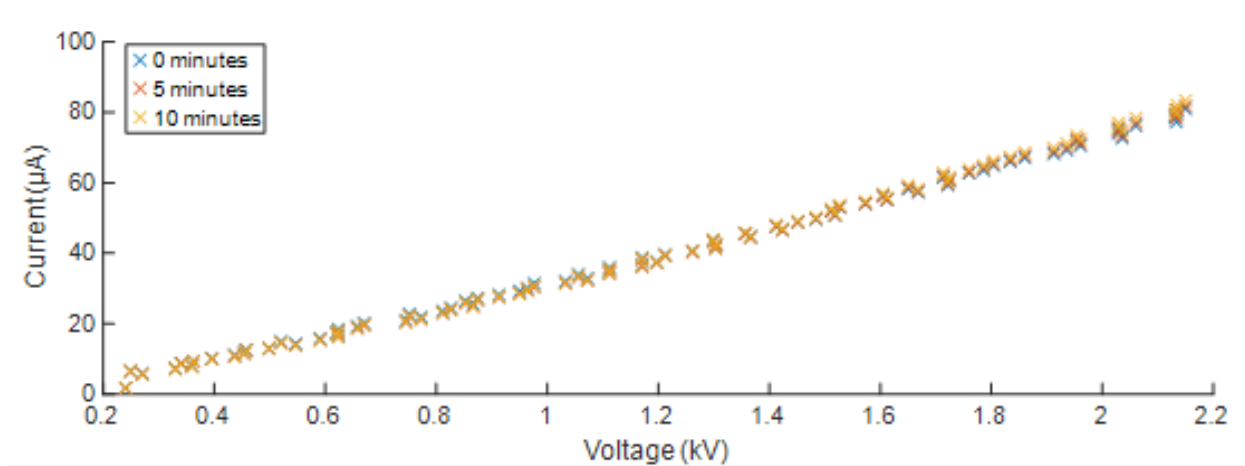


Figure 3.20: Shows a plot of the current/voltage ramp test for different length of time exposure to the LED source.

As is clear from the results in figure 3.20, there is no discernable difference in the ramp tests with increased LED exposure time. Therefore, it is unlikely that thermal energy transfer from the light source has a significant impact on the resistance.

### 3.8 SEM images post breakdown

During the high voltage testing there were several observed incidences of sparking on the surface of the a-Si (as mentioned in section 3.7.6) as well as electrical breakdown due to high voltage (41kLux at 5kV). A primary concern when considering a-Si as a material for designing future actuators is the resilience of the material to continuous high voltage exposure. After the high voltage characterisation a sample of the a-Si tested was imaged using a scanning electron microscope (SEM) to better understand the effect of high voltage on the a-Si surface.

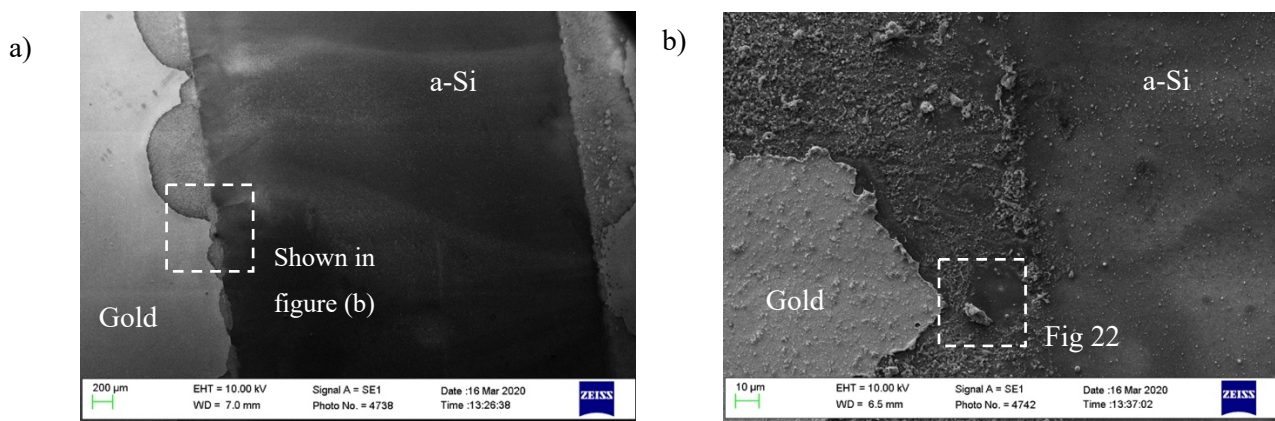


Figure 3.21: (a) SEM image showing the entire surface of the sample with the gold electrode on the left and a-Si centre. (b) Shows an SEM image of the surface damage to the gold electrode in (a) (undamaged SEM examples can be seen in figure 3.7).

As can be seen from figure 3.21, there is evidence of damage to the electrode surface due to electrostatic discharge at high voltage. Figure 3.21 (a) shows two major sites of spark initiation at the gold electrode, evidenced by the half-moon shaped craters at the top left of the image. There are also three light ‘mist’ like depositions across the surface of the central a-Si section. Under closer inspection in figure 3.21 (b) this is shown to be small particles of the gold electrode that have been vaporised from the gold electrode with the propagation of the spark across the surface of the a-Si to the counter electrode on the other side. Figure 3.21 (b) shows a close up of the interface between the damaged gold electrode and the a-Si. It is noticeable that, other than the small depositions of gold particles across the a-Si surface, these SEM images show no evidence of damage to the main section of a-Si after the electrical breakdown. Therefore, it can be suggested that the electrical breakdown was isolated to the air gap or outer surface of a-Si between the gold electrodes and the a-Si layer deposited was able to withstand up to 5kV without signs of the material breaking down. Potential methods of reducing the risk of breakdown of the electrodes would be to increase the distance between the two electrodes from 4mm if higher voltages above 5kV are required.

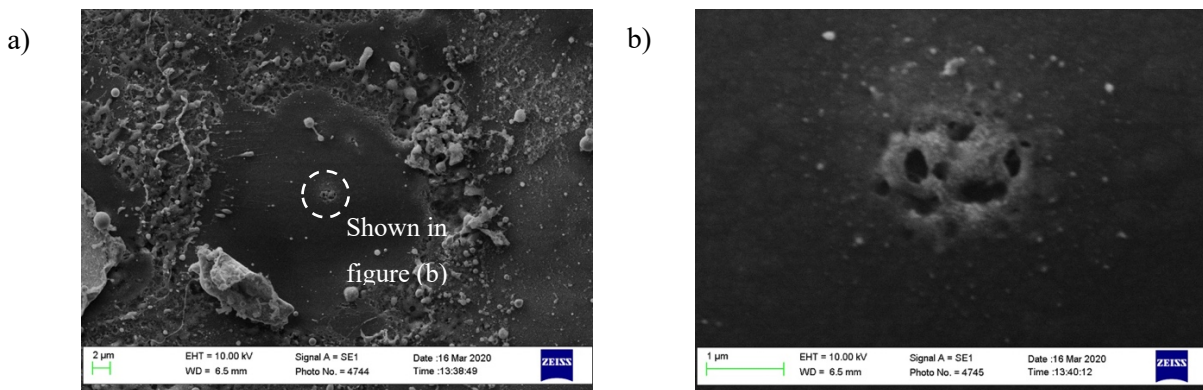


Figure 3.22: (a) SEM image showing the initiation site of electrical discharge from the gold electrode. (b) SEM image of the initiation site showing damage to a-Si under the electrode.

Closer inspection of the damage to the gold electrodes shown in figure 3.22 reveals that the damage to the electrode is localised. As can be seen in figure 3.22 (a) the area of gold electrode that has been completely vaporised by the electrical breakdown is around 12-15 $\mu$ m in diameter and the a-Si layer is clearly showing underneath the electrode. In the centre of the exposed a-Si there is evidence of the initiation point of the breakdown. Higher magnification of this initiation point is shown in figure 3.22 (b). Where a 1 $\mu$ m in diameter porous area can be seen in the centre of the image. This shows evidence of damage to the underlying a-Si layer from the initiation of the electrical breakdown of the gold electrode. The small size of this damage is likely due to the localised spark, which provides enough energy to cause damage to the underlying a-Si layer. The small-scale damage shown in figure 3.22 is of the length scale of microns and the length scale of the a-Si components fabricated is millimeters, the

difference in these length scales would suggest that this damage would have potentially low impact on the operation of the a-Si. Although there is potential for repeated damage to the gold electrode, due to sparking, could cause sufficient buildup of gold particles across the a-Si surface causing the device to be shorted. Therefore, care and attention is required in the design of the electrode spacing with regards to the expected operational voltage of the actuator device.

### 3.9 Numerical modeling of A-Si

*This work was conducted in collaboration with Yutian Zhang and Prof Martin Cryan (Department of Electrical and Electronic Engineering, University of Bristol). In this work the a-Si samples that were deposited were characterised by ellipsometry to identify the  $n$  and  $k$  coefficients of the a-Si samples as a function of wavelength. This data was supplied to Yutian Zhang [76] who used a numerical model of a-Si using facilities provided by Prof. Cryan to produce the plots shown in Figures 21,23,24 and 25. From this the theoretical resistance of the fabricated a-Si samples were calculated as a function of wavelength.*

In this section numerical modelling will be used to calculate the expected reflectance, absorptance, photoconductivity and resistance of the undoped a-Si: H (hydrogenated a-Si) deposited in this investigation.

#### 3.9.1 Absorption depth

In this model a sample layer of undoped a-Si:H (1347 nm thick as measure by ellipsometry) deposited on a glass substrate is considered. From the ellipsometry data collected in section 3.5 the refractive index  $n$  and extinction coefficient  $k$  to different optical wavelengths in air for the a-Si samples fabricated in section 3.3.1 are measured as a function of wavelength. The absorption coefficient  $\alpha$  and absorption depth ( $1/\alpha$ ) can be calculated by using the extinction coefficient  $k$  and the related optical wavelength in air ( $\lambda$ ) using the following equation [77]:

$$\alpha = 4\pi k/\lambda \quad (5)$$

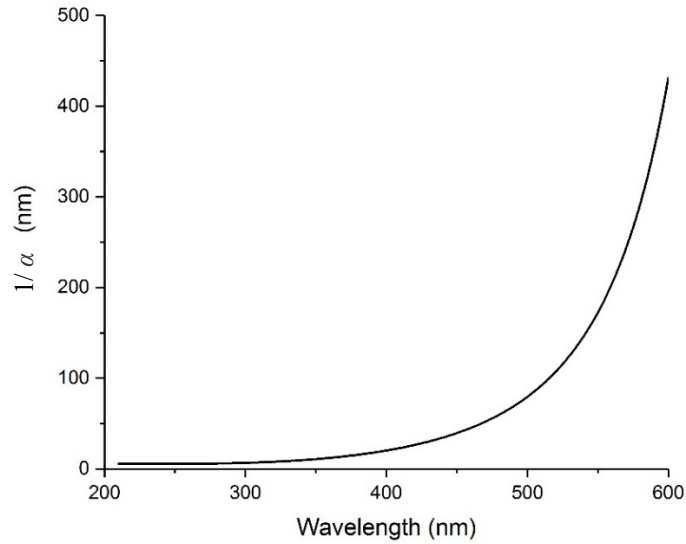


Figure 3.23 A plot showing the relationship between the theoretical optical wavelength in air and the absorption depth ( $1/\alpha$ ) between 200-600nm for a-Si. (Reproduced from [76]).

Figure 3.23 shows the absorption depth of the a-Si layer increases dramatically between 300-600nm. This shows that this range of wavelength would be the most effective range of light source to stimulate the resistance change of the a-Si layer. This wavelength range falls entirely in the visible wavelength spectrum (380nm -700nm). This has added benefits when considering a-Si's use with actuator designs as there is less need for specialised light sources such as high-powered lasers to stimulate the device and there is scope to use commercially available visible light sources.

### 3.9.2 Reflectance and absorptance

To derive the photoconductivity in a undoped a-Si: H layer, an infinite thickness of the undoped a-Si: H layer (i.e a sufficient thickness to absorb all the incoming light) is assumed [78]. This allows a simple two-layer model (air-a-Si) to be developed.

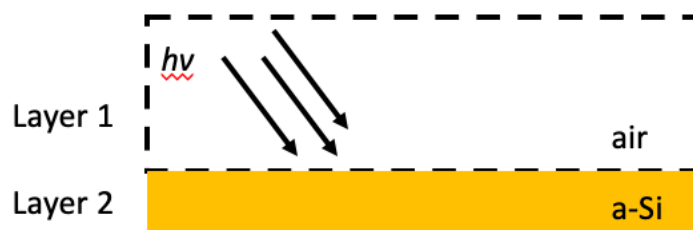


Figure 3.24: Schematic of the two-layer model developed to model the optical properties of the air/a-Si boundary.

The interfacial reflectance and absorptance can be calculated from the measured  $n$  and  $k$  values, with a frequency resolution of 10 nm. Absorptance is the effectiveness of the surface of a material to absorb radiant energy. The reflectance, the inverse of absorptance, was calculated using a transfer-matrix



method from the  $n$  and  $k$  values for the a-Si samples fabricated [79] and plotted in figure 3.25. This is a method of analysing the propagation of electromagnetic rays through a multi-layered material. This method encapsulates the effect of partial reflectance and absorption of radiation between multiple layers of materials and is more representative of the a-Si substrate than using a single interface model.

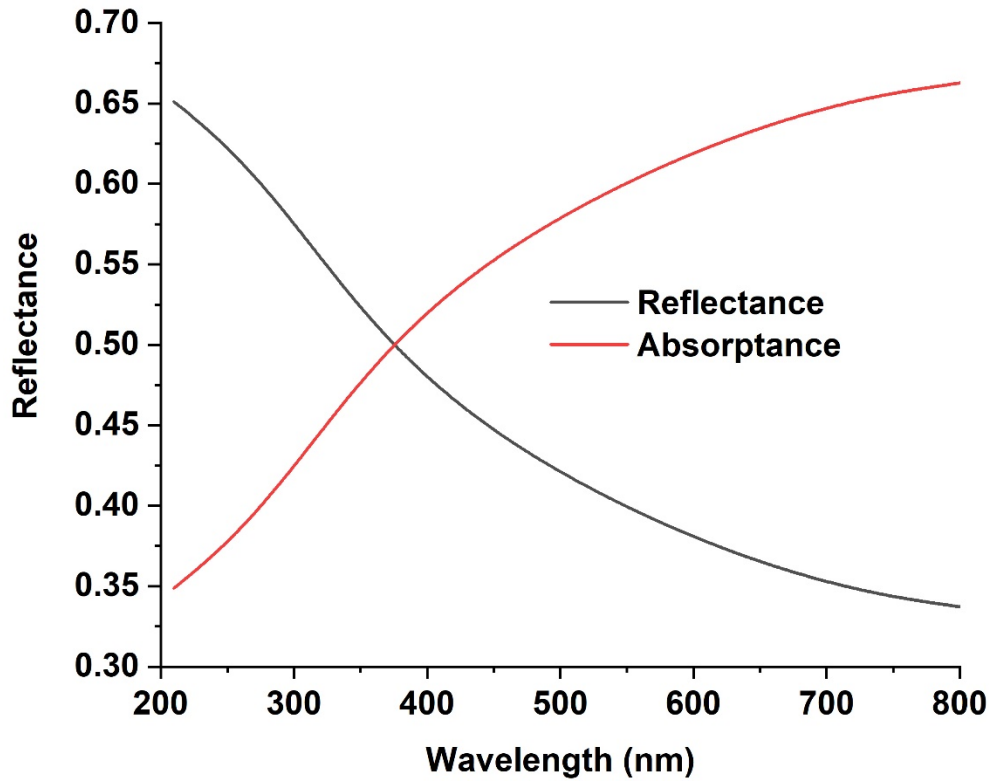


Figure 3.25: Shows the relationship between the optical wavelength in air and the interface reflectance and absorptance. (Reproduced from [76]).

Considering just the interface between the air and a-Si, figure 3.25 shows how the reflectance and consequently the absorptance of the a-Si/air interface changes as a function of wavelength. With a range of adsorption from 35% to 65% between the wavelengths of 200-800nm. Figure 3.25 highlights the inflection point of the absorptance of the incident light, i.e. when more than 50 percent of the incident light is absorbed by the a-Si. This is shown to occur around 380nm, which coincides with the range of wavelengths of visible light. This shows that visible light will be more effectively absorbed by a-Si.

In practice the two-layer model is not the most optimal to capture the absorption of light in a-Si as it does not consider the top oxidised layer of the a-Si. A matching layer of silicon dioxide (surface oxide found in a-Si) can be added to the model with a layer thickness equal to a quarter of the incident wavelength (shown in figure 3.26) to better represent the multi-layer nature of a-Si. This three-layer model will have interfaces between air and silicon dioxide ( $\text{SiO}_2$ ) and  $\text{SiO}_2$  and the a-Si. The reflectance

and absorptance for the three-layer model was calculated using a transfer-matrix method with the  $n$  and  $k$  values shown in figure 3.8.

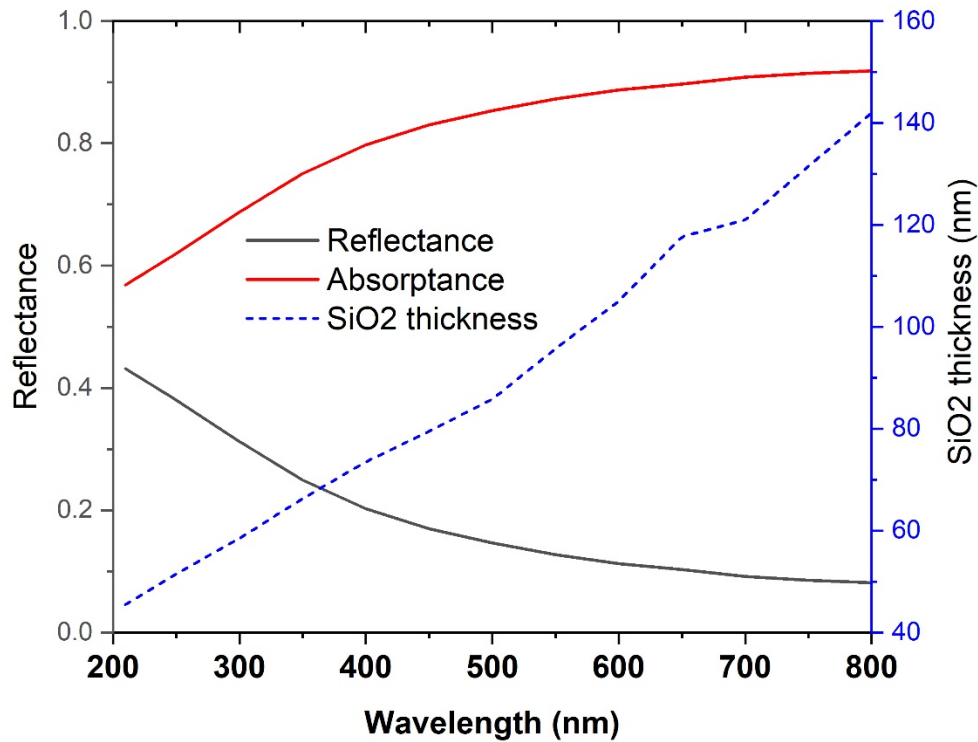


Figure 3.26: The relationship between the optical wavelength in air and the reflectance on the air-SiO<sub>2</sub> interface and the absorptance through the SiO<sub>2</sub>-aSi interface (along with the corresponding matching layer thickness). (Reproduced from [76]).

Figure 3.26 shows there is significant improvement in the light transmitted into the a-Si layer with the addition of a SiO<sub>2</sub> matching layer. Although this additional layer may not be necessary for the scope of this research however it is important to consider methods of improving our understanding of the material for future work.

### 3.9.3 Proprietary modelling of photoconductivity of a-Si

With the information from these models alongside specific data collected from literature it is possible to calculate the photoconductivity of the a-Si at increasing thickness depth as a function of wavelength. Photoconductivity is the phenomenon by which a material shows an increase in electrical conductivity from the presence of electromagnetic radiation such as visible light. Using a numerical model written by Yutian Zhang which calculates the photoconductivity of multi-layer thin film semiconductors, the photoconductivity of the a-Si samples fabricates was calculated. In this model the key material properties of the a-Si samples were used to make this calculation. These parameters are listed below

The key parameters are:

- Absorption coefficient: calculated from transfer-matrix method.
- Recombination time:  $2.1 \times 10^{-2}$  s [80]
- Diffusion length:  $8.66 \times 10^{-7}$  m [80]
- Surface recombination velocity:  $4.5 \times 10^{-4}$  m/s [80]
- Electron mobility:  $7.95 \times 10^{-6}$  m<sup>2</sup>/Vs [81]
- Hole mobility:  $4.5 \times 10^{-10}$  m<sup>2</sup>/Vs [80]
- Intrinsic carrier concentration:  $2.36 \times 10^{21}$  /m<sup>3</sup>
- Internal quantum efficiency: wavelength-dependent, peaks at 68.9% at 560 nm
- Absorptance: calculated from transfer-matrix method
- The optical intensity is set to 2.48 W/cm<sup>2</sup>

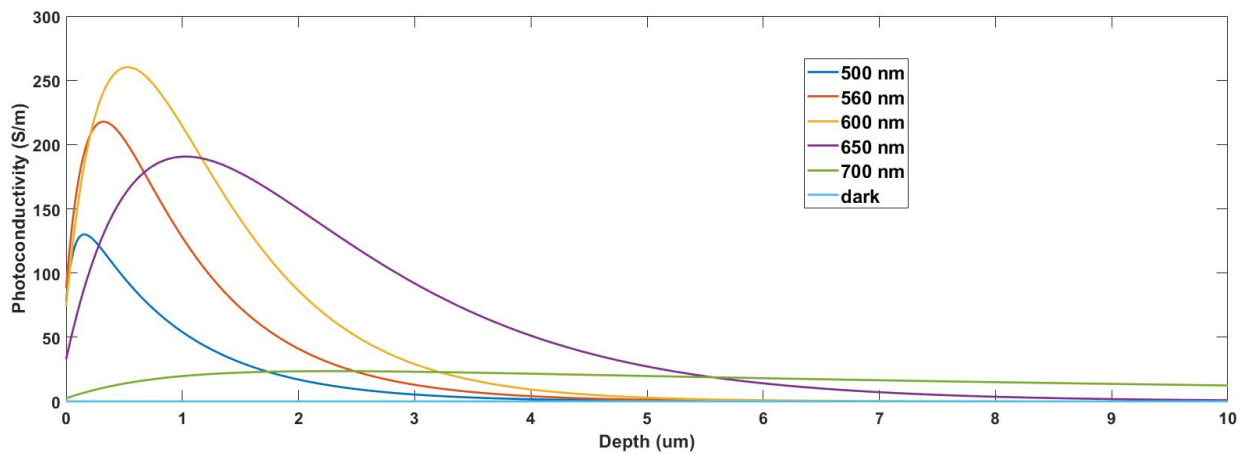


Figure 3.27: The curves of photoconductivity to depth into the undoped a-Si: H layer for different wavelengths of the light source. (Reproduced from [76]).

Figure 3.27 shows that the maximum photo conductivity of around  $260 \text{ S m}^{-1}$  can be achieved by using a wavelength of 600nm. The photoconductivity of the a-Si samples was calculated using a Matlab script written by Yutian Zhang from the  $n$  and  $k$  values of the a-Si samples [76]. Higher wavelengths show a drop in photoconductivity. This shows that ideally operational wavelengths should not exceed 600nm. In addition, in figure 3.27 the wavelengths 500, 560 600 and 650nm tested (centre of the visible spectrum) all have peak photoconductivity found before or around a thickness depth of  $1 \mu\text{m}$ . Therefore, it is not necessary to deposit layers of a-Si that are thicker than  $1 \mu\text{m}$  as there is no improvement of the photoconductivity of the material. This opens up the potential to use thin depositions of a-Si to maximise mechanical flexibility whilst maintaining the desired photoconductivity.

### 3.9.4 Calculation of resistance of a-Si

To calculate the total resistance of photo-induced plasma regions in the undoped a-Si layer, we assume the optical spot is square with an area of  $w$ . The total resistance is then calculated as follows:

1. Layer the undoped a-S layer with an infinitesimal individual thickness of  $dt$  ( $t$  is the depth into the undoped a-Si: H layer);
2. Calculate the conductance,  $dG$ , of each layer, assuming a constant photoconductivity for each layer, following Ohm's law: [82]

$$dG = \frac{\sigma w}{l} dt, \quad (6)$$

where  $\sigma$  is the photoconductivity of each layer,  $w$  and  $l$  are the width and length of each plasma layer respectively. The plasma layer is a layer of material excited by photons

3. The total conductance,  $G$ , can hence be expressed as by integration.

$$G = \sum dG = \int_0^{+\infty} \frac{w\sigma(t)}{l} dt, \quad (7)$$

where  $d$  is the depth into the undoped a-Si layer.

4. The total resistance can then be expressed as the inverse of conductance [82]

$$R = \frac{1}{G}, \quad (8)$$

Setting  $w = 1\text{mm}^2$ , to be a representative area of considerable length scale larger than that of the material thickness, the total resistances for different wavelengths of the light source are shown in Table 1.

Table 3.3 Total resistances of a-Si ( $0.84\mu\text{m} \times 1\text{mm} \times 1\text{mm}$ ) for different wavelengths of the light source [76].

Wavelength (nm)	500	560	600	650	700
Volumetric Resistance ( $\Omega$ )	318.4	303.8	290.1	278.7	301.8

As can be seen from table 3.3 the resistance of the plasma layer of a-Si reduces from 500nm to 650nm where it reaches its lowest value of 278.7 $\Omega$ . After which the resistance begins to increase again with the wavelength. Therefore, it can be inferred that for a-Si the lowest resistance of a-Si is seen at a wavelength of 650nm which would correspond to the ultraviolet (UV) end of the visible light spectrum. However, there are safety considerations to be made when using high powered UV sources. Table 3.3 also shows that at all the wavelengths tested the resistance calculated is of the same order in magnitude. As the starting resistance at low light intensity has been shown to be of the order of G $\Omega$  it is clear that the intensity of the light used has a much larger impact on the resistance change than the specific wavelength of light.

### 3.10 Characterisation Summary

In this chapter the manufacturing and performance of a-Si has been characterised using a variety of techniques. This was in order to establish the material properties of a-Si so that the most suitable electrostatic actuator could be chosen. In terms of manufacturing, both SEM and AFM microscopy techniques highlighted that manufacturing a-Si on a glass substrate was the most appropriate method to reduce the number of defects in the a-Si layer in comparison to the ITO coated glass substrate. This was supported by the high voltage testing where the glass substrate samples were able to withstand multiple ramp tests at high voltage where the ITO substrate samples experienced electrical breakdown due to the considerably shorter current paths of in the ITO samples (shown in figure 3.11). Thus, it was concluded that a simple glass substrate would be the best starting point for tests with electrostatic actuators to ensure the highest quality and consistency of sample.

Measured ellipsometry data gave values of the thickness of the deposited layer of a-Si, as well as the refractive index ( $n$ ) and extinction coefficient ( $k$ ). These were valuable in the numerical modeling of the a-Si sample where the potential to reach as low a resistance as  $278.7\Omega$  was calculated. It was also shown through numerical modeling that in order to optimise the photoconductivity of the a-Si layer there is no benefit to depositing a layer of thickness greater than  $1\mu\text{m}$ , as increasing beyond this depth causes a decline in photoconductivity for all wavelengths. Finally, numerical modeling also informed that the specificity of the wavelength, provided that it is within a range suitable to excite the a-Si (500nm-700nm), serves only to change the resistance of the material by a small amount. Whereas, increasing the light intensity showed resistance changes of the order of several magnitudes (Highlighted in table 3.3). Improvements, on a simple two-layer model (air/a-Si) were made by adding a wavelength matching oxide layer of  $\text{SiO}_2$  with a thickness of a quarter of the wavelength of the light source. This was shown to improve the absorption into the a-Si layer model.

Low voltage (1-5V) electrical testing showed that a-Si when compared to a commercially available LDR had significantly higher inherent resistance. The high inherent resistance of a-Si was demonstrated to be beneficial at high voltage, where it was shown to be stable when deposited on a plain glass substrate. This was not the case for the LDR and ITO glass coated samples which broke down at high voltage. Therefore, demonstrating that depositing a-Si on a plain glass substrate is most appropriate for high voltage applications.

To test the time dependent response of a-Si at high voltage a square wave voltage input was used to replicate that of a typical actuation mode. It was found that the a-Si behaved with a linear current response at all voltages tested (1.5-5kV) at low light intensities. As the light intensity was increased this current response became increasingly non-linear, showing an exponential response at 4.5kV and

41kLux. The threshold for this change from linear to non-linear response was found to be approximately 3kV. This further supports the potential for a-Si to achieve large changes in resistance which would be beneficial for actuator applications. An explanation of this transition effect was hypothesised that over time due to the higher electric field at higher voltages (4.5kv) the randomised dipoles of the a-Si could reorientate with the applied electrical field across the sample leading to a dramatic change in the resistance of the material. Although further work in this area will need to be conducted to better understand this observed transition. One concern in testing was the potential effects from thermal energy transfer to the a-Si from exposure to a high intensity light source. Prolonged exposure to the elevated temperatures of the high intensity light sources showed no change in the current response of the a-Si during a ramp test.

A concern over potential damage to the a-Si due to continuous exposure to high voltage was considered. To investigate this a sample that was tested at high voltage was imaged using an SEM. The microscopy showed evidence of damage to the gold electrode due to surface sparking at around 5kV. The gold vapourised and was shown to be deposited as small particles across the a-Si surface. The SEM showed no evidence of damage or change to the a-Si surface except for a 1 $\mu$ m diameter site of damage at the gold electrode where the spark was thought to originate. The length scale of this damage (microns) is significantly smaller than the length scale of the a-Si sample (millimeters) therefore, it is proposed that this damage is unlikely to affect the operation of the a-Si. However, an accumulation of this damage could create an area of damage significant enough to impact the operation of the a-Si.

### 3.11 Conclusion

In conclusion, through the characterisation techniques explored in this chapter it can be proposed that the requirements for developing a-Si and for use alongside an electrostatic actuator are:

- Plain glass substrate,
- Layer thickness of less than or equal to 1 $\mu$ m,
- Visible wavelength of light (ideally 650nm).

It can also be said that there is more potential for research in exploring high voltage applications of a-Si, such as for use alongside electrostatic actuators like dielectric elastomers actuators (DEA). A significant two-order-of-magnitude change in resistance was observed from increasing the light intensity from an ambient 62Lux to 42kLux with a potential theoretical lowest resistance of 287.7 $\Omega$ . From the characterisation of a-Si presented in this chapter we will look to develop an experimental proof of concept of optical control of a DEA using a-Si as a switch. This will be explored in the next chapter.

## Chapter 4: Control of dielectric elastomer actuators using amorphous Silicon

*The work presented in this chapter was published in a conference paper: C. Gillespie, A. Marzo, F. Scarpa, J. Rossiter, and A. T. Conn, "High- voltage photonic switching of dielectric elastomers with amorphous silicon thin-films," Electroact. Polym. Actuators Devices ( EAPAD ), vol. 10966, 2019. [83]*

### 4.1 Introduction

There are many classes of electrostatic actuators that operate at higher voltages with lower current demand that would pair well with the amorphous silicon (a-Si) on glass substrate developed in the previous chapter. The most common of this class of actuators is the dielectric elastomer actuator (DEA) [20]. DEAs are appealing for soft robotic applications due to their high work density and strains [13]. In this chapter we look to use the characterisation of a-Si in chapter 3 to develop an optically switched DEA using a-Si.

Control of electrostatic actuators such as DEAs in soft robotic research relies on external componentry due to the lack of imbedded control from the actuator. Control of DEAs typically involves methods of adjusting the input power signal. This can be done by smoothly varying the power supply voltage or through digital switching of the supply. When considering multiple DEAs in a system typically, MOSFETs or relays can be used to switch individual actuators on and off within a robotic system. In a field of research that strives for increased compliance from devices there is an opportunity to look towards functional materials such as amorphous silicon (a-Si) to be used as thin film switches to control the input power supply to the DEA using changes in light intensity. To create light-controlled electrostatic actuators, external components such as light dependent resistors are required to provide the actuation signal to the actuator when the correct stimulus thresholds have been applied. As shown in chapter 3, an LDR would need to be separated from the power supply due to the high voltages required by a DEA. In this chapter, we present a high voltage a-Si receptor that responds to the changes in the environmental lighting intensity and can be used directly in series with a DEA. The light responsive changes in resistance of an a-Si element are used to modulate the voltage applied across the DEA and thereby control its actuation.

In this chapter the following topics will be discussed:

- DEA design configurations are given in section 4.2.1,
- Fabrication of a DEA is given in section 4.2.2,
- Theory of DEA use with a-Si given in section 4.3,
- Experimental methods in section 4.3.1,
- DEA testing with a-Si given in section 4.4,

#### 4.2 Dielectric elastomer actuators

DEAs undergo out-of-plane as well as in-plane actuation by exploiting compliant electrodes and elastomeric dielectric materials [84]. There are other high voltage, low current electrostatic zipping actuators such as the Peano-HAZEL [17] and DLZ actuators [16], each offering benefits such as increased specific strains and blocking forces equivalent to skeletal muscle. Further details can be found in chapter 2, section 2.4 and 2.5. At the preliminary stages of development of the use of a-Si as a functional material for these actuators presented in this thesis, DEAs were chosen due to their ease of fabrication, high achievable strains and flexibility in design configuration which allow for complex modes of actuation.

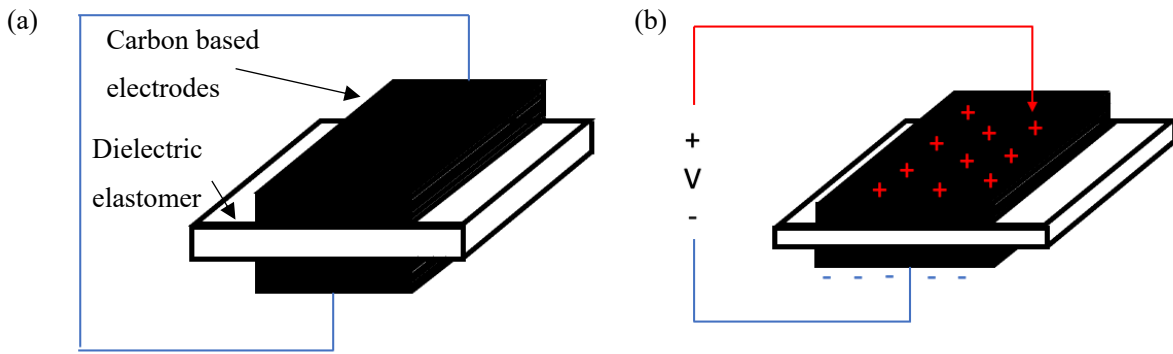


Figure 4.1: (a) Schematic of a DEA under no applied voltage. (b) Schematic of a DEA under applied voltage showing thinning and in plane stretching of the membrane.

Figure 4.1 shows a basic cross section of a DEA which consist of a thin dielectric elastomer layer that separates two compliant electrodes typically made from carbon-based composites such as carbon grease. The dielectric membrane can be pre-strained biaxially to improve actuation and held in place by a fixing ring such as laser cut acrylic [20]. An electric field-dependent Maxwell pressure is generated between the two electrodes by applying a potential difference between them. The Maxwell pressure,  $P$ , generates through-thickness compression and biaxial expansion of the dielectric elastomer membrane and is determined by equation (1) [85].

$$P = \epsilon_r \epsilon \left( \frac{V}{T} \right)^2 \quad (1)$$

Where  $\epsilon_r$  is the relative permittivity of the dielectric elastomer and  $\epsilon$  is the permittivity of free space ( $= 8.859 \times 10^{-12}$  F/m).  $V$  is the applied voltage and  $T$  is the membrane thickness of the DEA.

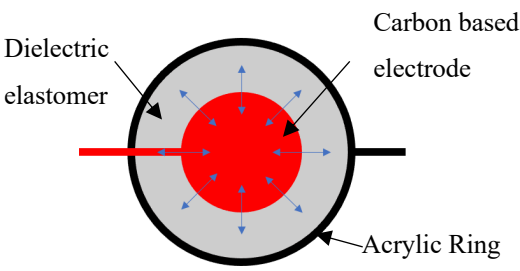
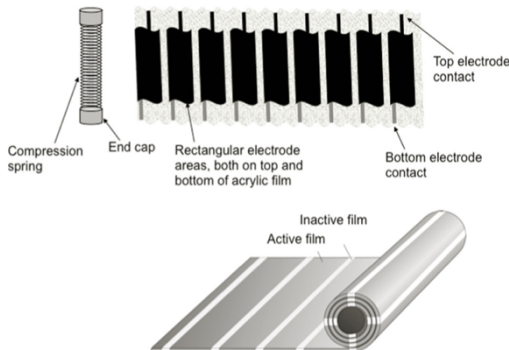
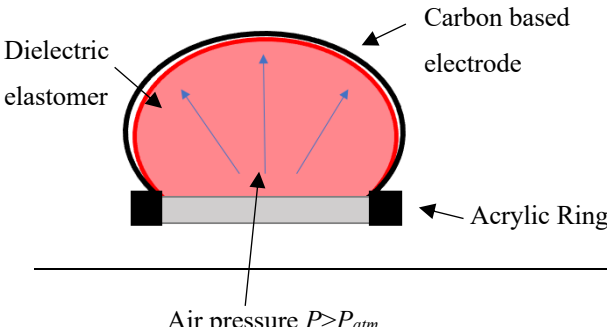
Typically, the applied electric field is of the order of  $100 \text{ V}\mu\text{m}^{-1}$ , with operational voltages of 2-5kV [86].

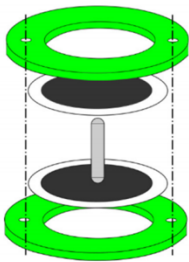
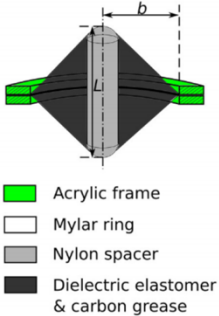


#### 4.2.1 DEA Configurations




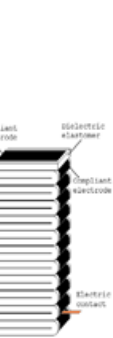
One of the advantages of DEAs is the adaptability of the design, by which plain strain, out of plane displacement and multiple degrees of freedom actuation can be achieved by altering the configurations of the actuator. Here a number of common DEA configurations will be considered to establish the common actuation mode and to investigate which is best suited for preliminary studies with a-Si. Table 4.1 contains a list of common DEA configurations and their outputs.

Table 4.1: List of common DEA configurations (after A.Hinitt [87]).

Actuator Depiction	Type	System Output	Actuation
	Planar film [85] (Spot DEA)	Planar biaxial expansion	Planar expansion
	Spring roll [88]	Spring assisted bending and elongation	Cylindrical expansion
Reproduced from Pei et al. [88]			
	Diaphragm [89]	Volumetric expansion or peak translation	Nonlinear biaxial strain

Exploded view	Cross sectional view	Antagonistic cone [90][91]	Linear pair translation	Nonlinear biaxial strain
				

Reproduced from Cao et al [90]

(a)	(b)	(c)	(d)	Stacked layers [92]	Transverse contraction	Planar expansion
						

Reproduced from Brochu et al. [22]

#### 4.2.2 Planar film DEAs

In-plane DEAs are one the most common configurations for actuator designs in research. Planar film DEAs include two flat electrodes on either side of a single actuator membrane. This leads to in-plane actuation by the biaxial expansion of the active electrode region of the membrane. The pattern of the electrode can be altered to change the desired actuation mode. The most common electrode patten is a simple spot electrode that can achieve biaxial in-plane expansion of the electrode area with the application of voltage.

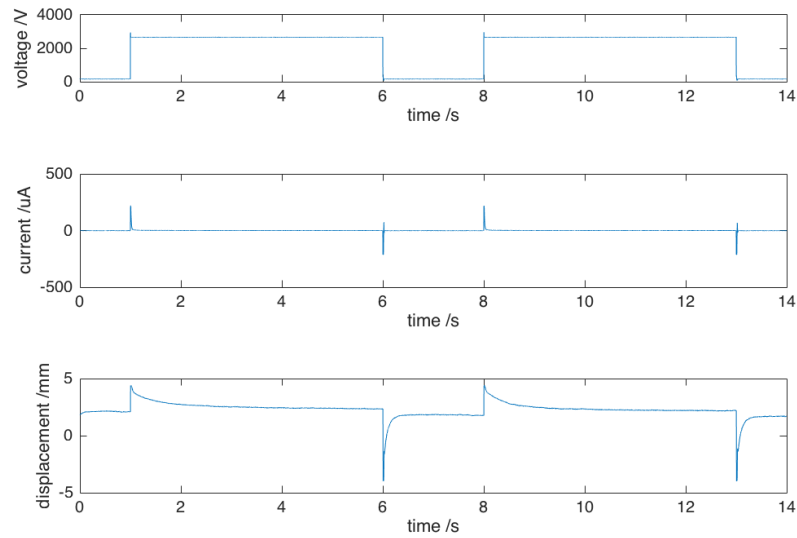


Figure 4.2: Plot showing the typical; voltage, current and in-plane displacement measurements from a DAQ for a weighted spot DEA actuator (shown in figure 4.6) (internal diameter 100mm, electrode diameter 50mm).

Figure 4.2 shows the typical current and displacement response for a planar spot DEA with a high voltage input, details of this test are shown in Appendix B. As can be seen from voltage and current data in figure 4.2, DEAs behave similarly to a capacitor in terms of their electrical response [20]. After the initial application of high voltage, the DEA initially charges as seen by the spike in current. Following this, the membrane continues to charge until a steady state is reached and the displacement is constant. When the voltage is then removed from the DEA there is a sudden discharge followed by a slow relaxation from the DEA until the actuation stops. An aperture design has also been presented which has a central circular passive region and an annular electrode ring which leads to contraction of the passive aperture as the electrodes expand [65].

#### 4.2.3 Out of plane Cone and diaphragms DEA

The cone and diaphragm DEA designs are both examples of DEAs that can achieve out-of-plane displacement and in the case of the cone DEA, multiple degrees of freedom actuation [91]. The double cone DEA design has two membranes separated by a central spacing rod. This spacing rod is used to separate the two films which have electrodes patterned so that they can be used independently as shown in figure 4.3.

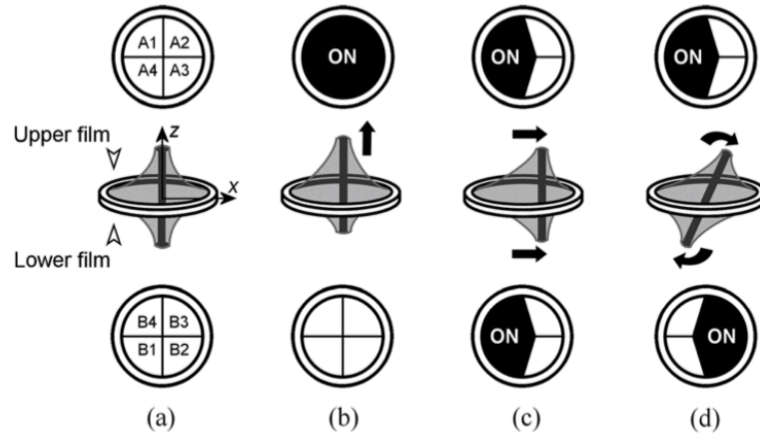


Figure 4.3: Double cone DEA principles of operation (a) the electrode arrangement for the upper and lower film. (b) Method of antagonistic displacement vertically. (c) Method of translation of the central spacer. (d) Out of plane twist of the spacer. Reproduced from [91].

Figure 4.3 shows methods of achieving actuation with multiple degrees of freedom with the double cone actuator design. Multiple different actuation modes can be achieved from the same actuator by applying voltage to segmented electrodes around the structure. This can be controlled to give antagonistic, translational and rotational modes shown. This DEA design has also been shown to have applications as peristaltic pumps [25] [26] and walking robots [93].

Diaphragm DEAs can also exhibit out of plane actuation by using coupled membranes separated by air or liquid [94][95]. This allows for an active membrane and a passive membrane of the diaphragm. The passive membrane can be isolated from the high voltage supply allowing for potential interactive or adaptive surfaces that are safe to touch [96].

#### 4.2.4 Stacked DEA

Stacked DEA designs aim to increase the magnitude of through thickness actuation [97] [98]. This is done by the accumulative effect of stacking multiple layers of DEA actuators on top of one another to achieve a larger global actuation when voltage is applied. Stacked actuators can reduce need for a retaining ring and pre strain of the membrane. Instead, the actuator can form a self-supporting stack.

#### 4.2.5 Spring Roll DEAs

Rolled DEAs as shown in table 4.1 are fabricated from a single roll of elastomer with a patterned electrodes which increase the work density of the actuator, allowing for applications such as bio-inspired flapping robots [99]. The ‘spring roll’ DEA is an example of a rolled DEA design [100] that uses a central spring instead of the elastic pre-strain typically seen in a DEA membrane [88]. Similar to

the cone DEA, multiple degrees of freedom and complex actuation can be achieved with this design. However, its complexity often leads to difficulty in fabrication and premature failure of the DEA in use [88].

#### 4.2.6 DEA fabrication

The fabrication of prototype DEAs is relatively straightforward and can be conducted with minimal specialist lab equipment. However, the quality of the fabrication process can have a direct impact on the performance of the DEA so care and attention is required to ensure the process is controlled and repeatable. The dielectric elastomer used for the DEAs in this work was 3M 4905 VHB tape with carbon grease (MG Chemicals) for the surface electrodes. The step-by-step process for the fabrication process for a planar film DEA (depicted in table 4.1) is highlighted in figure 4.4:

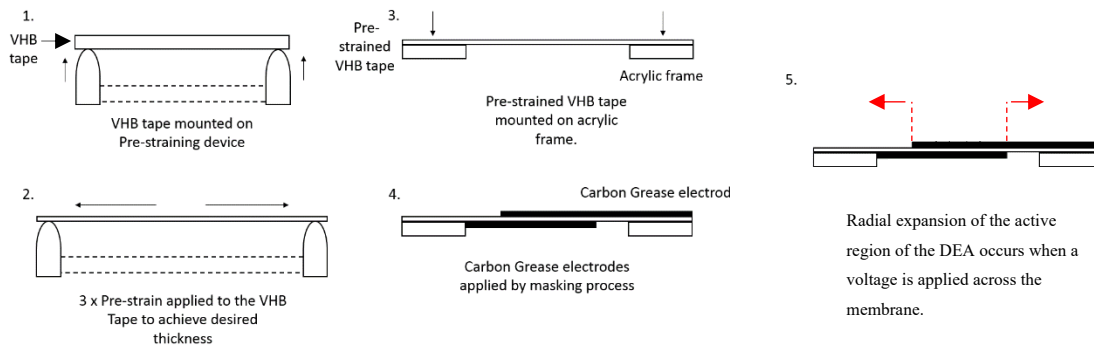


Figure 4.4: Graphic showing the basic five step process for the manufacture of a DEA spot actuator.

The steps shown in figure 4.4 highlight the key stages of the fabrication process of a DEA. Initially, the VHB 4905 tape is cut to size and the backing tape removed. The tape is placed on a radially expanding biaxial strain device, which consists of a series of connected arms which concertina to maintain a uniform biaxial strain [101]. This device is designed to achieve a 4x4 biaxial pre-strain of the dielectric membrane. Laser cut acrylic rings (internal diameter, 60mm, external diameter 70mm) are placed on either side of the stretched membrane. Even pressure is applied around the rings allowing the VHB 4905 membrane to adhere to the acrylic. The radially expanding device is then removed and the biaxial strain in the membrane is maintained by the acrylic rings. The excess VHB 4905 around the edge of acrylic rings is cut away with a scalpel.

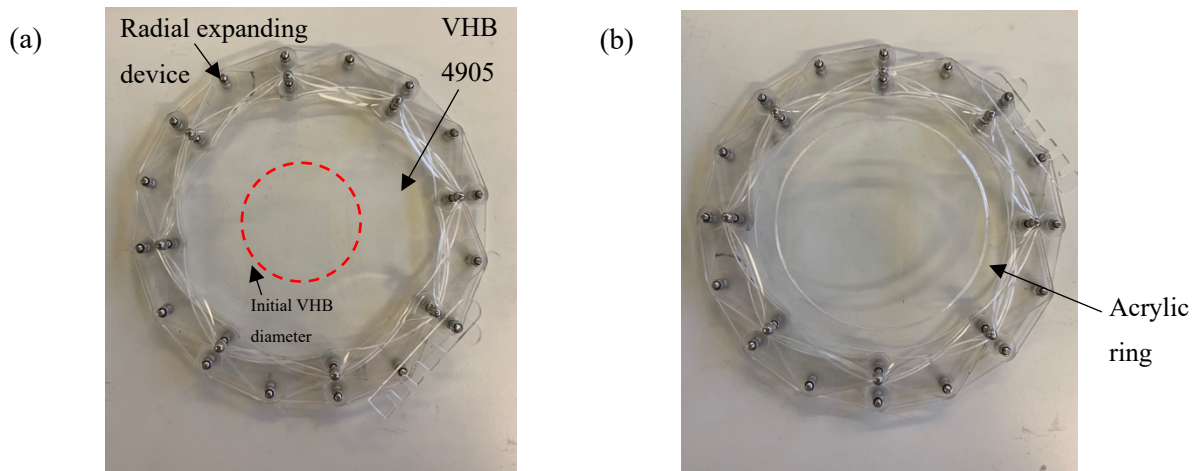


Figure 4.5: (a) Image showing the stretching of the VHB membrane using a radially expanding pre-strainer (b) Image showing the installation of the acrylic retaining ring.

The process of pre-straining the VHB 4905 membrane is shown in the images in figure 4.5 where the VHB tape is strained the appropriate amount with a radially expanding device shown in figure 5 (a) and the pre strain is maintained using an acrylic ring shown in figure 4.5 (b). Using a Cricut computer aided manufacturing cutter, a non-adhesive polymer film mask was cut to the desired shape of the passive region of the actuator. The masks are then placed on either side of the VHB 4905 membrane to mask out the electrode pattern. Carbon grease is then carefully applied to the surface of the unmasked area. Care and attention is taken to maintain an even layer thickness of carbon grease on both sides of the actuator. Once the carbon grease is applied, the mask is then removed. The final stage of manufacture is to attach copper electrodes made from 3M 1181 copper adhesive tape to the outer ring of the DEA, each running to opposing electrodes. The carbon grease electrodes are connected to the 3M 1181 copper tape with a blob of carbon grease.

During fabrication, it is important to ensure that the pre-strain is uniform across the membrane. This can be done by controlled even stretching of the VHB 4905 film, as well as ensuring that the retainer rings are firmly adhered to the membrane all the way around the circumference. Any areas that are not fully adhered will creep back to a lower pre strain and this will lead to an uneven actuation of the DEA. Uneven actuation can also be caused by uneven and or patchy electrodes. It is also important to avoid touching the membrane as much as possible during manufacture. This is because contaminants can become initiation points for failure of the DEA. Such contaminants can include dust from the environment. The carbon grease used in the fabrication process is carcinogenic. Therefore, the correct PPE and safety precautions must be followed when fabricating DEAs.

#### 4.2.7 DEA summary

In summary, the relatively simple operating principle of DEA actuation can be used to create a wide range of mechanical outputs based on the configuration of the actuator or the patterning of the electrodes. In-plane expansion and contraction of the membrane film can be achieved using a pre-stained planar membrane. Out-of-plane actuation can be achieved by cone or diaphragm designs. Multiple degrees of freedom have been demonstrated with simultaneous control of multiple electrodes using, for example, the antagonistic cone and spring roll designs. DEAs can produce a number of different actuation modes that can be beneficial for a wide range of robotic applications. All of the designs discussed exploit the same Maxwell's pressure. Therefore, if it can be demonstrated that a-Si can be used to control a planar DEA, only small changes would need to be made to allow a-Si to be used alongside other DEA configurations. At the preliminary stage of integrating a-Si with DEAs in this research, a planar DEA configuration was selected for testing due to the simplicity of fabrication and analysis of the response of the actuator.

Table 4.1 shows many configurations of DEAs that can achieve complex actuation such as the spring roll and double cone designs. These DEAs require multiple electrodes in order to achieve this level of sophistication. Each independently activated electrode requires a separate high voltage supply. The use of multiple high voltage cables supplying each independent electrode can inhibit the design flexibility and scalability of DEAs. Hence, through the use of a-Si to remotely control which electrodes are being independently activated from a single high voltage supply is advantageous to producing compliant actuators that can achieve complex actuation.

#### 4.3 Development of an optically controlled DEA with a-Si

As a proof of concept of this technology, the next step in the development of optically controlled DEAs is testing of an a-Si sample in series with a DEA using the optical and electrical properties of a-Si from the characterisation presented in chapter 3. In this section the experimental methodology will be outlined as well as a quasistatic tuning of the electrical circuit to maximise the voltage across the DEA. For this investigation, a simple spot DEA with a central weight was used as shown in figure 4.6. The central weight creates a vertical displacement as the membrane actuates that can be measured by laser displacement.

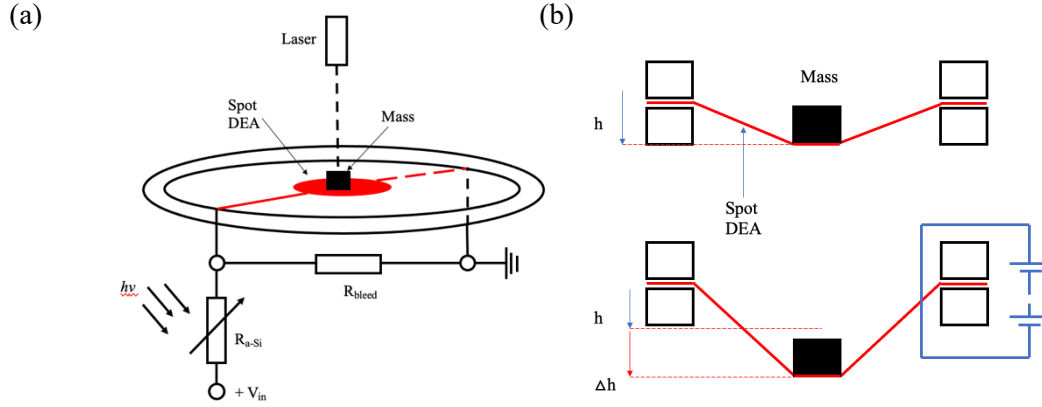


Figure 4.6: (a) Schematic diagram of a photonic controlled DEA using a-Si. (b) Side view showing actuation of the photonic controlled DEA.

Figure 4.6 shows a schematic diagram of a proposed photonic controlled DEA using a-Si and a weighted planar film DEA. The weighted planar film DEA uses a central mass placed on the DEA membrane to create an out-of-plane displacement when the DEA is activated. This vertical out-of-plane displacement can be measured using a laser (Keyence LK-GD152 and LK-GD500) providing an accurate and reliable measurement of displacement compared to measuring the radial expansion of a planar film DEA.

#### 4.3.1 Methodology

A sample of  $0.84\mu\text{m}$  thick a-Si was deposited onto a cleaned glass substrate following the steps highlighted in chapter 3 section 3.3, the sample size used was  $25.8\text{mm} \times 38.6\text{mm}$ . To ensure good electrical contact, the a-Si sample was mounted onto a specially designed printed circuit board (PCB) with gold connector pins either side of a central opening to allow light to pass. This mount was bonded to the PCB board with epoxy resin.



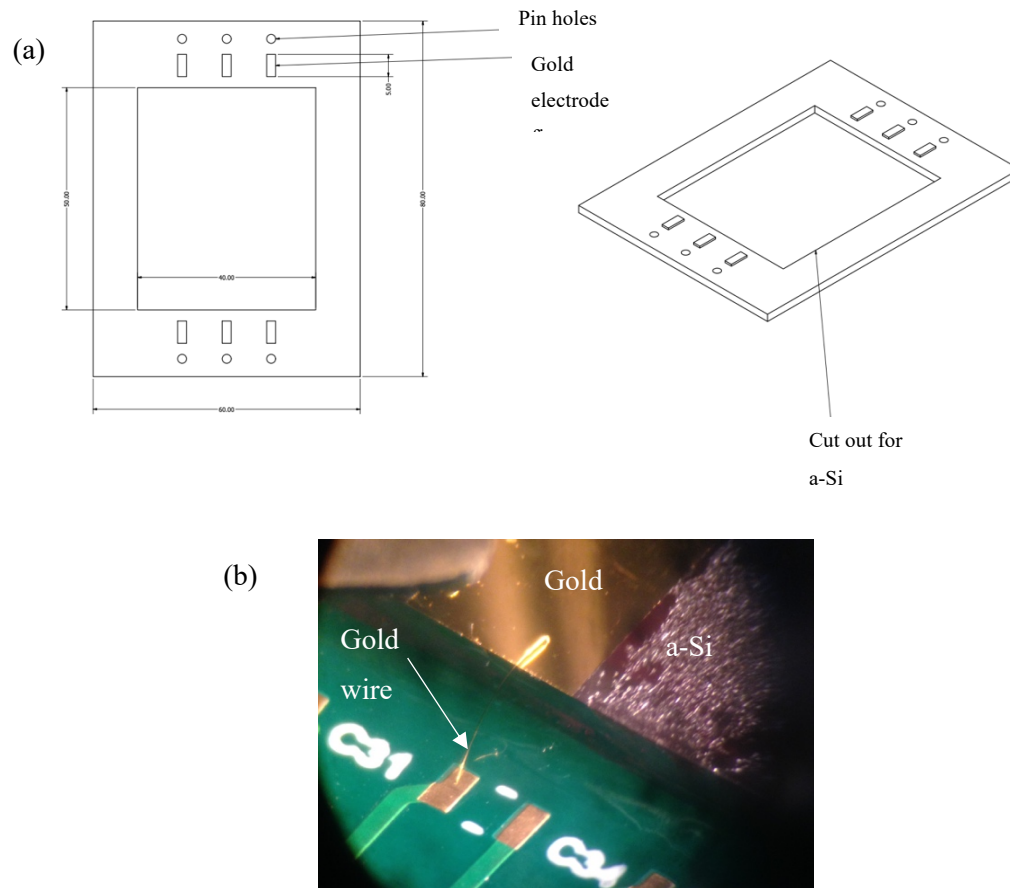


Figure 4.7: (a) Schematic of the a-Si mount (b) Microscope image of the arc bonded gold wire from the external PCB mount to the gold electrodes of the a-Si sample.

Figure 4.7 (b) above shows an image of the gold wire forming a permanent electrical connection between the PCB mounting board and the a-Si sample. Using an arc-bonding process a 5-micron thin gold wire was bonded between the two gold contacts between the a-Si and the PCB mount. This provides a secure and consistent electrical contact to the a-Si. Pin header connectors were then soldered to the PCB to allow the sample to be connected to the high voltage amplifier.

#### 4.3.2 Electrical circuit diagram

To better understand the experimental set up, each electrical component can be represented as equivalent electrical components to predict how the circuit will operate at high voltage. To make sure that charge can be removed from the DEA after actuation, a bleed resistor is needed in parallel to the DEA.

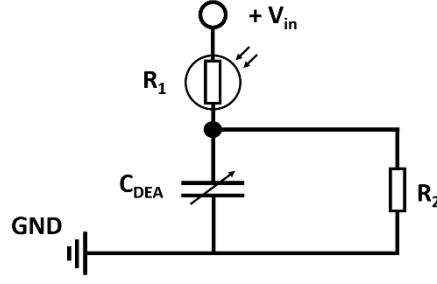


Figure 4.8: Schematic of the voltage divider circuit for the optically controlled DEA.

Figure 4.8 shows the schematic of the voltage divider circuit for the optically controlled DEA proposed, with  $+V_{in}$  representing the input voltage and GND the ground. In this circuit the a-Si labeled  $R_1$  acts as a light dependent resistor. The DEA can be represented by a variable capacitor when considering the electrical circuit in a quasistatic case rather than dynamically [102]. As mentioned previously, to ensure that the DEA discharges after actuation a bleed resistor, labeled in figure 4.8 as  $R_2$  was placed in parallel with the DEA. This sets up a voltage divider circuit at the junction point where  $R_2$  is connected between the a-Si and the DEA.

#### 4.3.3 Quasistatic tuning of the voltage swing across the DEA

The size of the voltage across the DEA can be calculated and tuned by controlling the resistance of the bleed resistor. The voltage divider will act to split the voltage applied to the circuit. This means that the voltage across the DEA will be a fraction of the input voltage ( $+V_{in}$ ). The voltage across the DEA can be calculated using the voltage divider equation shown in equation (2).

$$V_{out} = \frac{V_{in}R_2}{(R_1+R_2)} \quad (2)$$

Where  $V_{out}$  is the voltage across the DEA,  $V_{in}$  is the input voltage,  $R_1$  is the resistance of the a-Si and  $R_2$  is the resistance of the bleed resistor ( $R_2$ ). With an assumed input voltage ( $V_1$ ) of 3kV we can calculate the voltage across the DEA at two different quasistatic states using the resistance value of a-Si calculated in chapter 3 table 3.3. The first state is when  $R_1$  represents the resistance of a-Si under an ambient lighting condition  $R_{ambient}$  (62 Lux) and the second is when  $R_1$  represents the resistance under an illuminated light source (13kLux),  $R_{light}$ . Therefore, the voltage swing across the DEA between ambient and illuminated state can be calculated using the following equation (3).

$$\Delta V_{DEA} = \frac{V_{in}R_2}{(R_{light}+R_2)} - \frac{V_{in}R_2}{(R_{ambient}+R_2)} \quad (3)$$

Using the resistance values of a-Si estimated from experimental data in chapter 3 table 3.3 the value of  $\Delta V_{DEA}$  can be calculated for different values of bleed resistor.

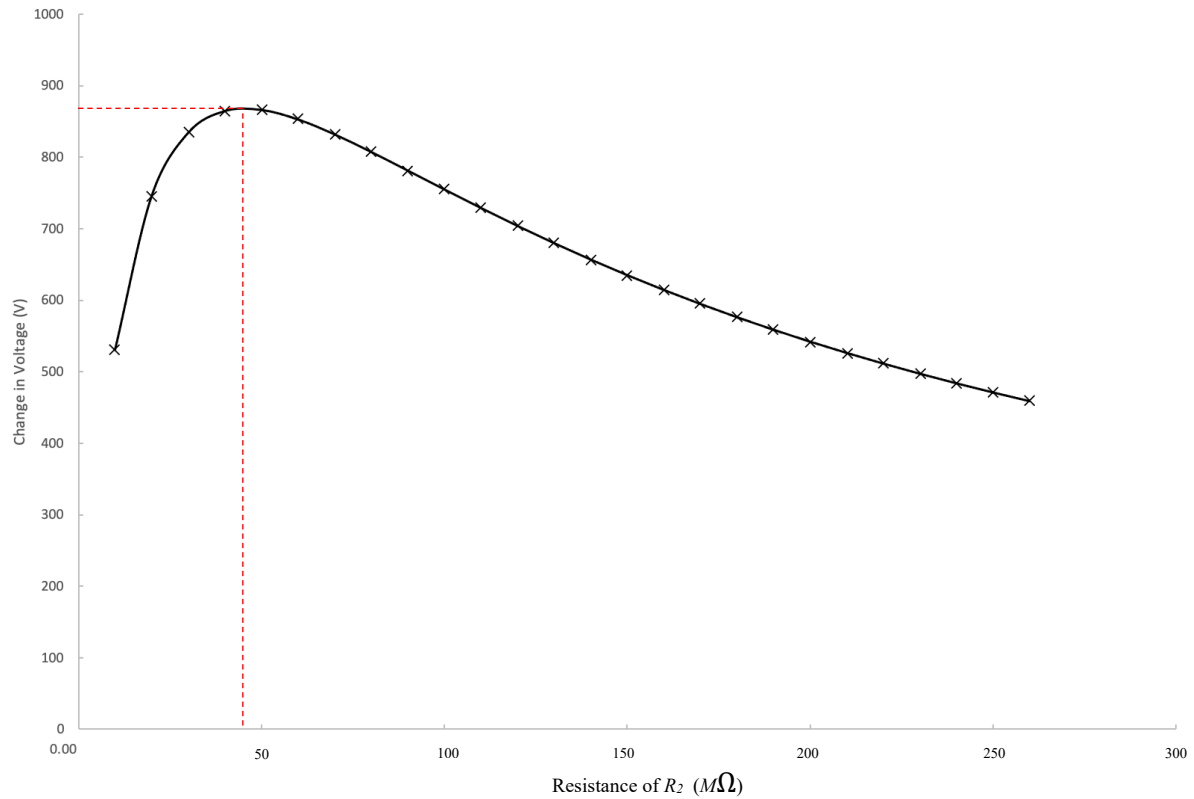


Figure 4.9: A plot showing the predicted change in voltage across the DEA between ambient and illuminated states as a function of increasing values of resistance of  $R_2$ . With an input voltage of 3kV.

Figure 4.9 shows a plot of the voltage swing due to illumination of the optically controlled DEA circuit, predicted using equation (3), for increasing values of bleed resistance from 0 – 300M $\Omega$ . As can be seen, there is an increase in the voltage swing across the DEA as the resistance of the bleed resistor is increased from 0M $\Omega$  to 50M $\Omega$  where a maximum voltage change of 866.1V at 49 M $\Omega$  is seen between the ambient and illuminated states. As the resistance value of the bleed resistor is further increased, the voltage swing begins to decrease gradually. Therefore, for this electrical circuit, a 50M $\Omega$  bleed resistance was selected, allowing for a theoretically voltage swing of around 866.1V between an ambient and illuminated state for the optically controlled DEA.

#### 4.3.4 Controlling the light source

Due to health and safety constraints on the use of high voltage this investigation was conducted in an electrically isolated high voltage box. Consequently, a method of controlling the light source remotely is required. An Arduino Uno controller was connected to a relay switch which was programmed with a loop function to turn the light source on for 5 seconds and then off for 10 second. This was repeated for

two complete cycles. This allowed for modulation of lighting conditions remotely as well as providing a means of consistent modulation between the two conditions.

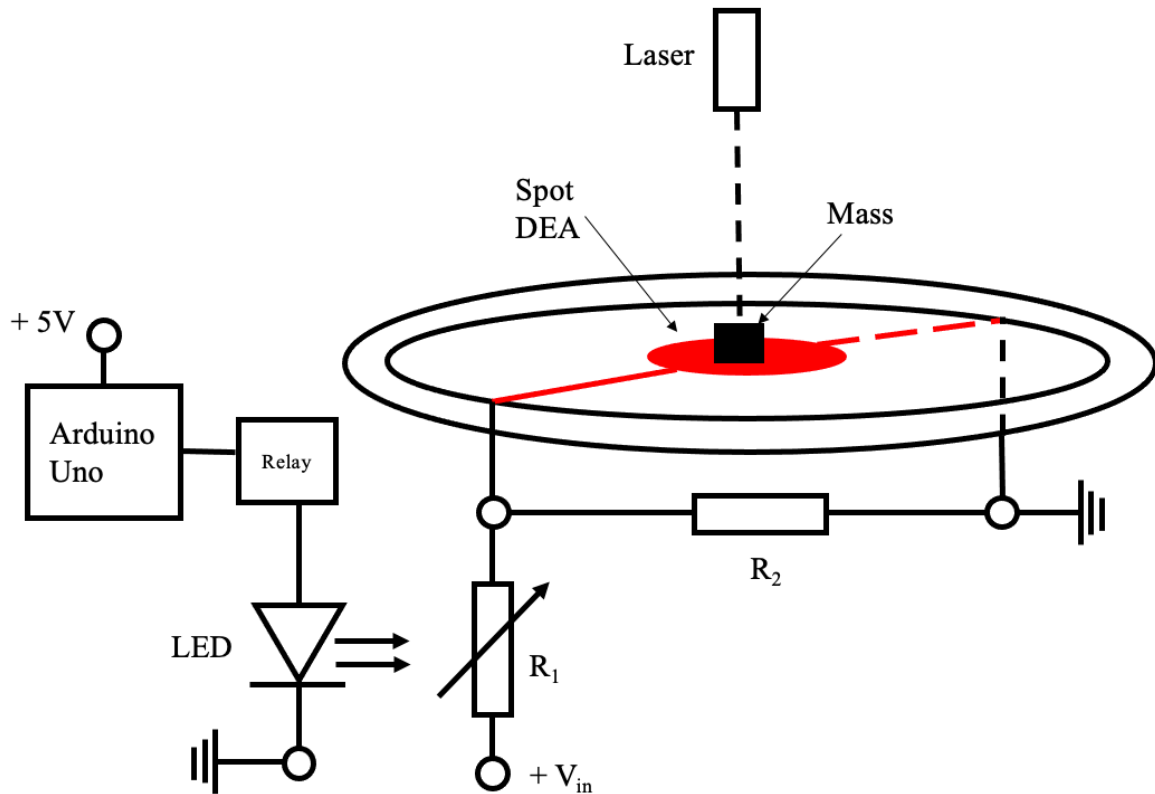


Figure 4.10: Schematic of the experiment set up for the optically controlled DEA.

The experimental set up is shown in figure 4.10 where the high voltage supply is connected to the optically controlled DEA circuit shown in figure 4.6. To measure the displacement of the DEA a small aluminium weight (9.1g) was placed in the centre of the passive region of the spot DEA to bias the membrane. This means that the planar expansion in the active area of the DEA membrane under an applied voltage causes a vertical displacement which can be measured using a laser displacement gauge (Keyence LK-GD152 and LK-GD500). The LED Light source is separated from the high voltage circuit, which is placed below the a-Si sample. The light source is connected to the Arduino controlled relay with a separate 5V supply.

A 3kV square wave voltage was applied to the optically controlled DEA after 5 seconds using a high voltage amplifier (Ultravolt 5HV A23-BP1) and the current and voltage signals were recorded using a data acquisition device (DAQ) (National Instruments BNC-2111). The 3kV supply was held on for 30 seconds. During the 30s of applied voltage, the light source was modulated by the Arduino relay as shown in figure 4.11.

## 4.4 Results

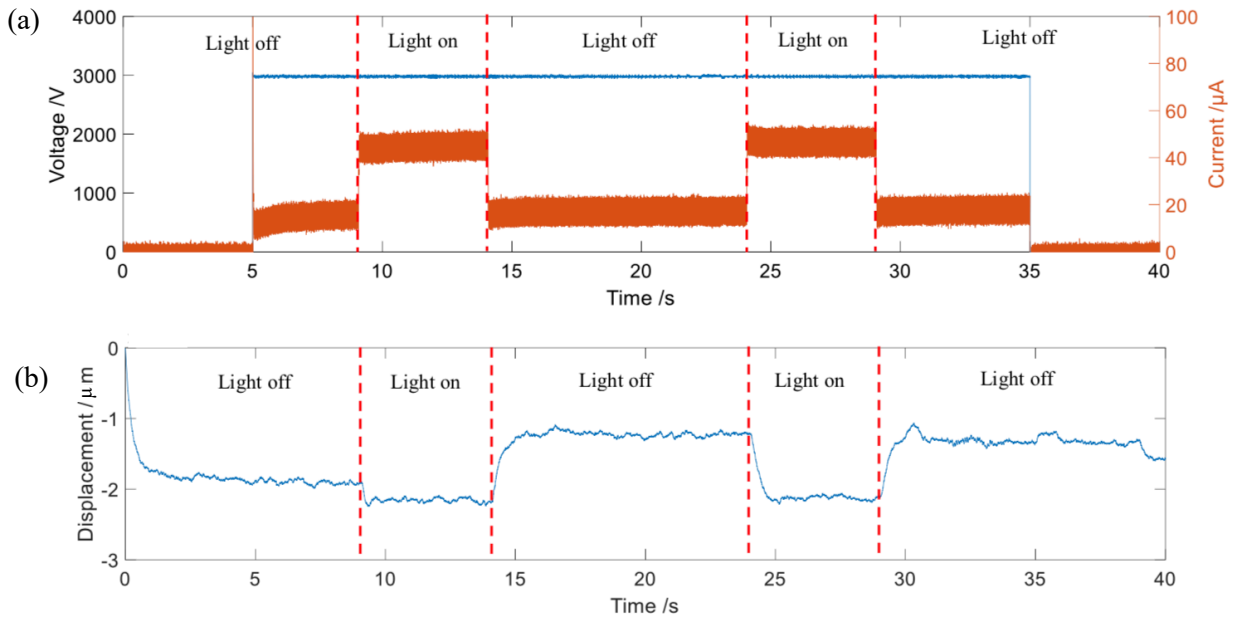


Figure 4.11: DAQ results for the experimental test of the optically control DEA showing the voltage, current and displacement of the weight-biased DEA actuator as a function of time. The illumination conditions have been overlayed in the plot.

As highlighted in figure 4.11, during the period of illumination a maximum mean achieved displacement of  $2.2\mu\text{m}$  was recorded with the laser displacement meter. The values of displacement are seen as negative in figure 4.11 as the weight biased DEA is below the laser displacement gauge and so it moves away from the gauge during actuation. The amplitude of displacement is consistent between the two regions of illumination (9 and 24 seconds). The displacement seen in the first off period (0 -10 seconds) is greater than the second (14-24 seconds) and third (29-40 seconds) which both share consistent displacement values. This is due to the fact that from 0-10 seconds there is no charge on the DEA and so therefore the DEA draws current to charge the membrane leading to a larger displacement in the initial off period. The period of 14-24 seconds and 29-40 seconds the DEA is already charged and so returns to a consistent displacement in the off periods.

## 4.5 Discussion

The optically controlled DEA showed actuations from an increase in light intensity. This result proves the concept that a-Si can be used to optically control the actuation of a DEA. However, as highlighted in figure 4.11 the mean displacement of  $2.2\mu\text{m}$  is very small and difficult to observe with the naked eye. Figure 4.11 also shows the low latency in current response of the a-Si which can be very desirable in the field of robotics where high frequency inputs are often used. The displacement of the DEA does show some latency in response, but this is likely due to the capacitive electrical behaviour and

viscoelastic mechanical behaviour of the DEA rather than the response of the a-Si. The displacement of the DEA in figure 4.11 also shows the actuator having a greater base line displacement when the 3kV voltage is applied (at 5 seconds) compared to the subsequent off periods. This is because in the initial case the DEA has no residual charge and therefore the initial off period also features the application of the high voltage to the DEA. For the subsequent periods of ambient illumination, the DEA will already be holding charge and will return to a steady state once the light source is turned off. This could help to explain why the 10 second periods of no illumination after the initially application of light shows repeatable ambient displacement values.

The small magnitude of the actuation recorded in this investigation, although significant in proving the hypothesis of using a-Si as a method of optical control of a DEA actuator, is not large enough to be useful for many robotic applications. One potential reason for the displacement of the DEA being small is that the light intensity applied to the a-Si was not enough to reduce the resistance enough to allow for enough voltage to reach the DEA. However, as calculated previously in section 4.3.3, an 866.1V swing should have been achievable with the voltage divider set up used in this investigation. This leads to the thought that the resistance of the a-Si is higher than expected from the predictions made in chapter 3 table 4.3. This could also be due to the geometry of the a-Si sample. For this investigation, a larger sample of a-Si was deposited to allow for wider spacing between the electrodes on the surface to reduce the risk of sparking and electrical breakdown (2.5kV per 5mm). A potential reason for the small displacement is that 866.1V is a small voltage to apply to a DEA in this context and the weight biased planar film configuration of DEA used is not the optimal design to show large displacements.

Methods of improving the actuation of the optically controlled DEA include increasing the intensity of the light source, reducing the resistance of the a-Si, and exploring alternative DEA configurations that generate a larger actuation stroke for a voltage change of 866.1V. Increasing the light intensity applied to the a-Si would lead to an increase in the resistance changes of a-Si which in turn would lead to increased actuation of the DEA. However, using a high intensity light source will increase the resistance change of a-Si, but it steps away from the goal to develop a soft robotic technology that can respond to environmental changes. If the intended outcome is to develop a soft robotic actuator that can be remotely controlled by an optically signal, then a high intensity source would be needed. In addition, increasing the input voltage above the 3kV tested would increase the voltage that reaches the DEA and therefore would in turn increase actuation. However, if the voltage across the DEA is too high (typically above 100 MV/m) there is an increased risk of electrical breakdown of the membrane.

In this investigation, the focus of research has been a-Si and its role in the development of an optically controlled actuator. Consideration needs to be made of the other ‘half’ of this system, the DEA. In order to have a larger output, consideration needs to be made around optimising the interaction between the

a-Si and the DEA as well as designing a DEA to fully utilise the calculated 866.1V swing between ambient and illuminated conditions proposed in this investigation. This could be done by adjusting the geometry or configuration of the DEA to further improve this actuation.

#### 4.6 Conclusions

In this chapter a proof of concept of an optically controlled DEA has been developed using a-Si as a light dependent resistor in series with a DEA operating under high voltage. The DEA was chosen as the electrostatic actuator to pair with a-Si due to its simple operation principle and wide range of potential outputs for future applications. This includes both in-plane expansion, contraction, and rotation with a planar DEA confirmation as well as out-of-plane actuation with cone, diaphragm, spring roll and stacked actuator designs. This wide range of actuation modes all stem from the same principle of Maxwell pressure on the dielectric membrane. Therefore, since optically controlled actuation has been demonstrated with a planar spot DEA, the principle can be transferred to optically control DEA confirmations with more complex actuation modes.

Using numerical modelling of the voltage divider circuit for the optically controlled DEA, it was shown that a theoretical 866.1V voltage swing between ambient and illuminated light conditions can be achieved using a 50M $\Omega$  bleed resistor. This was calculated from a voltage divider equation used in two quasistatic states, ambient and illuminated. The difference between these gives a prediction of the expected voltage swing across the DEA with an input voltage of 3kV. Testing the proposed design for an optically controlled DEA showed that at 3kV an actuation of 2.2 $\mu$ m of a weight biased spot was achieved when illuminating the a-Si with 51kLux for a period of 5 seconds. This demonstrated the concept of controlling a DEA with changes in environmental light intensity. The actuation was shown to be controlled and repeatable over the course of the 40 second test period. However, the achieved displacement by the DEA actuator was considerably lower than a typical DEA and of an order of magnitude that is not readily usable in many soft robotic applications. Therefore, considerations were made as to further improve the output of the actuator under illumination. It was proposed that in either the light intensity or the input voltage of the circuit would need to be increased. In addition, we should explore alternative DEA configurations which would better exploit the change in resistance and therefore applied voltage to the DEA from the a-Si. In the next chapter we look to refine the geometry of the DEA to better exploit the 866.1V swing achievable through changes in light intensity. This is done through controlled geometry of the DEA and exploitation of the transition between stable and unstable actuation of the DEA membrane.

## Chapter 5: Improving the actuation of an optically controlled DEA using wrinkling.

### 5.1 Introduction

In chapter 4, it was demonstrated that the change in resistance of a-Si between low (ambient) and high light intensities could be directly coupled to a dielectric elastomer actuator (DEA) to control its response. However, the first proof of concept optically controlled DEA presented in chapter 4 section 4.4 achieved an actuation displacement of only  $2.2\mu\text{m}$ , which is small compared to the displacement generated by conventionally-switched DEAs. From the conclusions in section 4.6 it was established that the weighted planar spot DEA used in section 4.3.4 (figure 4.1 (a)) may not be the best DEA configuration to make use of the 866.1 V change across the DEA from the change in resistance of the a-Si under different light intensities.

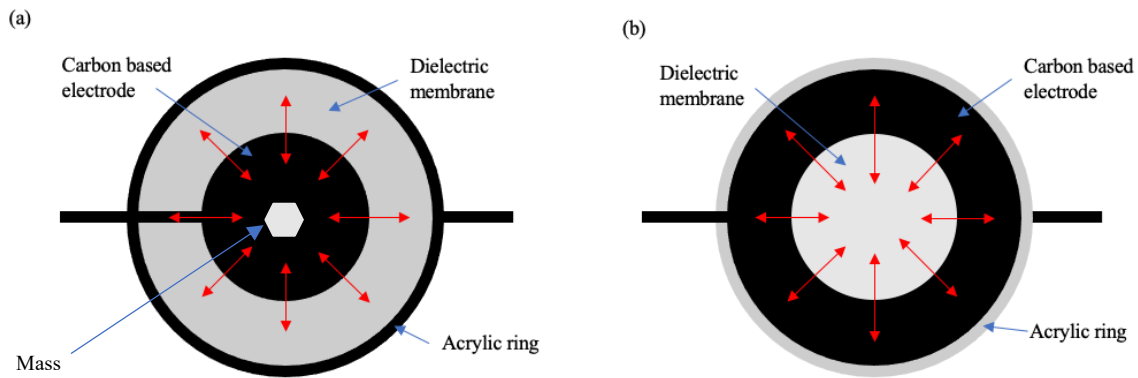


Figure 5.1: (a) Schematic of the planar spot DEA configuration tested in chapter 4. (b) Schematic of the aperture DEA configuration tested in this chapter.

To improve the actuation response of an optically controlled DEA, in this chapter we look to exploit the instabilities in the actuation of an aperture DEA, shown in figure 5.1 (b), to achieve larger actuations through surface wrinkling of the dielectric membrane. The background theory of wrinkling in DEAs and how this can benefit the proposed optically controlled DEA technology will be discussed in section 5.2. A characterisation of the transition of a DEA from stable to unstable actuation will be made to understand the voltage threshold for the onset of wrinkling for the aperture DEA that is tested. In section 5.3 we look to develop an optically controlled DEA that can transition between stable and wrinkled states due to changes in the environmental light intensity. Finally, the potential future applications of an optically controlled DEA that exhibits controlled wrinkling, such as robotic irises and active blinds are discussed in section 5.4.3.



Other methods of improving the actuation of the DEA were considered, these included increasing the applied voltage and using a high-powered UV light source as shown in table 3.3. These methods were not considered as they could become a limitation in future research. The use of a high-powered UV light source has added additional safety risks associated. Therefore, it was decided that exploiting the wrinkling stability of a DEA was the best way to improve actuation without further increasing the safety risks associated with the DEAs.

## 5.2 DEA Wrinkling

Under the application of large voltages (3-10kV) DEAs have been observed to form unstable wrinkles through the compliant electrode membrane [103]. This instability has been documented in research to allow for larger displacements to be achieved as well as snap through instabilities of the constrained DEA membrane [103]. The onset of this instability in DEA membranes can be separated into two types, Type-I is the nucleation of wrinkling at one small area of the membrane which then extends and grows throughout the membrane. The second type, Type-II, is when the entire flat membrane becomes wrinkled. These transitions can lead to out-of-plane displacements and massive displacements [104]. This displacement is usually preemptive of the electrical breakdown of the membrane and therefore a significant research has focused on looking to control the transition between stable and wrinkled actuation to allow for the exploitations of the larger displacements [105].

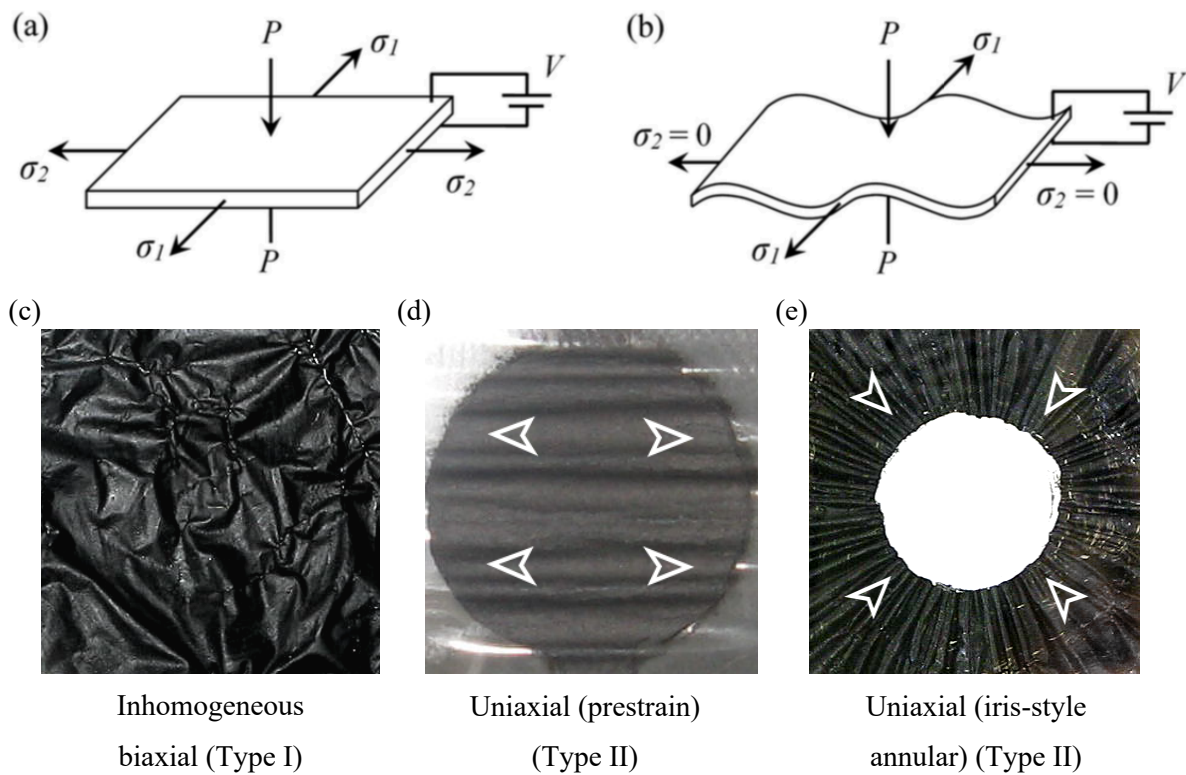


Figure 5.2: Theoretical analysis of a typical DEA membrane in (a) flat state (b) wrinkled state. (c) Shows inhomogeneous biaxial wrinkling (Type I), (d) shows uniaxial wrinkling (Type II) and (e) shows uniaxial wrinkling in an annular DEA (Type II) Reproduced from [19].

Figure 5.2 shows a diagram outlining the theory that leads to the onset of wrinkling in a DEA membrane where  $\sigma_1$  and  $\sigma_2$  are the principal in-plane stresses and  $P$  is the applied Maxwell's pressure. As the applied voltage ( $V$ ) is increased the stress in the pre-strained membrane will tend towards zero as the membrane thins due to the Maxwell's pressure. The onset of wrinkling occurs when the principal in-plane stress becomes equal to or less than zero, at which point there is a loss of tension in one direction of the membrane and the membrane starts to wrinkle as shown in figure 5.2 (b). If both in-plane principal stresses are less than 0 then biaxial wrinkling will occur. The reason why electrical breakdown often occurs as the voltage is increased further from this point is due to a runaway effect of the membrane thinning from the Maxwell pressure, leading to an increased electrical field across the membrane which in turn acts to further increase the Maxwell's pressure on the membrane, thinning it further until failure occurs.

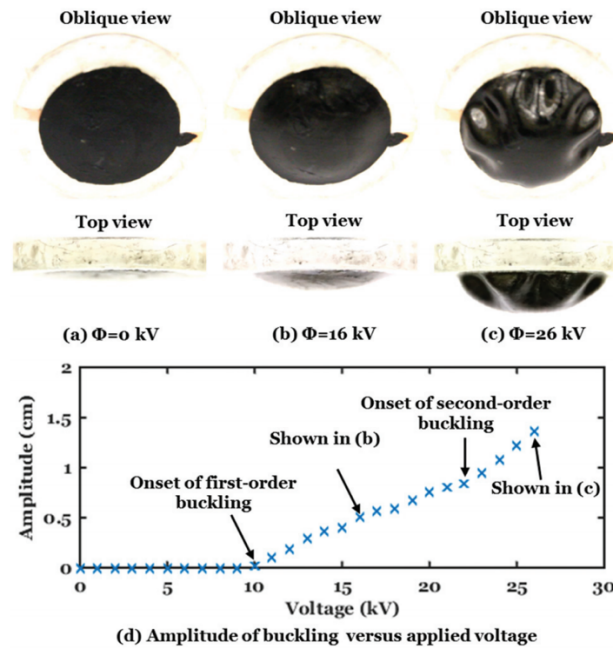


Figure 5.3: Plot of the amplitude of displacement due to buckling of the DEA as a function of the applied voltage. Reproduced from Godaba et al. [103].

Wrinkling is a form of out-of-plane buckling. Buckling is defined as the sudden change in shape of the membrane during an applied load. Figure 5.3 shows an example of the achievable displacements from exploiting the buckling of the DEA membrane. The first order buckling mode occurs at 10kV where out of plane buckling can be observed in the images of the oblique angle of the DEA in figure 5.3 (b).

The second order buckling mode occurs at significantly higher voltages, around 24kV, this shows considerable out of plane displacement from the DEA seen in figure 5.3 (c). However, the ability to demonstrate controlled and repeatable out-of-plane buckling is a significant research challenge [103][105].

With optically controlled DEAs there is an opportunity to exploit snap-through buckling instability of Type II membrane wrinkling so that the voltage swing induced by the resistance change of a-Si due to increased light pushes the DEA to the onset of wrinkling to achieve increased displacements between the ambient and illuminated conditions.

### 5.3 Wrinkling of an aperture DEA

A planar aperture DEA is a configuration that can benefit greatly from the exploitation of wrinkling instabilities [19]. Analogous to the iris of an eye, an aperture DEA is a planar DEA membrane with an annular electrode which surrounds a central passive region. On activation, the annular electrode region expands and acts to ‘close’ the central passive aperture. As shown in figure 5.2 (e), this closure occurs due to the biaxial pre-stretch of the DEA membrane. Without this, the DEA would buckle out-of-plane as seen in figure 5.3. This DEA configuration has been used to develop DEA lenses [65]. Exploiting the onset of wrinkling in an aperture DEA would lead to much larger displacements and allow for greater closure of the central aperture, opening opportunities for potential applications as automatic irises and active blinds [106].

#### 5.3.1 Methodology

Using the fabrication methodology described in chapter 4 section 4.2.7, five aperture DEAs were fabricated using VHB 4905 elastomer membranes (4x4 biaxial pre-stretch) and carbon grease (MG Chemicals) electrodes with the geometry shown in figure 5.4. The central aperture was masked using an acrylic disk laser cut to the required diameter (19mm). A high voltage amplifier, (Ultravolt 5HV A23-BP1) with a maximum output voltage of 5kV was used to drive the annular DEA.

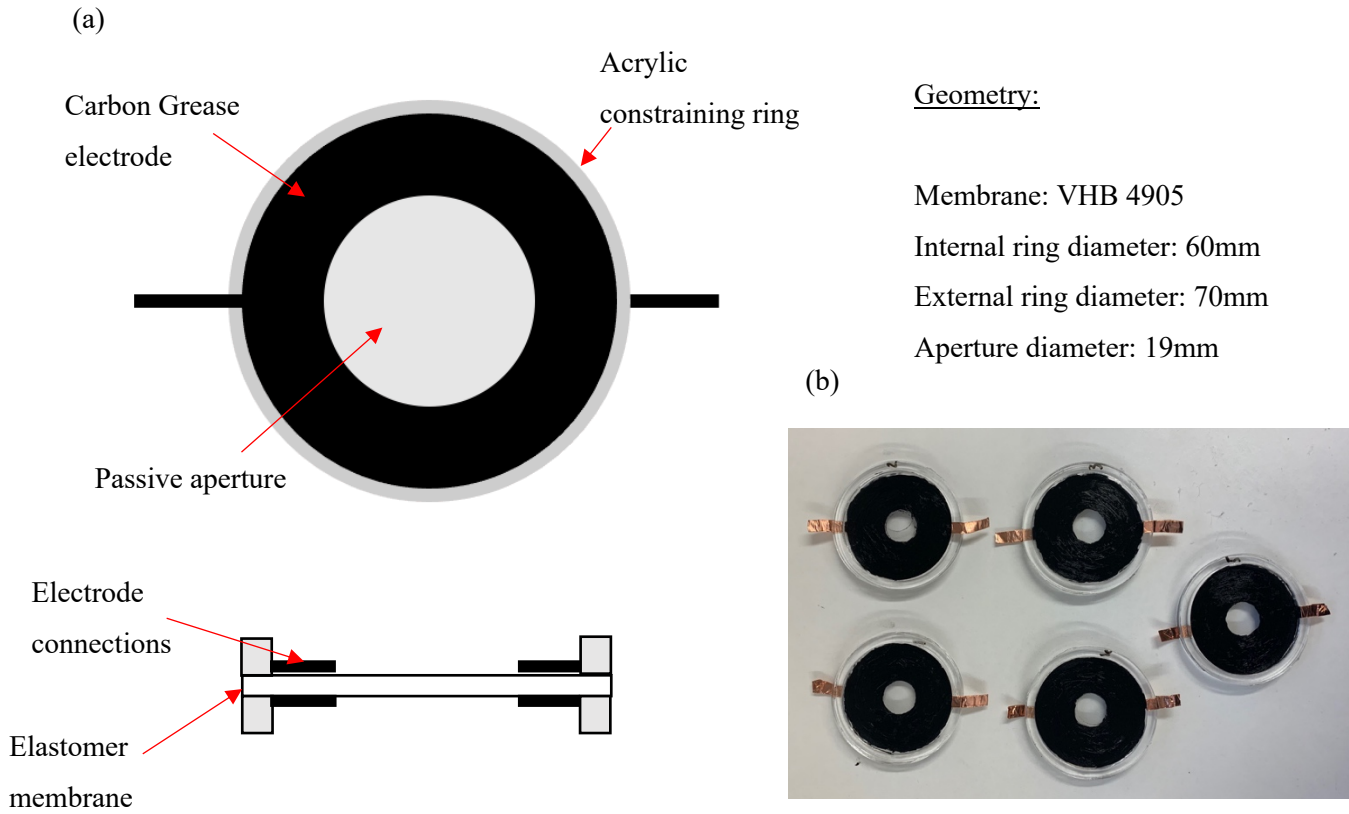


Figure 5.4: (a) Schematic of the spot aperture DEA and associated geometry. (b) Image of manufactured spot aperture DEAs.

Once fabricated, the DEAs were connected to a high voltage amplifier (Ultravolt 5HV A23-BP1) with the current and voltage signals being recorded through a DAQ (National Instruments BNC-2111). The DEAs were actuated with a square wave input at a frequency of 1Hz. This frequency was found to mitigate for viscoelastic dampening and enabled the DEA to discharge sufficiently between actuations and avoid electrical breakdown through prolonged periods of wrinkling. The DEA were tested with applied voltages of 2kV, 2.5kV and at increments of 250V between 3kV and 4.5kV.

Videos of the actuation of the DEAs were recorded at 60 frames per second to allow for image processing of the video frames. The image frames of the video for each voltage step were isolated and the size of the central aperture was measured using ImageJ image processing software. The aperture closure was measured as the percentage reduction of aperture diameter. The experimental set up for these characterization measurements is shown in figure 5.5.

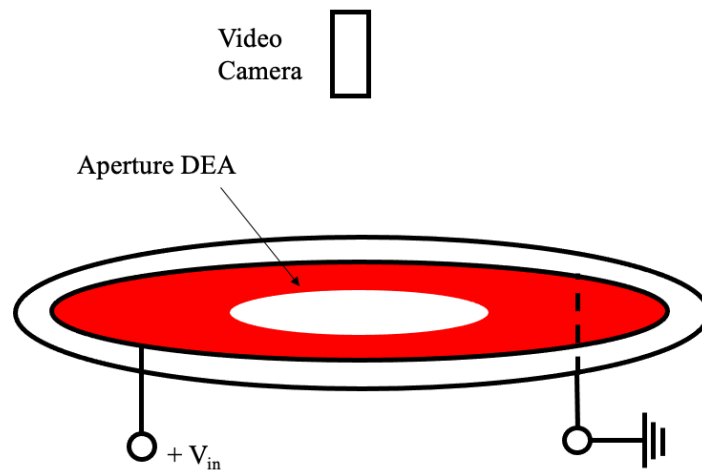


Figure 5.5: Schematic of experimental set up for the characterisation of the onset of wrinkling of an aperture DEA.

### 5.3.2 Results

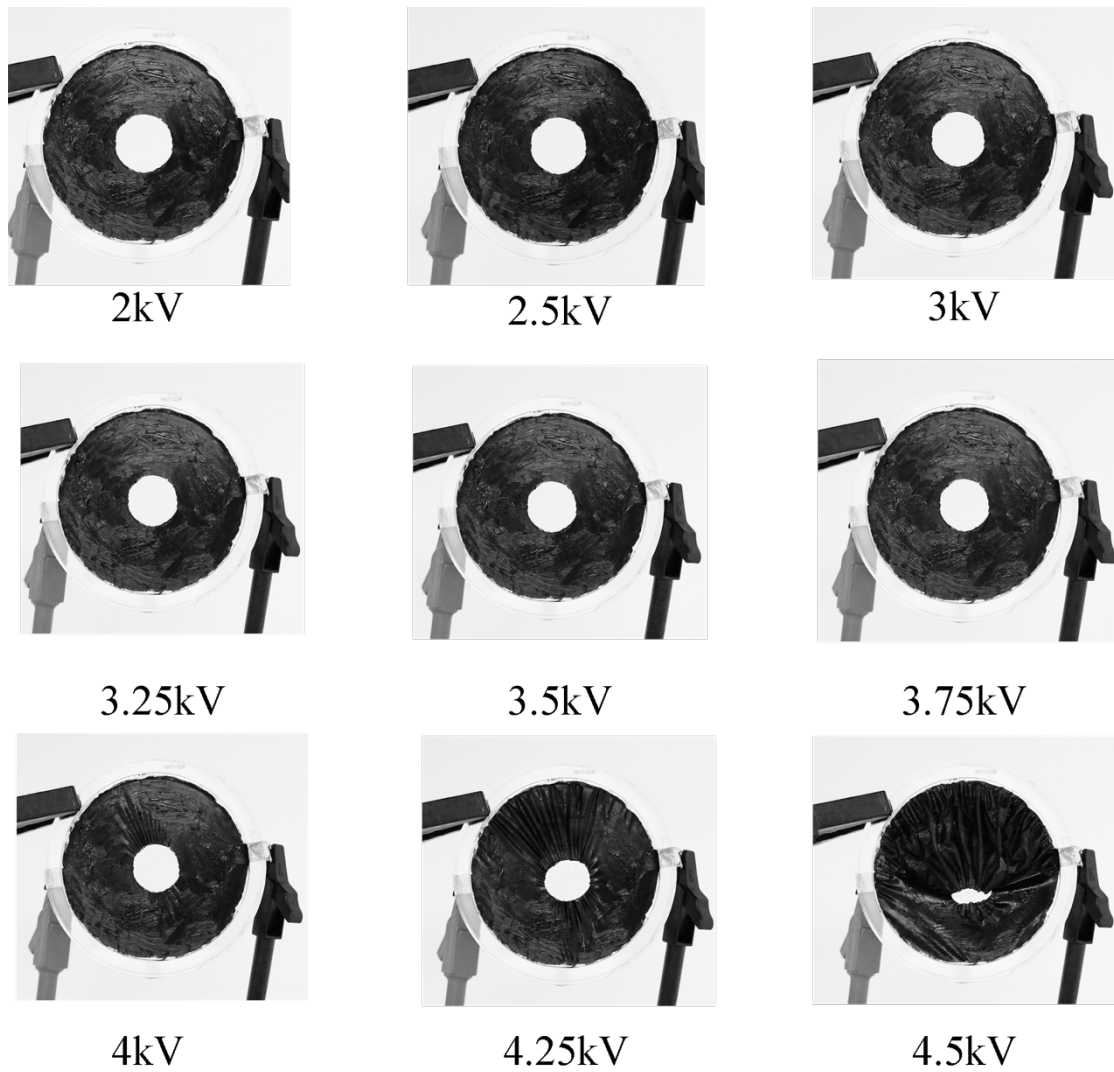


Figure 5.6: Images of the activated state of the DEA at increasing voltages.

As can be seen from figure 5.6, with increasing applied voltage the aperture of the DEA reduces in diameter. The magnitude of actuation observed is relatively small until 3.5kV where an increase in active strain is observed. The initial onset of wrinkling on the surface of the DEA membrane can be seen at 4kV where there is a small nucleation of wrinkling towards the top left quadrant of the electrode highlighted in figure 5.7 (a). At 4.25kV, significant wrinkling of the entire membrane is observed with small out of plane displacement. Finally, at 4.5kV, buckling of the DEA membrane can be observed where folding of the membrane occurs with significant out of plane displacement shown in figure 5.7 (b). At 4.5kV, the out-of-plane buckling was observed to be unstable so it can be assumed that over longer periods of applied voltages or at higher voltages the DEA would fail due to dielectric breakdown.

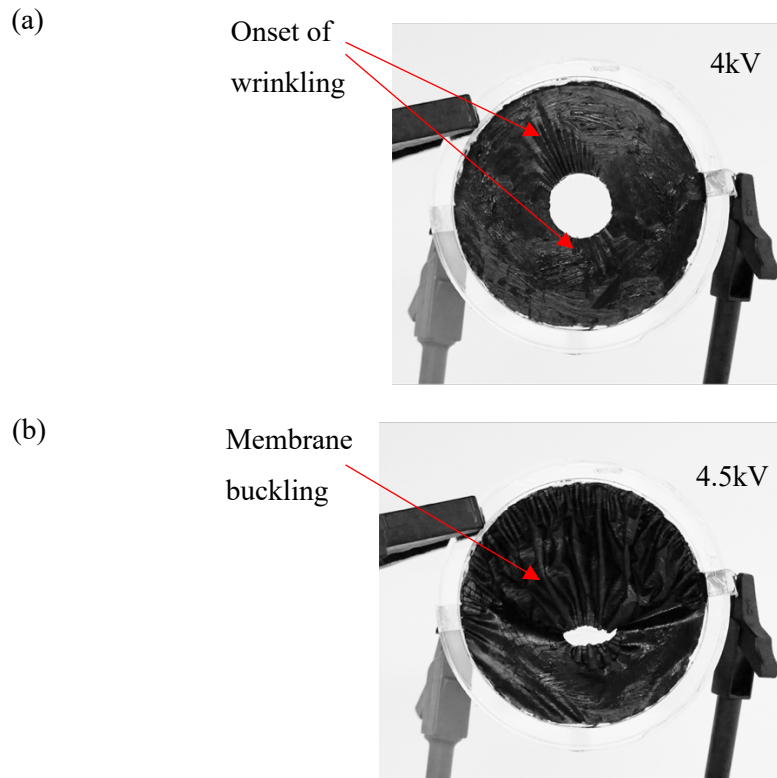


Figure 5.7: (a) Image of active aperture DEA at 4kV showing onset of wrinkling. (b) Image of active aperture DEA at 4.5kV showing unstable membrane buckling.

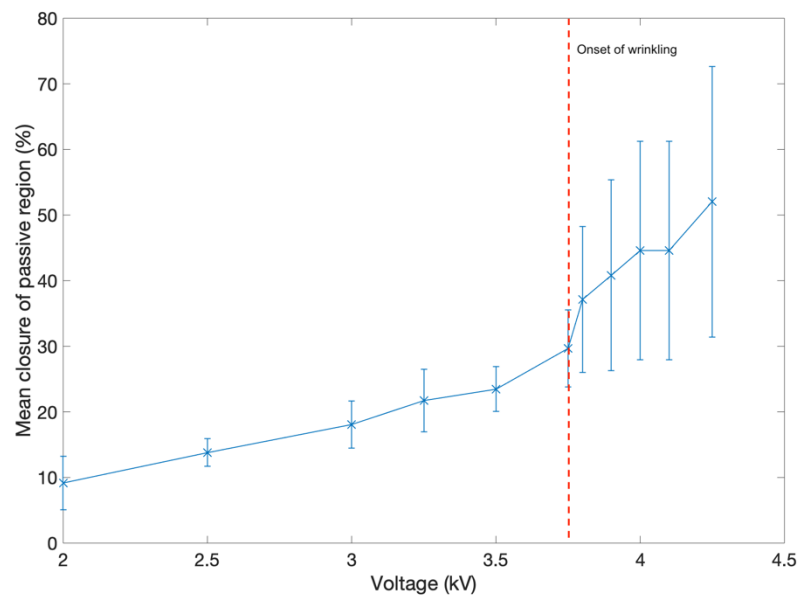


Figure 5.8: Plot of the mean closure of the passive aperture region of the DEA against applied voltage. The error bars are set to one standard deviation either side of the mean closure and are calculated from five experiments.

Figure 5.8 shows the mean aperture closure values collected from image processing of the five DEA samples with each DEA being measured once. As can be seen from figure 5.8 the mean aperture closure

percentage increases with voltage from 2kV-3.75kV with an approximately linear relationship for 10% to 27%. After 3.75kV there is a significant increase in the aperture closure percentage to 36% with a maximum closure of 52% achieved at 4.25kV. There is a much larger standard deviation across the DEAs seen between 3.75kV-4.5kV compared to 2kV-3.5kV, which indicates that the wrinkling behavior is less stable than standard in-plane active strains highlighted in figure 5.9 where there is a large variation in the type of wrinkling observed between the DEAs tested. The visual inspection of the actuation images shown in figure 5.6 confirms that the threshold for the onset of wrinkling of an aperture DEA of this geometry and pre-stretch is around 3.75kV.

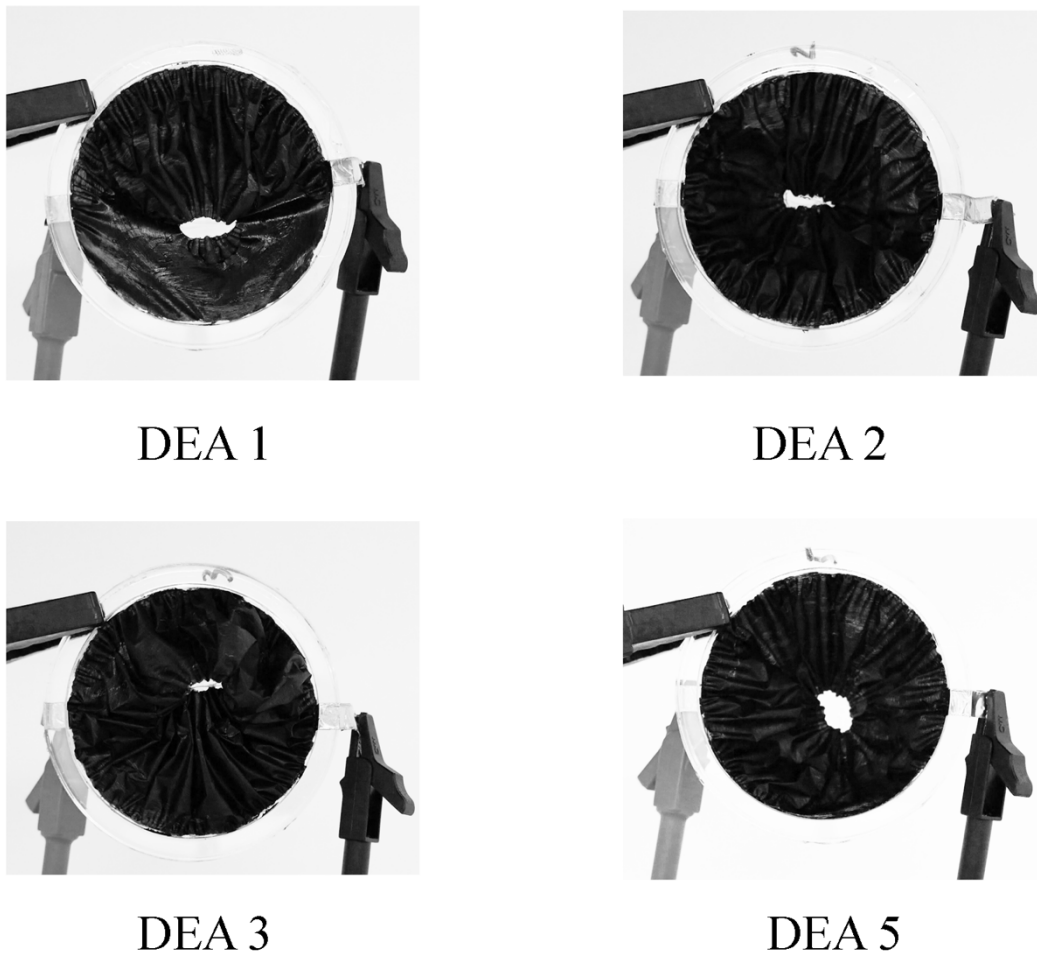


Figure 5.9: Images of the DEA samples tested at 4.5kV. DEA 4 failed before reaching the 4.5kV test.

As highlighted in section 5.2 there can be concerns surrounding the stability of the wrinkled DEA membranes during prolonged actuation. To test this, the spot aperture DEA geometry proposed in figure 5.4 was connected to the high voltage amplifier and tested at increasing voltage steps between 2.5 and 4kV at differing frequencies of input voltage signals from 0.5Hz to 4Hz (the duty cycle was kept constant at 50%). During the test the DEA was stable at all frequencies even with high amounts of



membrane wrinkling with no samples showing electrical breakdown at lower frequencies. The methodology and results for these experiments can be found in Appendix C. Electrical breakdown of the DEA is likely to occur when the period of applied voltage exceeds 5 seconds, depending on how high the applied voltage is.

### 5.3.3 Discussion

From figure 5.8 it can be proposed that for this geometry of DEA it is possible to achieve the onset of wrinkling at 3.75kV. This means that with control of the applied voltage to the DEA from the changing resistance of a-Si, it would be possible to achieve the increase in aperture closure shown in figure 5.8. As can be seen from figure 5.8, after the onset of wrinkling there is a significant increase in the standard deviation of the actuation response between the DEAs tested. This can be due to differences introduced during the DEA's fabrication such as variabilities in the electrode thickness which will lead to different amounts of wrinkling. In addition, variations in the pre-strain across the DEA membrane can lead to areas of the membrane that are more likely to nucleate the wrinkling. This could be alleviated with an automated fabrication process of the DEA actuator that would act to reduce the variance in the thickness of the electrodes due to human error during fabrication. An automated fabrication process could use alternative electrode materials to carbon grease, such as a carbon elastomer composite. An example of this could be similar to the pad printing process used by Shea et al [23]. By focusing on the initial onset of wrinkling, i.e. the 3.5-3.75kV voltage range, there will likely be a lower variance in actuation magnitude between the DEAs tested as well as a reduced risk of electrical breakdown, whilst still benefitting from the increase in actuation achieved from exploiting this instability.

We can also look to nature for comparisons: the human pupil can contract up to 50% of its original size and it can be seen from the results shown in figure 5.8 that a 52% aperture closure was achieved with an applied voltage of 4.25kV. Therefore, by utilising this wrinkling instability of the DEA membrane, it is possible to achieve an aperture closure comparable to that of biological systems and open opportunities for potential future applications.

### 5.4 Exploiting wrinkling in an optically controlled DEA

It has been demonstrated in figure 5.8 that by using a specific geometry of DEA shown in figure 5.4 it is possible to achieve a consistent voltage of for the onset wrinkling. To develop this further the inclusion of a-Si as a variable resistor in the circuit with the DEA could provide a means of switching between planar (low active strain) and wrinkled (high active strain) states. This would be achieved by applying a constant input voltage and using the variable resistance of a-Si under different light intensities to modulate the voltage across the DEA above and below the threshold voltage for wrinkling (as established in section 5.3.2).

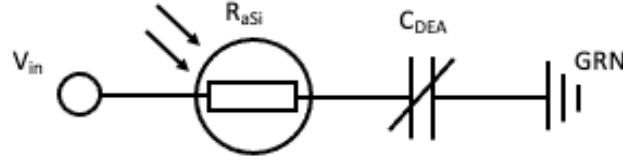


Figure 5.10: Electrical circuit diagram for the optically controlled DEA, showing the DEA in series with the a-Si sample. Where  $V_{in}$  is the input voltage,  $R_{asi}$  is the effective resistance of the a-Si and  $C_{DEA}$  is the capacitive behavior of the DEA.

The a-Si sample used in the electrical circuit shown in figure 5.10 was a  $0.84\mu\text{m}$  thick layer of a-Si deposited on a glass substrate ( $25.8\text{mm} \times 38.6\text{mm}$ ) with  $200\text{nm}$  gold electrodes deposited on to the surface. The sample of a-Si used in this investigation was the same geometry and specification as the a-Si sample used in Chapter 4. The a-Si sample was then mounted on to the same PCB with an open base to allow for the a-Si to be illuminated as shown in chapter 4 figure 4.7 (a). The a-Si was connected to the PCB using arc bonded  $5\text{nm}$  diameter gold wire as shown in chapter 4 figure 4.7 (b). The a-Si was then connected to the high voltage supply in series with the DEA which was manufactured to the specifications shown figure 5.4.

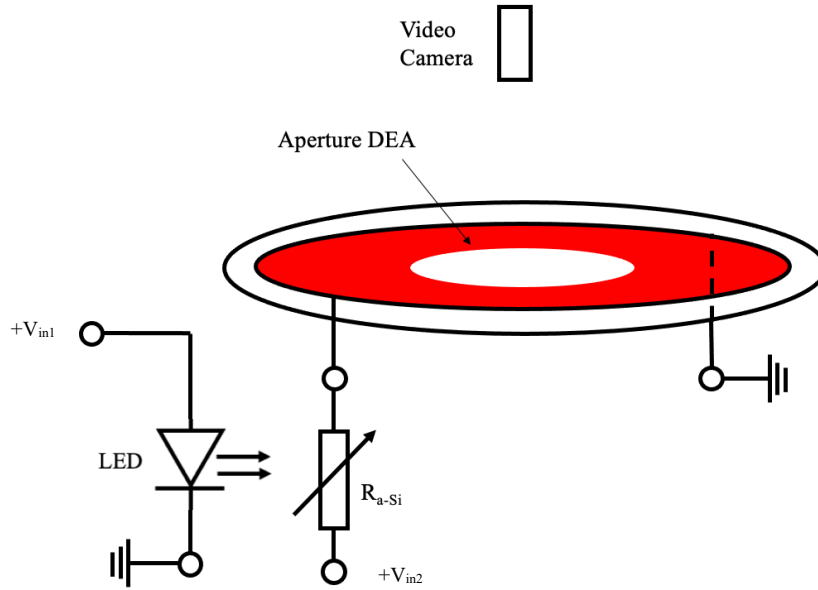


Figure 5.11: Schematic of the experimental set up for the wrinkling of an optically controlled DEA.

The a-Si was placed under a LED source with a light intensity of  $41\text{kLux}$  as shown in figure 5.11. The circuit was enclosed in a light box (an open-front box with a matte white material coating the inside to help create consistent lighting) to ensure consistent illumination and clear quality images could be obtained from the video camera. The optically controlled DEA was first tested between  $3.8\text{-}5\text{kV}$  at an ambient light condition ( $32\text{Lux}$ ) and then again with the applied LED light source. A video was taken

of the DEA during the tests and the percentage actuation was later calculated from image processing of the video frames using an image processing software (ImageJ). As can be seen in figure 5.11 there is no bleed resistor used in this electrical circuit, which was used previously in figure 4.6. It was found that the bleed resistor created a voltage divider circuit with the DEA and therefore reduced the overall voltage across the DEA. To improve the voltage across the DEA and increase actuation the bleed resistor was removed, and it was found that the a-Si had no issues with charge retention.

#### 5.4.1 Results

The percentage aperture closure for both the ambient and illuminated states were calculated using measurements of the aperture size during actuation with the image processing software ImageJ. For each voltage tested a circle was fitted to the passive aperture of the DEA during actuation. The maximum change in area of the passive region was recorded and the percentage aperture closure was calculated. Due to time constraints only a single DEA sample was tested in this preliminary study.

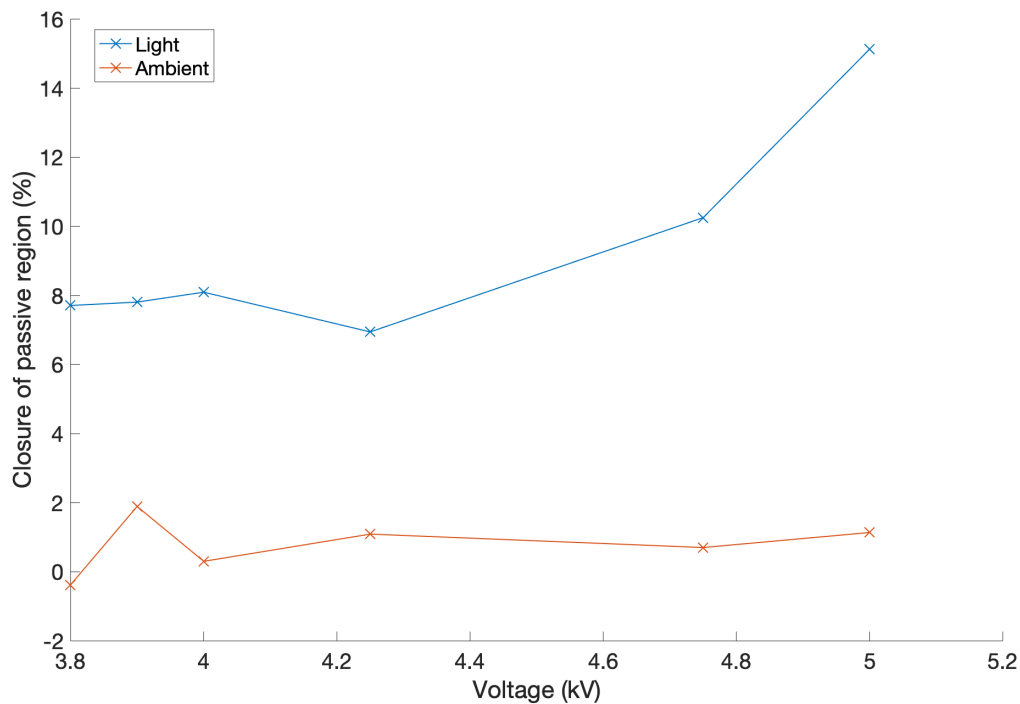


Figure 5.12: Plot showing the percentage aperture closure of the optically controlled DEA at ambient and illuminated lighting conditions.

Figure 5.12 highlights the increase in percentage closure of the iris aperture DEA between ambient and illuminated lighting conditions. It can be seen that between 3.8kV and 5kV there is a maximum of a 2% actuation increase seen in the DEA under ambient lighting conditions (32 Lux). However, by increasing the light intensity to 41kLux a significant increase in the actuation of the DEA is observed. The aperture closure increases by 7.9% at 3.8kV to a maximum of 15.2% at 5kV. It was noted that no signs of

wrinkling of the DEA membrane were observed during the investigation even at 5kV which is the limit of the high voltage amplifier used (Ultravolt 5HV A23-BP1). As the voltage is increased from 4.2kV to 5kV under the illuminated lighting condition a significant increase in the actuation response is seen compared to the region of 3.8kV to 4.2kV.

#### 5.4.2 Discussion

This investigation demonstrates that a greater actuation stroke can be achieved by designing the geometry of the DEA to help induce the onset of wrinkling through the change in resistance of a-Si between ambient and illuminated states. As shown in figure 5.12 a maximum of 15.2% aperture closure can be achieved through changes in light intensity at 5kV, although this was achieved without wrinkling. This demonstrates a method of actuating a DEA by changing the environmental light intensity. This method also uses a simplified electrical circuit shown in figure 5.10 compared to the optically controlled DEA in chapter 4 figure 4.8 that has the potential to be easily integrated into a stand-alone actuator device in future work due to the thin layer of a-Si required (0.84 $\mu$ m).

Despite the high input voltages (up to 5kV) applied to the optically controlled DEA there was no signs of membrane wrinkling during actuation. When compared to the input voltages required to wrinkle the DEA without a-Si (3.75kV) we would expect to show some signs of instability in the actuation of the optically controlled DEA in the applied voltage range of 3.8kV to 5kV. However, due to the resistance of the a-Si in series with the DEA, the a-Si and the DEA act as a potential divider and the voltage across the DEA is lower than the input voltage, even at a higher light intensity. Therefore, in order to exploit the large actuation increase seen in figure 5.8 it will be necessary to apply a higher input voltage (>5kV), which would be above the voltage limit of the high voltage amplifiers used in this investigation (5kV).

Due to the recent restrictions on lab access at the time of this research due to the Covid-19 outbreak the use of a higher limit amplifier was not possible. However, using extrapolation from the results collected, the approximate input voltage required to achieve the onset of wrinkling from the application of higher light intensity to the optically controlled DEA can be predicted. Considering the results in figure 5.12, an aperture closure of 15.2% was achieved at 5kV for the optically controlled DEA. Using the results from the high voltage test on the spot actuated DEA in figure 5.8, an aperture closure of 15.2% is equivalent to an applied voltage across the DEA of 2.75kV. Therefore, if the onset of wrinkling for this DEA geometry occurs at an applied voltage across the DEA of 3.75kV it can be predicted using the estimate resistance values of a-Si as a function of light intensity presented in chapter 4, that the onset of wrinkling for the optically controlled DEA should occur around an input voltage of 6kV.

### 5.4.3 Potential applications

The ability to utilise the changes in light intensity of the environment to control the actuation of a robotic device has a number of potential applications. These include optical blinds, where the increase in light intensity through a window could allow for the instantaneous activation of the DEA blinds that would effectively open and close in response to the environment.

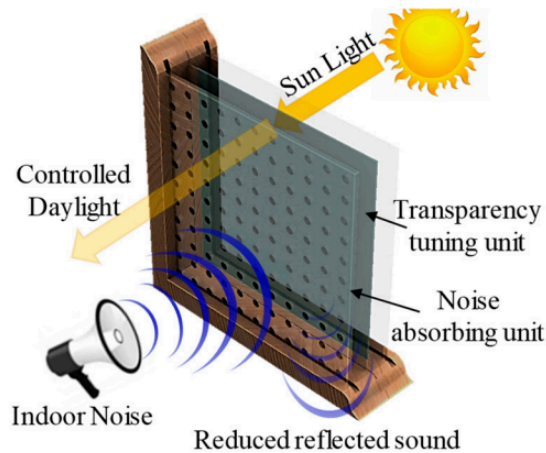


Figure 5.13: Example of DEA based tunable window that has both transparency and noise control. Reproduced from Shrestha et al. [106].

There have also been examples of conventionally controlled DEAs being used to vary the opacity of tunable windows. Figure 5.13 shows an example of the design of DEA actuator that could most benefit from the optically controlled DEA technology developed in this chapter. The design in figure 5.13 operates by using an array of DEAs to alter the texture of the window through actuation. This change in surface roughness due to the actuation of the DEA leads to the transition between a transparent and opaque finish to the window. By using a-Si in an optically controlled DEA it would be possible to passively control this transition between transparent and opaque in real time and allow for autonomous control of the window without the need for a microcontroller. However, the energy efficiency of the proposed optically controlled DEA is a limitation as the supply voltage is always on and the DEA may exhibit a small leakage current.

Another example of potential applications of the optically controlled DEA that could be explored in future work is using the DEA iris within a robotic eye for applications in animatronics. The human iris can contract up to 50% of its original aperture size. The results shown in figure 5.8 show that this amount of contraction can potentially be achievable by exploiting wrinkling instabilities from a spot an iris DEA (52% aperture closure).

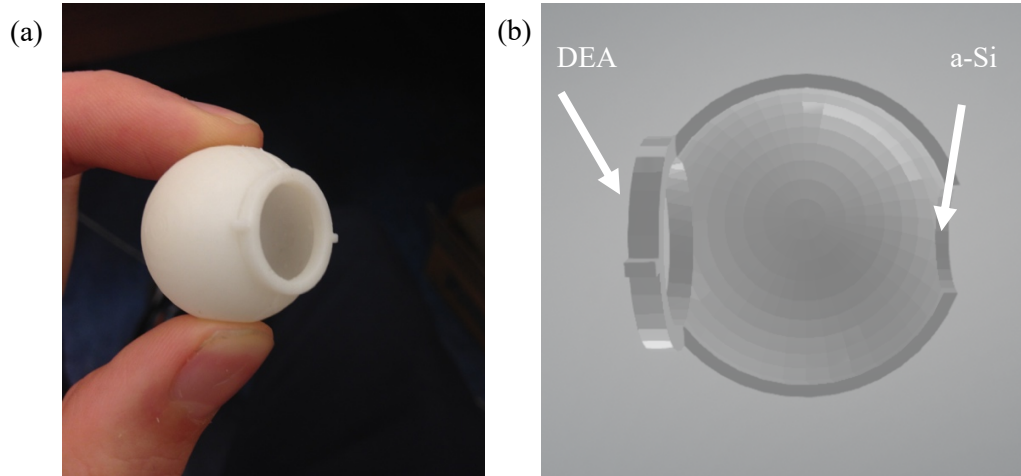


Figure 5.14: (a) 3D printed model of an animatronic DEA eye design. (b) Example of the proposed optically controlled DEA eye design using an a-Si ‘retina’.

Figure 5.14 above shows a proposed design for a robotic animatronic eye with a DEA iris. The VHB DEA membrane is pre strained over the front circular mount labeled in figure 5.14 (b) for the iris and can be held in place with a retaining ring. The a-Si deposited on a glass substrate is placed at the back of the DEA eye as a ‘pseudo-retina’. Once enclosed, light will enter the eye through the transparent region of the passive aperture in the centre of the DEA membrane. This would allow light to reach the a-Si at the back of the eye and cause a reduction in the resistance sufficient to allow the iris to actuate in response to changes in the environmental light intensity.

### 5.5 Conclusions

In this chapter we have established a method of increasing the actuation response of an optically controlled DEA aperture by designing the geometry of the DEA to exploit wrinkling instabilities. The geometry of the DEA was demonstrated to induce an onset of wrinkling instabilities at an applied voltage of 3.75kV. The wrinkling enabled a snape-through increase in actuation strain was leading to a maximum measured aperture closure of 52%. This aperture closure is of a similar scale of actuation seen in biological examples such as the human eye.

After establishing the geometry of the DEA and characterising the voltage range required to trigger the onset of wrinkling, the DEA was then placed in series with an a-Si sample. During testing of the optically controlled DEA there were no signs of wrinkling instabilities at the voltage range tested (3.8-5kV), which was due to the series arrangement of the a-Si and DEA acting as a potential divider circuit and the saturated output of the available high voltage amplifier. However, this investigation did demonstrate that a 15.2% increase in aperture closure can be observed between an ambient lighting condition (32Lux) and an illuminated environment (41kLux) with an applied voltage of 5kV. This is a significant result in developing novel methods of passive control of electrostatic actuators. In this work it was demonstrated that observable levels of actuation can be achieved through changes in the environmental light intensity of the DEA actuator. This could lead to exciting future applications such as tunable windows and an animatronic eye proposed in section 5.4.3.

Although wrinkling instabilities were not observed at the voltages tested for the optical controlled DEA with the a-Si switch, it was predicted that wrinkling would be triggered with a light intensity of 41kLux and an input voltage of 6kV. This is an area of future work to be explored in which the change in environmental light intensity can be used to stimulate the transition between stable and wrinkling of the DEA, leading to dramatic actuation responses.

Having demonstrated the use of a-Si to control a DEA, in the next chapter we will look to develop a means of integrating a-Si into the body of an alternative electrostatic actuator to achieve a higher overall structural compliance.

## Chapter 6 a-Si Kapton actuator

*This work was published [107] in SPIE EAPAD conference proceedings 2020: C. Gillespie, A.Marzo, F. Scarpa, J. M. Rossiter, and A. T. Conn, “Switching of amorphous silicon thin-film actuators for optically functional robotic devices,” in Electroactive Polymer Actuators and Devices (EAPAD) XXII, 2020, p. 52.*

### 6.1 Introduction

In this chapter we look to develop a method of integrating amorphous silicon (a-Si) into the body of a compliant electrostatic zipping actuator. In previous chapters a-Si has been manufactured, characterised and tested as a stand-alone device to be used with a type of electrostatic actuator, dielectric elastomer actuators (DEA). In this chapter a flexible a-Si film is developed using thin film deposition onto a flexible polyimide (Kapton) substrate with a high glass transition temperature. From this, a novel electrostatic cantilever actuator is presented that can be actuated by changes in light intensity.

Developing thin film functional materials offers potential benefits to the control of compliant actuator designs (as highlighted in chapter 2) with the increased drive for integration of control into the body of soft robots [4][67]. Typically, to control multiple actuators, electrical components such as relays and transistors are used to turn individual actuators on and off. The electrical components used for relay circuits are largely not flexible and therefore limit the overall compliance of the device, which is a large hurdle to overcome when developing highly compliant and untethered robotic devices. By using the thin film deposition presented in this chapter, it is shown that it is possible to benefit from the photo resistive properties of a-Si, which have been previously demonstrated as a potential method of control (chapter 4 section 4.4), whilst maintaining a high degree of compliance from the material due to the small thickness deposited (of the order of nanometers). This can lead to applications including photo responsive compliant structures such as self-deploying solar panels for space applications.

#### 6.1.1 Compliant electrostatic actuators

State of the art electrostatic zipping actuators include the HASEL (hydraulically amplified self-healing electrostatic actuator) design [17][32], which consists of a sealed inert pouch of dielectric fluid with two electrodes on either side of the pouch (figure 6.1).



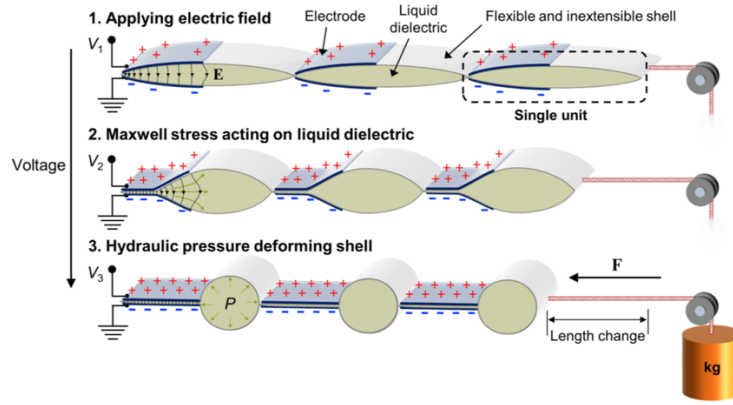


Figure 6.1: Schematic showing the structure and operation of a HASEL actuator. Reproduced from [17].

The dielectric fluid is used due to its high dielectric constant and electrical breakdown strength. This leads to the fluid being forced to one end of the pouch where a strain is produced through mechanical amplification from the fluid being translated.

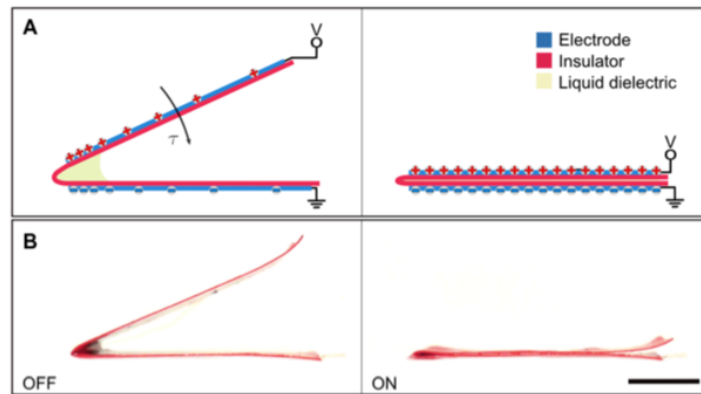


Figure 6.2: (a) schematic of the DLZ actuator relaxed and under applied voltage. (b) images of the DLZ actuator relaxed and under applied voltage. Reproduced from [16].

Another example is the DLZ (dielectric liquid zipping) actuator [16] which consists of two electrodes separated by an insulating material (typically PVC) as seen in figure 6.2. The two electrodes are joined together at each end to create a bow like structure. Silicone oil is placed in the corners of these joints to help amplify the closing force as the electrodes zip together via dielectrophoretic forces. Both the HASEL and the DLZ actuator designs demonstrate high mass and volume specific actuation outputs similar to that of mammalian skeletal muscle.

### 6.1.2 Photonic control of compliant actuators.

The mechanism of photonic activation for actuators is an attractive means of generating wireless control of electrostatic actuators. This is due to the ready availability of light sources, which can either be from

changes in the environment or external sources such as an LED. Using light as a means of control for actuator devices does not suffer from the same field dependent scaling losses that can occur in other means of transduction such as electro-magnetic coupling [44][108]. Examples of optically functional soft robotic devices in literature include exploiting morphological changes in liquid crystalline polymers to achieve actuation in thin films in work by Pliz De Cunha et al [2]. Multi-directional untethered locomotion of the device was achieved by using azobenzene chromatophores on a liquid crystal polymer film which actuate when a specific wavelength of light is applied. One downside of this is the requirement of a specific wavelength of light which therefore requires a specific source. This limits the potential application of this method of photo-induced actuation as it is unable to be actuated by changes in the natural environment where the specificity of the wavelength is hard to control. One advantage, however of using specific wavelengths is demonstrated by Wang et al [69] which used liquid crystal elastomer nano composites with applied silicon p-n junctions to create a photo-actuated bi-morph [69]. The use of silicon photo receptors across the actuator body allowed the controlled actuation of different regions of the bimorph through the wavelength of light applied. This allowed for control of multiple degrees of freedom demonstrated in an inchworm-like locomotion [69]. Instead, control using light intensity rather than wavelength could be seen as a better method when looking to develop passive environmental responses from the actuator.

In this chapter a photo-induced compliant zipping actuator which triggers actuation through changes in light intensity is explored. This will allow the device to respond to applied photonic stimulus by the application of external light sources (LED) as well as changes in the ambient environment, allowing for methods of passive control. As highlighted in the literature there are also opportunities to use specific wavelengths to control certain photo-induced actuators in a linked system. This would be an area of potential future research once a method of photo-induced actuation has been demonstrated. In this chapter the manufacturing process for a-Si thin films as well as the manufacture of the a-Si zipping cantilever is outlined.

## 6.2 Manufacturing of a-Si thin films

One of the major obstacles in developing a compliant film of a-Si is selecting an appropriate substrate. The plasma enhanced chemical vapor deposition (PECVD) process used to deposit a-Si has an operational chamber temperature of 250°C (see section 3.3 for further details of the PECVD process). This limits the range of materials available to be used as most flexible substrates, such as polymer films, do not have a high enough glass transition temperature ( $T_g$ ) to withstand the deposition process. For this investigation, a poly-imide film (DuPont Kapton) was used as the substrate for depositing the a-Si. Kapton was selected due to its high glass transition temperature (360°C) making it ideal for this processing technique. Kapton is a material that is widely used in the electronics industry due to its desired thermal properties and high dielectric break down strength.

In this investigation, 25 $\mu$ m thick Kapton film was cut to a 5cm by 5cm square. The surface of the film was cleaned with pressurised nitrogen gas to remove any surface impurities and was placed onto a silicon carrier wafer using small sections of silicon wafer to hold the Kapton film in place. The PECVD process was run for a deposition time of 5 minutes which is equivalent to an approximate a-Si layer thickness of 140nm. This layer thickness was chosen after initial tests to reduce the chance of the a-Si film being too stiff and brittle to be used in a compliant design whilst still maintaining the desired photo absorption in line with the results presented in chapter 3 section 3.9.3.

### 6.2.1 Processing difficulties

In this section we look at the difficulties that arose during the manufacturing process of a-Si/Kapton thin films and how these issues can be alleviated.

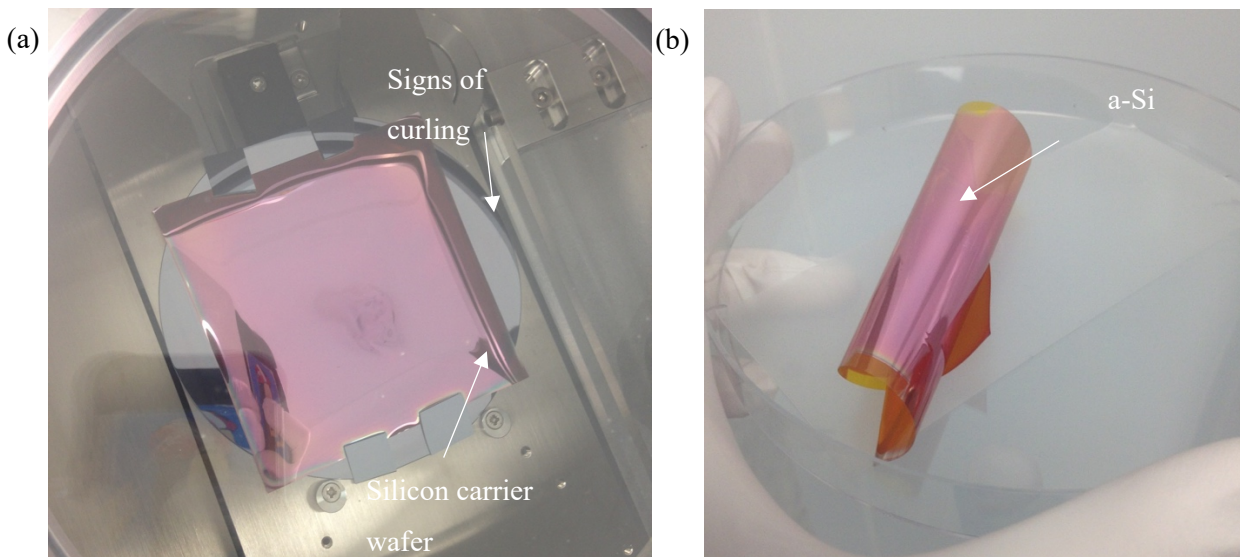


Figure 6.3: (a) Image showing the a-Si/Kapton thin film in the loading chamber of the PECVD system after deposition of 140nm of a-Si. (b) Image showing the significant curling of a-Si/Kapton film after it has been removed from the PECVD system.

Figure 6.3 (a) shows a sample of the a-Si/Kapton film in the loading chamber. The overall layer deposition looks to be consistent with minor effects seen around the edges of the film and the silicon wafer mounts used to hold the film in place during deposition. It can also be observed that there is a slight buckling to the surface layer as it no longer lays flat on the carrier wafer. This surface curvature became more extreme after the loading chamber was vented.

The a-Si/Kapton thin film was then removed from the PECVD system and it was immediately obvious that there was significant curling of the film as seen in figure 6.3 (b). There are two potential explanations for the curving of the a-Si thin film. The first is a potential mismatch in the thermal

expansion coefficients between the Kapton substrate and the a-Si deposited layer. The elevated operational temperatures of the PECVD machine would lead to thermal expansion of the Kapton substrate during deposition. During cooling the difference between the thermal expansion coefficient of Kapton and a-Si will lead to a mismatch in the amount of contraction between the a-Si and the substrate. This would lead to a stress on the surface of the thin film and cause the material to curve. This could be reduced by using a lower temperature CVD process however highly specialist industrial equipment is required to do this. The second potential reason is uneven thickness of the deposited a-Si layer. In the PECVD system the inlet of the reactants comes from a single source above the electrode. Due to the short deposition time, there is likely to be more a-Si deposited in the centre of the film than at the edges. This can be seen in figure 6.3 where a slight colour change can be observed around the edges of the deposited film, which indicates a variation in layer thickness by the colour of the refracted light between the layers. Since the issues with Kapton/a-Si processing was likely caused by the method of manufacturing (elevated deposition temperatures) and with limited alternative substrate flexible substrate materials, it was decided that samples for testing should be taken from the central area (3 cm in from the samples edges) of the 5 x 5 cm deposited film. This was intended to avoid the impact of any thickness variation to reduce excessive curving of the test samples. Despite this, some residual curvature will remain in the film. Residual curvature in the a-Si/Kapton film has the potential for use in an electrostatic zipping actuator since the inherent curvature of the film can provide an initial open position for the zipper. This concept is investigated here.

### 6.3 A-Si cantilever

Combining the photo reactive response of the a-Si with the curvature of the deposited thin films were developed into an a-Si zipping actuator which consisted of an a-Si electrode and a fixed electrode (figure 6.5). During actuation, the positive a-Si electrode will zip closed along the negatively charged fixed electrode. An approximate representation of a zipping actuator was proposed in chapter 2, where the actuator can be considered to be a number of intestinal point sources separated by a distance  $r$  as shown in figure 6.4.

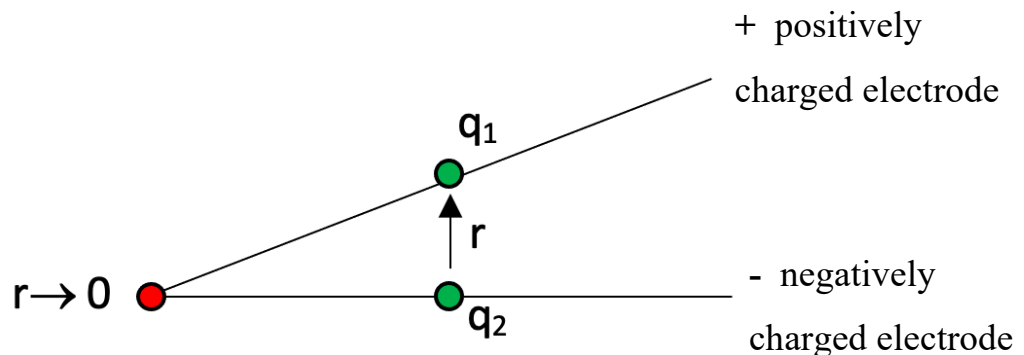


Figure 6.4: Diagram showing a simplified point charge model for an electrostatic zipper.

As can be seen from figure 6.4, the point charges  $q_1$  and  $q_2$  have an increased separation distance,  $r$ , at positions moving away from the initial zipping point of the cantilever. Therefore, it can be inferred that the electrostatic closing force will increase as the separation distance  $r$  tends towards zero. During actuation the zipping point will move along the length of the actuator as the electrodes become closer together. The equation below (Coulomb's law) describes the relationship between the closing force  $F$ , between two point charges  $q_1$  and  $q_2$  at a separation distance  $r$  where  $K$  is Coulomb's constant ( $K = 8.988 \times 10^9 \text{ Nm}^2/\text{C}^2$ ).

$$F = K \frac{q_1 q_2}{r^2} \quad (1)$$

As shown by equation (1) the closing force tends to infinity as the distance  $r$  tends towards zero at the zipping point. This numerical model does not consider interaction between neighboring point sources along the length of the actuator and will only give an approximation of the closing force. The model also does not take into account any insulating materials between the electrodes, which will affect the minimum zipping distance. Future work could investigate a more accurate representation of the electrostatic field and force output of this actuator using numerical computer modeling of the actuator such as COMSOL Multiphysics software. In this type of modeling both the electrical properties of the a-Si/Kapton thin film and its mechanical properties can be coupled together and applied to a 2D representative model of the actuator.

#### 6.4 Manufacturing of a-Si cantilever actuator

The a-Si zipping actuator consisted of a positive electrode (3 x 8mm) made of 0.14 $\mu\text{m}$  of a-Si deposited on 25 $\mu\text{m}$  thick Kapton film and a negative electrode made from steel shim (40 x 12 x 0.07mm) which was coated in poly-vinyl chloride tape (40mm x 12mm x 130 $\mu\text{m}$ ), to avoid electrical shorting between the two electrodes during actuation.

The actuator was built in a step-by-step assembly process. Initially, a section of PVC tape was placed with the adhesive side up. On to this the steel shim negative electrode was placed and electrically connected with a small copper tape contact protruding out beyond the PVC insulation. A second layer of PVC tape was placed over the steel shim and pressure was applied to the surface to ensure the electrode was sealed. The a-Si/Kapton positive electrode was then cut to size (3 x 8mm) using a scalpel. The a-Si electrode was taken from the centre of the deposited film (at least 3cm from each edge of the 5cm film) to ensure consistency in the a-Si layer thickness along the length of the actuator. The base of the a-Si electrode was electrically connected with copper tape contact and then secured in place using PVC tape. This helped to keep the positive electrode in place as well as maintain a consistent close distance between the two electrodes at the zipping point.

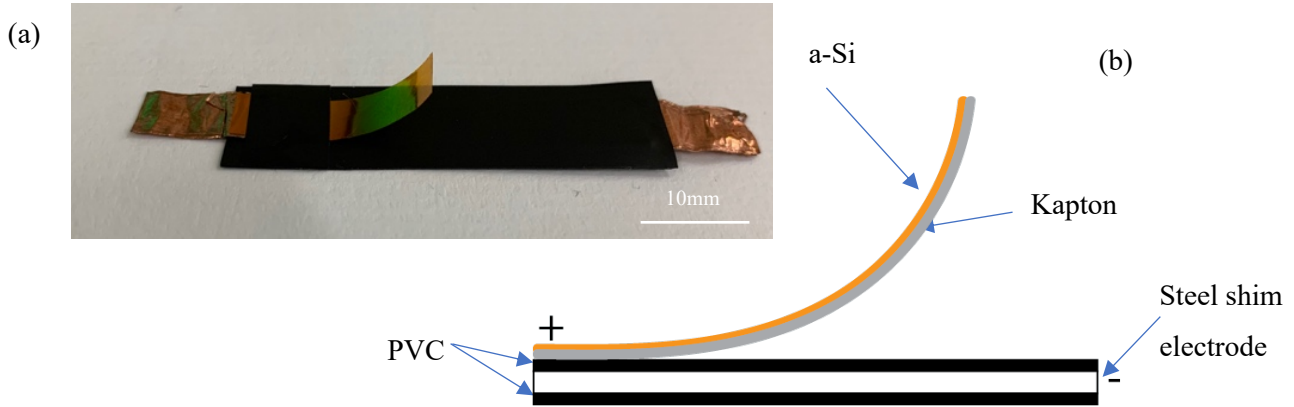


Figure 6.5: (a) Image of the a-Si/Kapton zipping actuator. (b) Schematic of the component parts of the a-Si/Kapton zipping actuator.

Due to the changes in resistance of a-Si with varying light intensity it is possible to generate a sufficiently large change in the electrostatic force between the two electrodes under constant applied voltage to allow the actuator to zip with air as the medium between them. Therefore, there is no need for the high dielectric liquids such as silicone oil used in current zipping actuator designs such as the DLZ [16] and Peano-HASEL [17].

### 6.5 Image processing

Due to the relatively small size of the a-Si cantilever and its structural compliance, the use of embedded sensors to record the output of the actuator would directly impact the performance of the device, therefore remote video imaging was used as a means to track the actuation. An image processing algorithm was applied to measure the change in curvature of the a-Si/Kapton positive electrode during actuation. To maintain consistency between each test the a-Si cantilever was attached to an acrylic support and clamped in place in order to maintain the same relative position between the camera and the actuator between tests. To ensure consistency in the background of the image and to maintain an even illumination, a light box was used to provide a consistent white background.

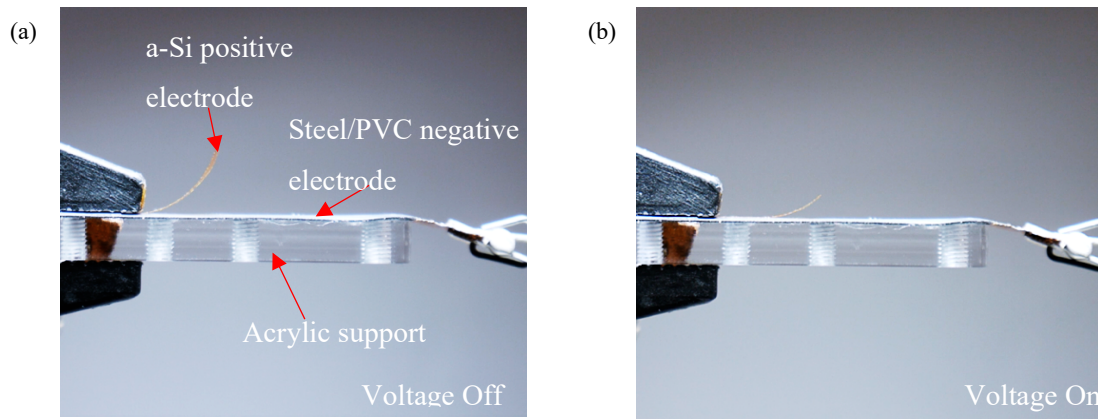


Figure 6.6: (a) Image showing the experimental set up for the a-Si cantilever at 36kLux. (b) Image showing the a-Si cantilever during actuation at 36kLux. (reproduced from [107])

The experimental set up for measuring the change in curvature of the a-Si cantilever between ambient and illuminated lighting environments is shown in figure 6.6. Figure 6.6 shows a frame of the video taken of the a-Si cantilever before actuation in figure 5 (a) and during actuation in figure 6.6 (b). Actuation occurred in the illuminated state which had a light intensity of approximately 36kLux, seen in figure 6.6 (b). The ambient light intensity was measured to be 22Lux.

The image processing algorithm developed for this investigation aimed to isolate the positive a-Si/Kapton electrode and measure its curvature change over time. In order to do this, there were a number of image processing steps that had to be applied to each frame of the video in order to accurately capture this change. The video (1080p resolution) was taken at 60 frames per second and was sampled at a rate of 10 frames per second in the algorithm. As can be seen in figure 6.6 the whole frame of the image taken contains a number of artifacts that are not the subject of interest being measured (a-Si electrode), including the acrylic support and the clamp stand. The videos were edited before being passed through the algorithm to crop the region of interest to just include the actuator and to trim the videos. To synchronise the time of each video, a small LED was placed on the clamp and connected to the DAQ during the experiment to provide a visual signal for when the voltage was applied to the actuator. The LED was positioned so that it would not impact the actuator during the tests.

Once the video footage had been cropped and synchronised the frames were processed to isolate the actuator from the background. This was done with a thresholding technique, which looks to change the pixels of the image by converting it into a binary image. It was found that for the ambient tests the best threshold to use was a black and white threshold function whereas in the illuminated case a thresholding function which worked based on the HGV channels of the image where used. Other thresholding techniques such as using the Euclidean distance of the RGB pixel values from a section of the backdrop were tested but did not provide consistent results between tests due to small lighting variations in the



background due to the time of day. The evaluation for choosing the threshold value was to reduce the number of artifacts in each frame and ensure a consistent image of the positive a-Si/Kapton electrode. Once the threshold was applied, a fill function with a spherical shape was used to fill the ‘holes’ in the cantilever image. Holes were defined as areas of zero value pixels that are surrounded by a certain radius of filled pixels, which helped to ensure a consistent image of the electrodes as it moves during actuation.

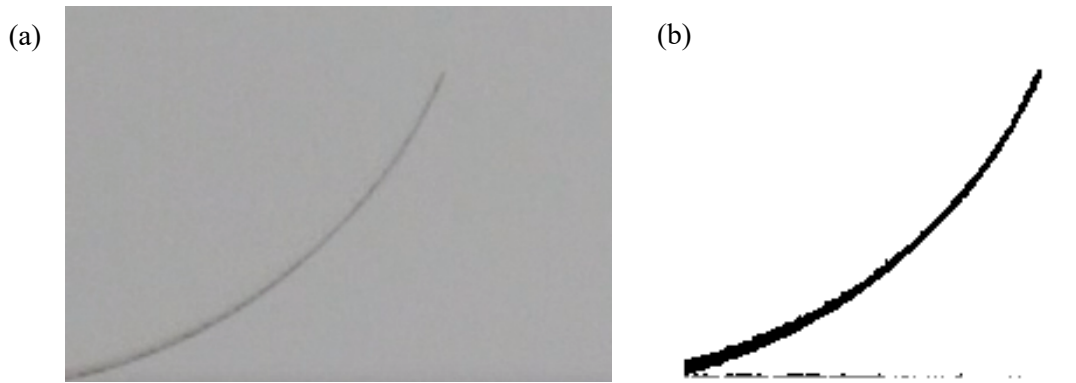


Figure 6.7: (a) Cropped image of the a-Si/Kapton electrode under ambient light conditions. (b) image of the a-Si/Kapton electrode under ambient light conditions after applying the threshold.

Figure 6.7 above shows an example of a frame from an ambient lighting test and the same image frame after thresholding has been applied. As can be seen from figure 6.7, the thresholding clearly separates the point of interest, the a-Si/Kapton electrode, from the image background and there is little to no erroneous pixels in the main area of the background. At the bottom of figure 6.7 (b) a small area of the negative electrode can be seen in the image; this is difficult to avoid but can be alleviated by selective processing of the image data.

After thresholding, a binary image is generated where pixels with values 1 correspond to the black pixels of the actuator shown in figure 6.7 (b). To find the edge of the actuator a simple For loop was written which checks the value of each pixel in a column of the image array until it finds a pixel of value 1, denoting the edge of the actuator. The algorithm then records the x and y coordinates of the pixel and then the loop moves on to the next column in the image array until all of the image is processed. This gives a list of (x,y) coordinates of the top edge of the a-Si electrode for each frame of the video, which can be used to track the actuator during testing.

Once the coordinates of the a-Si/Kapton electrode were recorded, a circle fitting function was used to fit a circle to the curve of the electrode. With this fit a measurement of the curvature of the electrode can be made as well as the root mean squared error of the fitted circle.



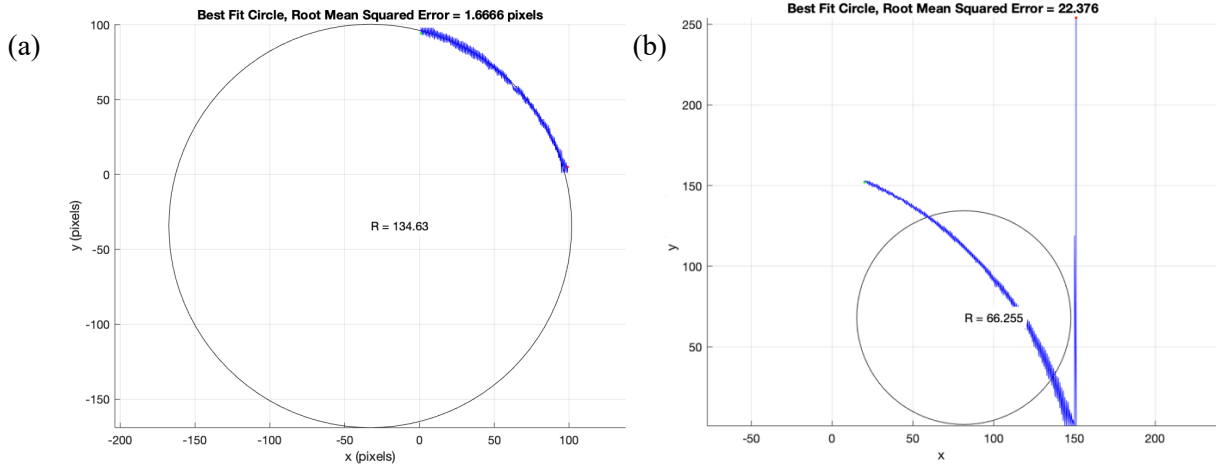


Figure 6.8: (a) Example of the circle fitting function output for a frame of the actuation. (b) Example of a poor fitting of the circle fitting function due to incorrect cropping of the negative electrode.

Figure 6.8 shows two example outputs from the circle fitting function used in this algorithm. Figure 6.8 (a) shows an example of a frame of the actuation video with a good fit and low root mean squared (RMS) error. Figure 6.8 (b) shows an example of the potential difficulties caused by ineffective image cropping. In this frame a small section of the negative electrode has entered the cropped area of the video and is causing the circle fitting function to be ‘skewed’ off the positive electrode being measured. This leads to both a poor fit and an erroneous curvature value for this frame of the video. This is avoided by manual cropping of the image at the pre-processing stage. Any random errors in the curvature data frames due to stray pixels were removed if they fell outside the 95 percentile of the mean curvature value.

## 6.6 Results

In this investigation the change in curvature of the a-Si/Kapton cantilever under an applied voltage of 5kV was tested separately with an ambient (22Lux) and an illuminated lighting condition (36kLux). The voltage was applied after a 10 second off period for 30 seconds and the lighting condition was held constant throughout each test. It was found during initial testing that after zipping the two electrodes would not return to their starting position for a up to 5 minutes after the voltage was removed. This extended ‘peel off’ time is likely due to the high molecular density of the polyimide (Kapton) substrate [34]. A high molecular density has been shown to cause a material to have a high polarisability, which correlates to a higher dielectric relaxation time [109]. This means there is a larger relaxation time for the polyimide substrate to return to its un-polarised state after the applied voltage is removed leading to the two electrodes remaining in contact for an extended period after actuation is completed. In testing it was found that this ‘peel off’ time ranged from 15 to 40 seconds. The actuator was left for 30 minutes between tests to reduce the impact of polarisation of the a-Si/Kapton cantilever.

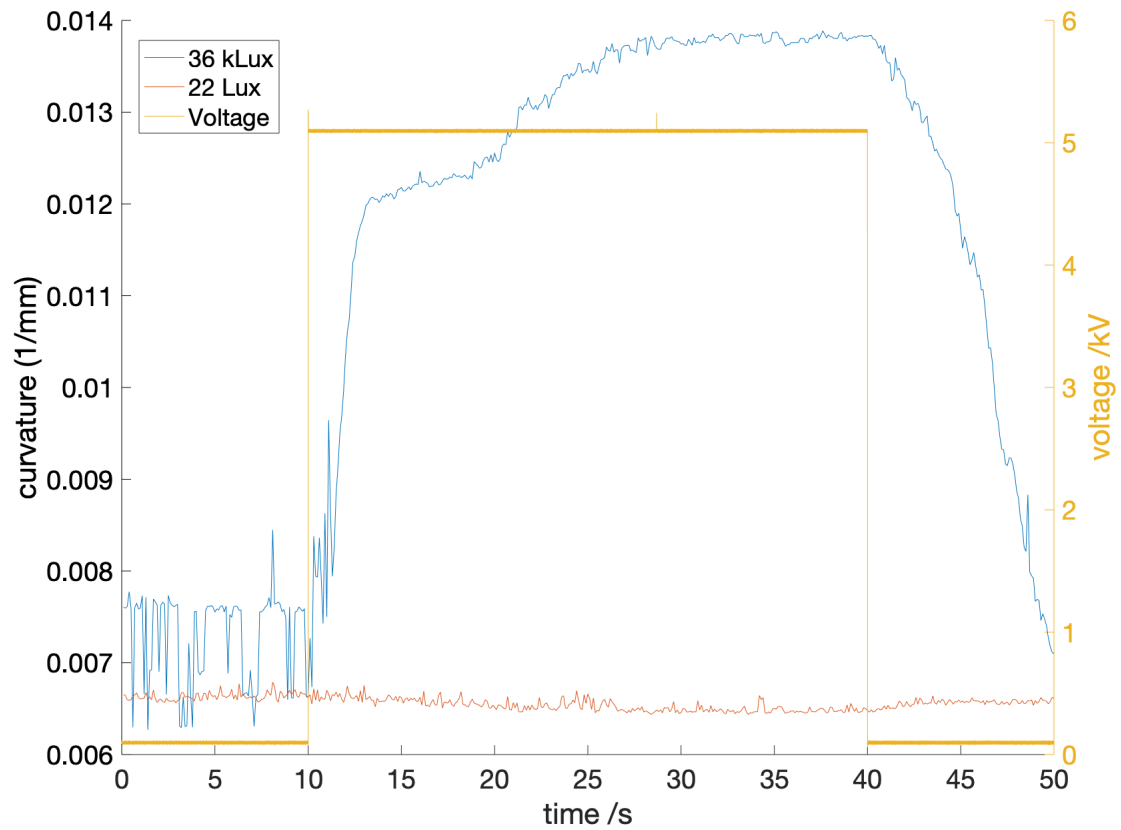


Figure 6.9: A plot showing the mean change in curvature of the a-Si/Kapton electrode under an applied voltage of 5kV in illuminated (36kLux, blue) and ambient (22Lux, orange) conditions from four tests.

Figure 6.9 shows the mean change in curvature for the a-Si cantilever under illuminated (36kLux) and ambient conditions (22Lux) from four repeated actuation cycles with standard deviations of  $0.0027\text{mm}^{-1}$  and  $7.5 \times 10^{-5}\text{mm}^{-1}$  respectively. As can be seen from figure 6.9, under at 36kLux the curvature of the positive electrode varies for the first 10 seconds due to slight movements in the a-Si/Kapton electrode after which a large increase is observed due to the application of 5kV, leading to a maximum increase in curvature of around  $0.007\text{mm}^{-1}$ . As the charges on the actuator settle over the 30 second period this curvature increases slightly, which may be due to polarisation of the Kapton. The curvature of the actuator falls when the high voltage is removed at 40 seconds. Evidence of polarisation of the polyimide substrate is seen since the actuator takes 10 seconds to return to the same curvature value as the start of the test. This slow return is likely due to the high polarisability of the polyimide (Kapton) substrate of the positive electrode causing it to hold residual charge for an extended time period after the voltage has been removed. Under ambient conditions negligible change in curvature is observed over the course of the test.

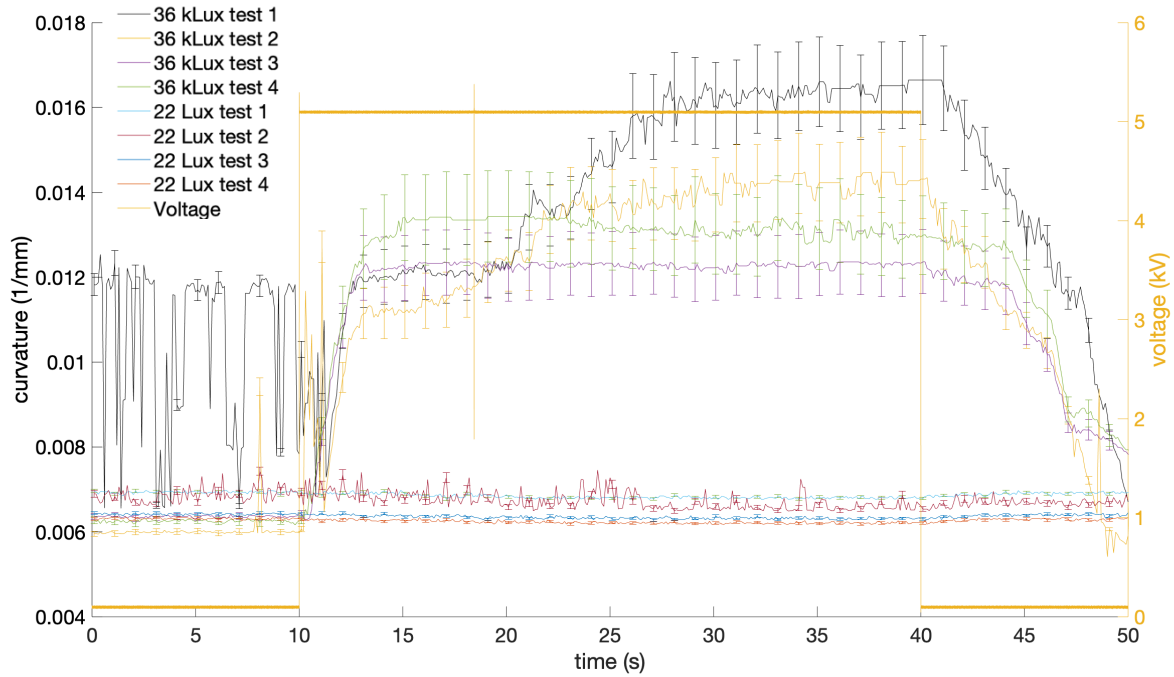


Figure 6.10: A plot showing the change in curvature of the a-Si/Kapton electrode under an applied voltage of 5kV in illuminated conditions (36kLux) and ambient conditions (22Lux) for four tests. The error bars are set to the error in the circle fit used to measure the curvatures of the electrode.

Figure 6.10 shows the curvature change for each of the four tests under illuminated conditions (36kLux) and ambient conditions (22Lux). As can be seen from figure 6.10 the actuation of the a-Si cantilever at 36kLux is inconsistent between tests, with the change in curvature varying between each repeated actuation. This could potentially be due to the residual curvature of the electrode leading to inconsistent zipping of the actuator. As the actuator is recorded from the side, any movement of the electrode in that plane (i.e. twisting) would not be represented in the plot shown in figure 6.10. The mean root-mean square error from the circle fitting algorithm for 22Lux was found to be  $0.013\text{mm}^{-1}$  with a standard deviation of  $7.05 \times 10^{-5} \text{mm}^{-1}$  across the four tests. For the tests at 36kLux the root-mean square error was  $0.0066\text{mm}^{-1}$  with a standard deviation across the four tests of  $0.0027\text{mm}^{-1}$ .

## 6.7 Discussion

This investigation shows that it is possible to develop a compliant electrostatic actuator design integrating functional materials as a method of remote and autonomous control. It was shown that by changing the environmental light intensity a 30% change in curvature of the actuator was seen, suggested there could be applications of a-Si based deployable structures. It has been demonstrated in this investigation that a thin and compliant structure can be activated by a light-dependent control system that is separated from the power supply of the actuator. An example of the use of this could be in deployable satellite panels where the change in light intensity from the satellite turning into the sun

during orbit can be used to trigger the deployment of the structure. Being able to separate the power from the control for this actuator opens up a number of opportunities that are not available to other zipping actuators such as the DLZ and the HAZEL designs.

One of the observations made in this investigation was the polarisation of the polyimide substrate leading to increased relaxation times of the actuator. This would be an issue if higher frequencies of actuation were required. However, if higher frequencies were required this could be achieved by either having a restoring force returning the positive electrode back to the starting position or by using a method of actuation that does not require the a-Si cantilever to fully zip. An example of this would be a simple powered oscillator. Alternative substrate materials to Kapton could be considered in future work with lower polarisability, however they must also have a high glass transition temperature to withstand the deposition process of a-Si, deposition of a-Si.

#### 6.8 a-Si Kapton oscillator

The cantilever a-Si actuator can be adapted to generate an oscillatory response driven by a higher frequency driving signal. The use of a higher frequency input voltage signal reduces the risk of polarisation in the Kapton layer. In addition, by using an actuator that operates at higher frequencies it is also possible to explore the use of resonance to achieve greater actuation.

##### 6.8.1 Manufacturing

The a-Si cantilever and the a-Si oscillator share a common design, but the oscillator has two differences: a longer a-Si/Kapton positive electrode is used with a length of 50mm, two small magnetic weights (0.9g total) are added to the positive electrode to form a pendulum. The magnetic properties of the weights create a negligible biasing force towards the steel shim of the actuator during oscillation as the distance between the magnets and the shim remains larger.

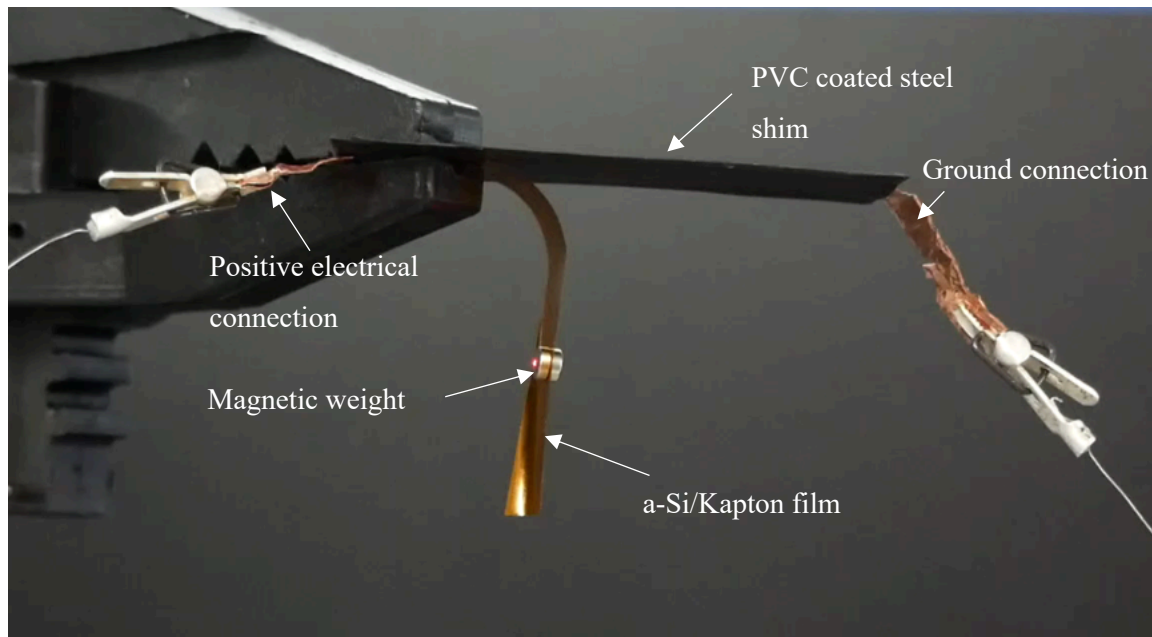


Figure 6.11: Image of the a-Si oscillator showing the steel shim negative electrode and the positive a-Si/Kapton pendulum.

Figure 6.11 shows the experimental set up for testing the a-Si oscillator, with the oscillator clamped at the initial zipping point and held in place by a clamp stand. The positive a-Si/Kapton electrode was left to hang vertically, and two small magnetic weights were attached to the centre of the electrode to create a pendulum mass. These magnetic weights were used as the magnetic force would hold them in place and would not require extra mountings that could inhibit actuation. The actuator was then connected to a high voltage supply using copper contacts. The displacement of the positive electrode was measured using a laser displacement meter which was focused on the magnetic weights (red dot in figure 6.11). A small angle assumption is made, whereby the arc movement of the pendulum can be assumed to be a near linear translation due to the change in angle of the pendulum remaining small during actuation.

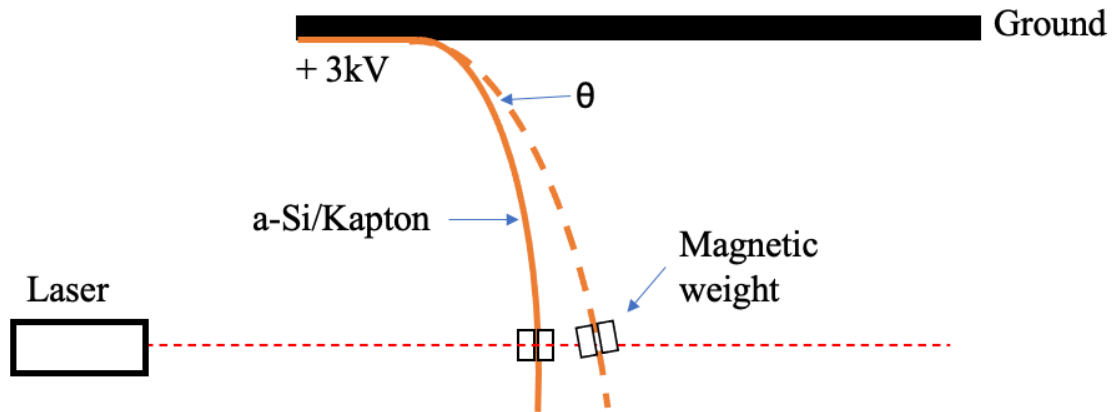


Figure 6.12: Schematic showing the experimental set up for measuring displacement of the adapted configuration for the a-Si oscillator using a small angle ( $\theta$ ) assumption.

The displacement of the a-Si oscillator was measured using a laser as shown in figure 6.12, this assumes that because the change in angle of the a-Si/Kapton electrode ( $\theta$ ) is small it can be assumed that the displacement of the oscillator is in the same plane and therefore can be measured using a laser.

### 6.8.2 Oscillator Results

The a-Si oscillator was connected to a high voltage amplifier (Ultravolt 5HV A23-BP1) and a potential difference of 3kV was applied across the actuator with a square wave input at a frequency of 2.3Hz and 50% duty cycle, which was found to be a frequency that maximized displacement for this geometry of oscillator. The current and voltage across the circuit were measured and recorded using a DAQ (National instruments BNC-2111). During the test the oscillator was held under ambient light intensity (22Lux) for 20 seconds, after which an increased light intensity of 36kLux was applied using an LED source for 10 seconds before it was removed again for a further 20 seconds in a cyclical manner.

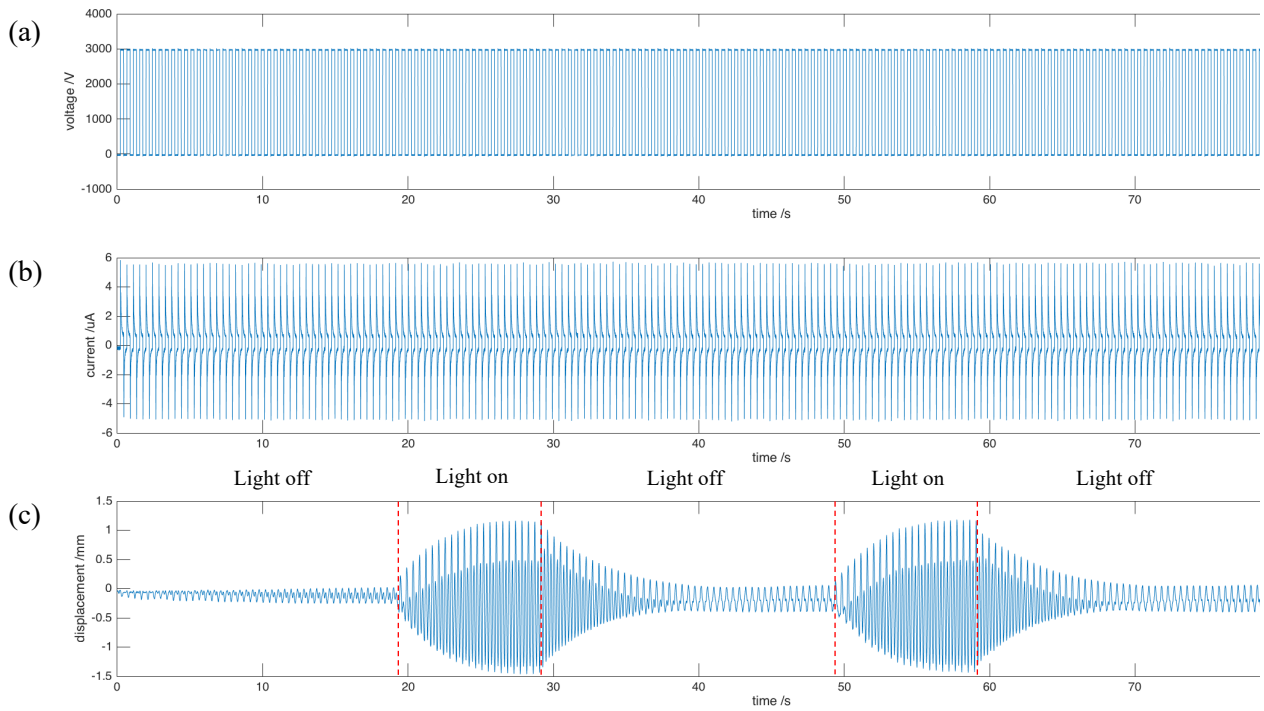


Figure 6.13: Plot of the DAQ outputs showing (a) the voltage and (b) the current measured by the DAQ during actuation and (c) the displacement measured by laser displacement.

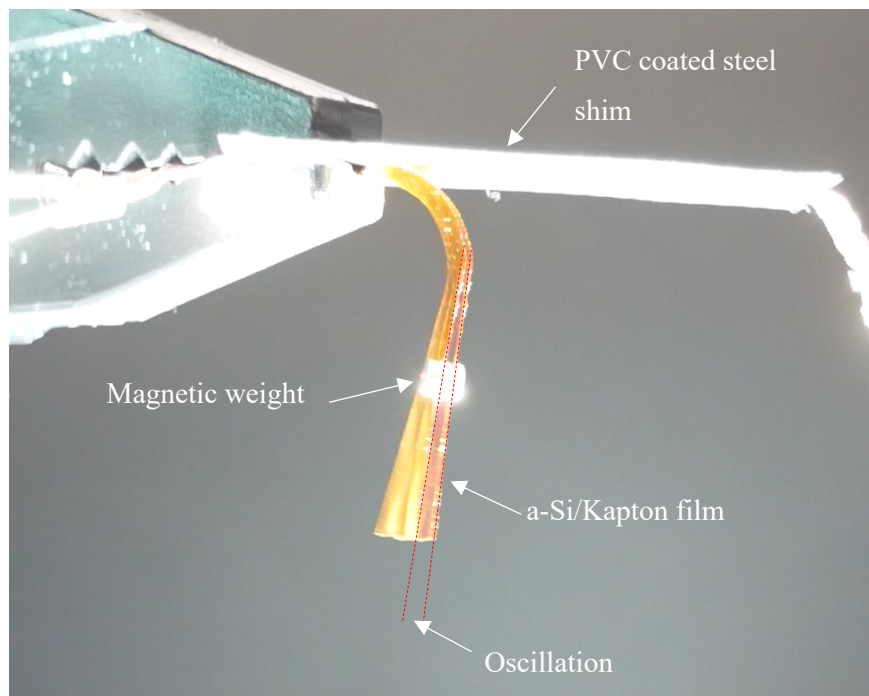


Figure 6.14: Overlaid images of the a-Si oscillator at 36kLux with an applied voltage of 3kV at a frequency of 2.3Hz.

The results recorded from the actuation of the a-Si oscillator are shown in figure 6.13. Figure 6.14 shows an overlay of the oscillator in operation under an applied light intensity of 36kLux. The applied voltage of 3kV at a frequency of 2.3Hz can be seen to lead to very little displacement of the a-Si/Kapton pendulum under ambient lighting conditions. However, once the light intensity is increased at 20 seconds the resistance change of the a-Si is sufficient to move the oscillator into resonance where we see an increase in the measured displacement of up to 1.5mm.

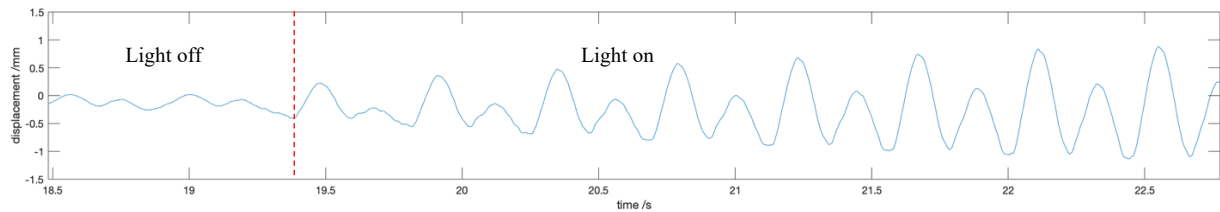


Figure 6.15: Zoomed in plot of Figure 11 (c) showing the displacement of the oscillator over time.

It can be seen from figure 6.15 that oscillator has a non-sinusoidal displacement, with different forward and backward swings. This could be due to a slight difference between the applied excitation frequency (2.3Hz) and the oscillation frequency seen in figure 6.15 of around 2.25Hz. The two distinct peaks could also be due to electrical losses through the a-Si as well as mechanical losses from the oscillator design. Once the light source is removed at 30 seconds the oscillator then begins to reduce in displacement. This causes the displacement to return to a steady lower amplitude ( $\pm 0.25$ mm) until the light intensity is increased again at 50 seconds. The actuation after 50 seconds is nearly identical to the actuation after 20 seconds.

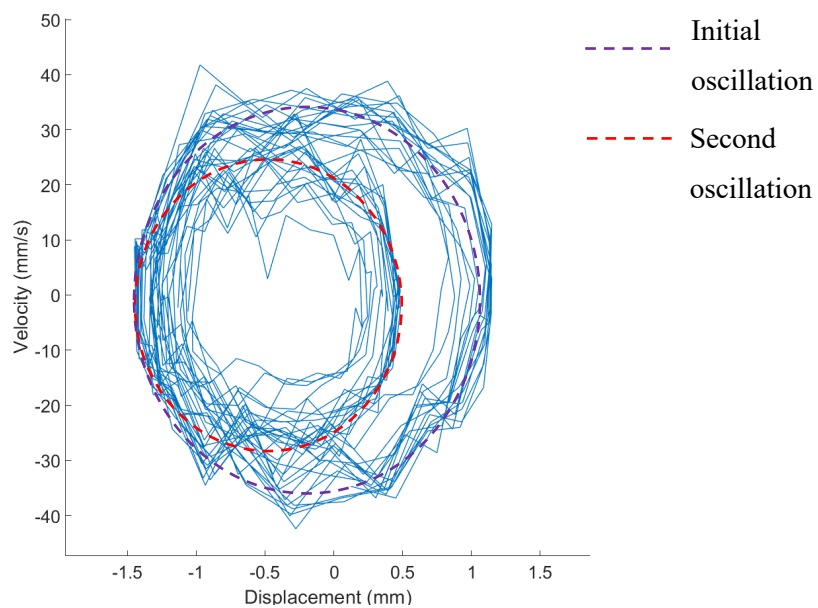


Figure 6.16: Phase plot showing the displacement against velocity of the a-Si oscillator during actuation under illuminated lighting conditions (36kLux).



Using the displacement data shown in figure 6.13 a phase plot of the actuation of the a-Si oscillator was plotted for the 36kLux condition. At the higher light intensity, evidence for resonance can be seen in figure 6.16 where there are two clear circular paths in the phase plot. The larger one represents the initial swing of the pendulum and the second circular represents the slightly damped return swing. The circular shape to this phase plot indicates that the oscillator is operating at, or near, resonance and is why a 300% increase in displacement is observed.

### 6.8.3 Oscillator Discussion

The results from the a-Si oscillator clearly demonstrate a means of achieving remote control of oscillatory actuation through the use of light intensity. It also benefits from the same integrated and compliant design as the a-Si cantilever. The key outcome of the a-Si oscillator is the demonstration of real time modulation of an oscillatory actuation response under a constant electrical driving signal. In the other actuator designs developed in this thesis it has been demonstrated that a-Si has the ability to change its resistance with light intensity. Generally, this included running a test under ambient light conditions and then running the test again under a different lighting condition. However, the a-Si oscillator tests have demonstrated the potential for real time switching between a high and low displacement output by increasing light intensity.

Being able to change between high and low displacements with low latency and repeatability demonstrated in the results above highlights the potential for a-Si as a means of light-based control. In addition, during testing the oscillator had a distinct separation between the electrical driving signal, which is continuous throughout the test, and the control signal which is modulated remotely by light intensity.

### 6.9 Future applications

The novel development of the a-Si cantilever and oscillator which both used light intensity as a trigger for actuation opens up a number of potential future applications. For example, if the concept was scaled up in size then it could be used for deployment of a folded satellite.

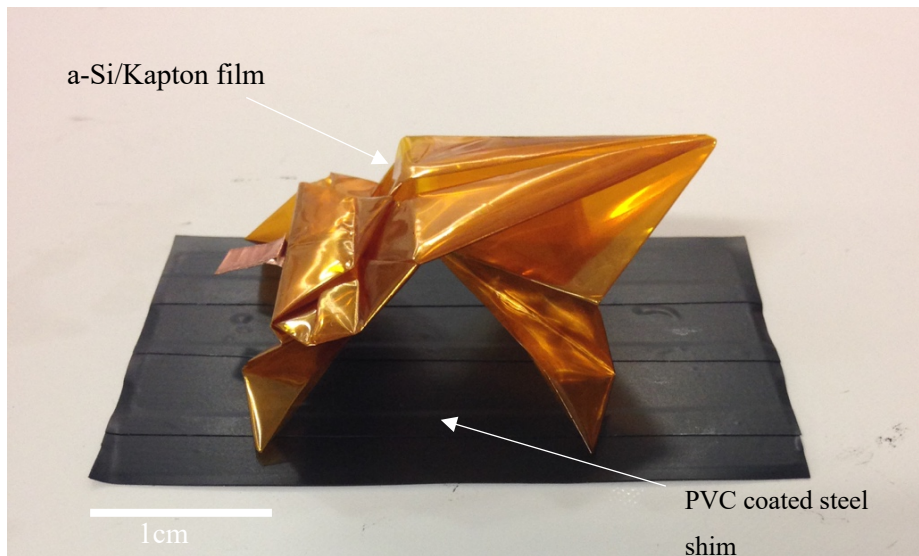


Figure 6.17: Image of a folded origami a-Si/Kapton ‘Frog’ concept with steel shim ‘Lilypad’ coated in PVC.

Figure 6.17 shows an example of a potential future folded structure using integrated a-Si deposited on to the folded thin film as a means of actuating a complex structure. It is proposed that the design for the origami frog shown in figure 6.17 utilises the actuation principles used in the a-Si cantilever and oscillator. The base would be constructed from steel shim coated in PVC to avoid shorting and to act as the negative electrode. The folded a-Si/Kapton film would then be placed on top and positively charged from an on-board power supply. The change in resistance due to increases in light intensity would cause the a-Si folded structure to be attracted to the negative electrode which would store mechanical energy in the structure that can be released when the light intensity is reduced and the ‘frog’ leaps away from the base.

Another future application looks to exploit the response of a-Si to develop a light weight four bar linkage design that can be used to respond to changes in the environmental light intensity. An example of this would be a method for autonomously actuating a solar panel to follow the path of the sun during the day to help maximise the energy output.

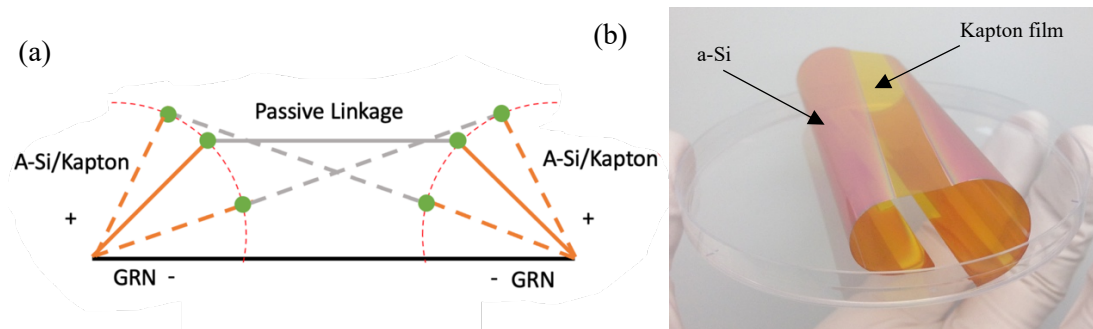


Figure 6.18: (a) Schematic of proposed four bar linkage design using two a-Si cantilevers as active linkages (the red lines show the arc of movement of the a-Si cantilevers). (b) Image of a-Si deposited on Kapton film with a central masked region with no a-Si deposited.

Figure 6.18 (a) shows a design for an autonomous method for controlling the angle of a solar panel. The solar cell would be placed on the passive linkage and two a-Si cantilevers can be used to create a four-bar linkage; this would allow for the angle of the solar cell relative to the ground to be constantly adjusted through the change in light intensity throughout the day. The length of the a-Si cantilevers can be altered to achieve larger ranges of motion and additional linkages could be added in the z-axis to increase the number of degrees of freedom achievable by the actuator. Figure 6.18 (b) shows an image of a sample of a-Si deposited on Kapton where the central section has been masked. This masking enables controlled patterning of a thin film substrate to allow for the design of complex structures with multiple optically active elements. One issue that would need to be resolved in future work would be the issue of residual curvature of the a-Si/Kapton thin film highlighted in figure 6.18 (b). This could be resolved by using a substrate material with a thermal expansion coefficient closer to that of a-Si or by utilising specialist deposition equipment that operate at lower temperatures.

## 6.10 Conclusions

In this chapter a novel actuator design has been developed that demonstrates how compliant bending actuators can exploit the optical properties of a-Si. This was done by using plasma enhanced chemical vapor deposition to manufacture thin films of a-Si (140nm thick) on a polyimide (Kapton) substrate less than 26µm in thickness. The a-Si/Kapton thin films were used to develop actuator designs based on electrostatic zipping. This addresses an aim of this PhD which is to achieve the integration of a-Si as a functional material in the body of an electrostatic actuator.

The a-Si/Kapton actuator design demonstrates the separation of the power supply from the control of the actuator. Typically, in a conventional actuator, such as a servo, the actuation would be controlled through modulating the applied power signal. By using a-Si as an optical switch in these electrostatic actuators it is possible to trigger actuation remotely as well as autonomously by either applying a light source to the actuator or using changes in the environmental light intensity respectively. This was done

without the need to change the electrical signal applied to the actuator, allowing the actuator to be controlled remotely. The separation of power and control opens up many future research opportunities. For example, it could allow for multiple actuators in a system to be controlled individually with light whilst maintaining the same power supply. This could be implemented by using an array of LEDs that are placed over the surface of the a-Si. With careful patterning of electrodes using lithography it could be possible to ‘activate’ different areas of the a-Si using different LEDs in the array. Each LED could correspond to a different actuator and therefore allow control of multiple actuators with a single a-Si device.

The a-Si/Kapton actuator design was adapted to operate as an oscillator that was able to increase its displacement by 300% under increased light intensity. This shows that it is possible to use an a-Si electrode embedded on an actuator to react to changes in light intensity whilst a constant power signal is applied. The increase in light intensity reduces the resistance of the a-Si, allowing for an increase in displacement. When the light intensity reduces, the a-Si will revert back to the higher resistance and lower displacement state whilst still under an applied potential difference.

In terms of scalability there is scope to have a-Si actuators operate at larger scales however there are some limitations. Electrostatic forces typically operated best at the smaller length scales seen in this chapter and the relatively small forces produced by the a-Si cantilever could be a limitation. Due to the thin film processing used to deposit the a-Si the samples are very thin ( $\sim 25\mu\text{m}$ ) this provides compliance and therefore only the length of the devices would be able to be scaled. Other zipping actuators such as the DLZ [16] has been shown to be scalable to larger length scales. Therefore, there is scope in future research to look at the scalability of a-Si cantilever devices.

To conclude, the principle of using a-Si to modulate the output of high voltage electrostatic actuators has been expanded to integrate a-Si onto the actuator design. Demonstrating light-triggered actuation opens future applications such as deployable space structures and active solar cells. In the following chapter we will look to collate the contributions of the research conducted in this thesis and show how the research aims stated in chapter 1 have been met.

## Chapter 7: Conclusions and future work

The aim of this thesis is to explore the use of amorphous silicon (a-Si) in electrostatic actuators, with the ambition to develop a method of providing wireless control whilst maintaining the compliance and integration desired by robotic applications. The previous chapters have proposed a number of actuator designs that exploit the photo-resistive response of a-Si, including its use alongside dielectric elastomer actuators (DEAs) presented in chapters 4 and 5 as well as a stand-alone actuator in the cantilever design presented in chapter 6. This chapter looks to collate the main conclusions from this work as well as look to areas of potential future research and development.

### 7.1 Conclusion

The research aims of this PhD are presented in chapter 1, in this section we will consider each of these aims individually and determine if these were met over the course of this research.

#### 7.1.1 How can functional materials be manufactured for use with existing electrostatic actuator designs?

In this research plasma enhanced chemical vapor deposition was used to deposit amorphous silicon (a-Si) onto the surface of a desired substrate. Using a combination of characterisation techniques including scanning electron microscopy and atomic force microscopy, the selection of an appropriate substrate material was made (untreated glass) in order to ensure a high surface quality for the deposited a-Si layer. Using ellipsometry, the layer thicknesses of the a-Si samples deposited were measured along with their refractive index and absorption coefficient. Using this information, a numerical model was used to calculate the photon absorption characteristics for the deposited a-Si, allowing for predictions to be made of the theoretical lowest achievable resistance ( $278.7\Omega$ ) at a wavelength of 650nm. It was also determined that a thickness of a-Si ( $<1\mu\text{m}$ ) was needed to achieve maximum photonic absorption.

High voltage ( $\sim 3\text{kV}$ ) electrostatic actuators such as DEAs and zipping actuators have advantages such as large strains ( $>10\%$ ) but their implementation is complicated by the need for separate power connections for each independently controlled active output. Photo-responsive a-Si enables wireless control of this class of actuator. Due to the relatively high operational voltages of the electrostatic actuators selected for this PhD research, the electrical energy provided by the applied voltage difference to the a-Si would be considerably higher than that of the photonic energy used for excitation of the a-Si. Therefore, the impact of exact wavelengths and layer thicknesses of the a-Si used is less of a concern than the amount of photonic energy (light intensity) supplied to the a-Si. Future work could look to explore the effects of varying wavelengths and layer thickness of a-Si, which could be valuable in lower voltage applications. In chapter 3 a number of characterisation techniques were implemented, and the

conclusion was made that a-Si has can be used with higher voltage actuators such as DEAs. This was then realised in chapter 4 where a-Si samples were deposited and then tested alongside a DEA actuator.

### 7.1.2 Can a-Si cope with the high voltage requirements of DEAs?

One of the key issues facing the integration of functional materials with DEAs is the high operational voltages required. This aim was met by demonstrating proof of concept experiments for using a-Si in series with a DEA in chapter 4 and integrating a-Si into a stand-alone zipping actuator in chapter 6. These actuators had operational voltages between 3 and 5kV. The a-Si samples tested in chapter 3 were imaged using a scanning electron microscope. The a-Si layer in the samples showed no sign of damage but there was evidence of damage to the gold electrodes from electrical breakdown, showing that a-Si was capable of withstanding use at the high voltages required for DEAs. This is in contrast to traditional photo-responsive electrical components such as the light dependent resistors tested in chapter 3 which were unable to withstand the higher operational voltages. This then led to follow-on research presented in chapter 4 where initial proof of concept experiments performed with a light controlled DEA with a-Si was presented and in chapter 5 where wrinkling instabilities in the DEAs were exploited to achieve larger actuations.

### 7.1.3 How can we use the photo resistive characteristics of a-Si for actuator applications?

In chapters 4, 5 and 6 the photo resistive properties of a-Si demonstrated in chapter 3 were used as a method of activating electrostatic actuators. A design for an optically controlled DEA was developed showing a displacement of the order of microns when applied with a light intensity of 51kLux. The voltage swing across the DEA due to the change in resistance of a-Si was calculated to be 865V. The proof of concept experiments presented in chapter 4 demonstrated that activation of a DEA using change in light intensity applied to a-Si was possible, however the magnitude of displacement was small for robotic actuator applications.

The actuation from the optically controlled DEA was improved in chapter 5 by controlling the geometry of the DEA to exploit wrinkling instabilities to increase actuation. In this chapter the change in resistance of a-Si due to changes in light intensity increased actuation by 16% between ambient and illuminated lighting conditions. Due to time constraints and limitations of the high voltage amplifier, the transition from stable to unstable wrinkling of the DEA membrane with a-Si was not fully captured. However, using extrapolation it was proposed that the onset of wrinkling could be triggered by a change of light intensity of 41 kLux with an applied voltage of 6kV.

Finally, it was also demonstrated that the photo resistive capabilities of a-Si can be used as an integrated electrode in an electrostatic actuator to allow for activation through changes in light intensity. This was

demonstrated successfully in chapter 6 with the a-Si cantilever and oscillator actuators designs which both used a-Si thin films.

#### 7.1.4 What is the potential control available through the use of a-Si as a photo-resistive element?

As discussed in this thesis there were two concepts of control proposed using a-Si. In this work both light triggered actuation in the optically controlled DEA and a-Si cantilever, and actuation through changes in environmental light intensity in the a-Si oscillator, have been presented. This was initially demonstrated with the optically controlled DEA which showed that by changing the environmental light intensity between tests it was possible to achieve increases in actuation. This was also demonstrated in the a-Si cantilever actuator where changes in light intensity between tests were shown to increase actuation.

Real-time triggering of actuation was shown with the a-Si oscillator where a transition between high and low amplitude oscillations under a 2.3Hz square wave voltage signal was demonstrated by the application and removal of a high intensity light source. This also led to a key outcome of this thesis which was the demonstration of the separation of power and control signals through the use of a-Si. It was shown from the a-Si oscillator that remote control of the actuator can be achieved through an applied light source whilst the input power signal remained constant. This leads to opportunities in remote control of actuators as well as actuators that can respond autonomously to changes in the environmental light intensity, circumventing the need for control through a varied power signal. The separation of power and control signals could reduce losses by removing the need for electrical components such as transformers and relays to control the actuation. However, there are clearly limitations in electrical efficiencies under the constant power supply used for the a-Si actuators in this work.

#### 7.1.5 How can a-Si be integrated into a compliant actuator design?

In this research it has been demonstrated through the use of thin film deposition that it is possible to deposit layers of a-Si that are compliant enough to be integrated into electrostatic actuators. This was exemplified by the use of a high temperature polyimide (Kapton) substrate that allowed for thin 0.14 $\mu\text{m}$  layers of a-Si to be deposited on the polymer surface. There was an issue with curling of the film in manufacturing due to differences in thermal expansion coefficients between the a-Si and the Kapton substrate. This issue was mitigated through the design of the cantilever and oscillator actuators which exploited this slight curvature. In these actuators the a-Si was used directly as the positive electrode in the actuator design and goes beyond the previous optically controlled DEAs by integrating the a-Si onto the actuator body as an electrode, whilst still maintaining a degree of structural compliance. Through

the compliant a-Si cantilever and oscillator, a means of integrating a-Si as an active component in an actuator design has been shown.

## 7.2 Discussion and future work

In this work initial steps were taken to investigate the use of functional materials for electrostatic actuators. As the work covered in this thesis is preliminary research, there are opportunities for future research. A number of these potential areas highlighted during this research are discussed below.

### 7.2.1 Limitations

Limitations of the optical control of electrostatic actuators using a-Si include the curling of the a-Si thin film electrodes as well as other unresolved questions such as the control fidelity that is capable with a-Si. The curling of the a-Si/Kapton thin films was less of an impact on the cantilever and oscillator designs presented in chapter 6 as the inherent curvature generates a restoring force in the electrode to return to its starting position after actuation. However, in other discussed designs the curvature of the a-Si/Kapton electrodes will cause significant limitations, such as in the case of a four-bar linkage. To reduce the curvature future work could focus on the use of lower temperature deposition processes for a-Si to reduce the impact of the mismatch in thermal expansion coefficients. Alternatively, future work can focus on the use of other high temperature flexible substrates with a closer thermal expansion coefficient to that of a-Si.

In this thesis largely binary methods of control have been used with a-Si, where the actuator is either on or off. From the current response of a-Si to light intensity shown in chapter 3, there is an opportunity for future work to focus on developing the non-binary control of an electrostatic actuator. One area that is yet to be explored is the fidelity of this control i.e., how precisely can the electrostatic actuator be controlled by varying the light intensity applied to the a-Si.

As highlighted in the characterisation of a-Si in chapter 3 a limitation of this material is the operational voltage range. Due to the high inherent resistance of the a-Si under ambient lighting conditions, it was shown to be most effective for control of electrostatic actuators with higher operational voltages (DEAs). Future work could look to develop upon the a-Si samples deposited on ITO for control of actuators with lower operational voltages.

### 7.2.2 Theory of a-Si and high voltage

The high voltage response of a-Si is largely unexplored in the literature. From the initial results of experimental testing of a-Si at high voltage, a hypothesis was made about how the material would behave in chapter 3.7.9. The higher energy under high potential difference could lead to greater polarisation of the crystallographic dipoles in the a-Si and increase the overall conductivity. Discussions



were also made with regards to the difference in input energy between the high electrical energy applied to the a-Si and the photonic energy applied which would be considerably less. Therefore, future work could focus on gaining a better understanding of the physics of a-Si under these applied voltage ranges. This will help to provide a better understanding of the response presented in this thesis and will help further develop optically controlled actuators.

#### 7.2.3 Exploration of other parameters of light for low voltage applications.

This work has focused on the use of light intensity for controlling the response of DEAs and electrostatic zipping actuators with a-Si. Due to the relatively high applied voltages needed for DEAs in this work, the most effective parameter to modulate actuation was the intensity of light as it provided the greatest changes in resistance of a-Si. However, as highlighted in the optical characterisation of a-Si in chapter 3 there is scope to investigate the effects of wavelength and signal frequency. There is a trend in research of reducing the operational voltage of electrostatic actuators and therefore there is scope for development of a-Si research to provide methods of control suited to lower voltage applications.

#### 7.2.4 Optically controlled wrinkling instabilities in DEAs.

In chapter 5 characterisation of voltage-induced DEA wrinkling was used to predict the point at which wrinkling instabilities would occur for an optically controlled DEA with a-Si. In future work this hypothesis could be tested to potentially demonstrate the use of changes in light intensity as a means of controlling a transition from stable to unstable actuation. This would not only demonstrate a potential method of achieving large deformations from an optically controlled DEA but it will open up potential research in using a-Si as a means to exploit bi-stability of structures to achieve large displacements through snap-through like responses

#### 7.2.5 Electromechanically coupled multiphysics modeling of a-Si actuators

A potential area of future research would include the use of multiphysics finite element modeling software such as COMSOL to help support the results for the a-Si cantilever proposed in chapter 6. A multiphysics FEA model could be used to couple the electrical properties and mechanical properties of the a-Si/Kapton thin film and predict the force output of the actuator with a higher degree of accuracy than the point charge model discussed in chapter 6.3.

#### 7.2.6 Development of thin film structures with multiple degrees of freedom

One of the novel contributions of this work was the proposal of electrostatic actuators that integrate a-Si as an active component in the actuator body. To achieve this, thin films of a-Si on flexible polyimide (Kapton) substrates were developed to allow for integration whilst maintaining compliance. It was also demonstrated that through the use of masking, there is scope to pattern a thin film with functional areas

of a-Si. There is potential for future research into more complex structures with higher degrees of freedom. Examples of this could include origami-based structures that could use a-Si to help develop optically controlled folds, and larger structures such as the ‘teetering table design’ proposed in figure 6.7.

## References

- [1] H. Schlicke, D. Battista, S. Kunze, C. J. Schröter, M. Eich, and T. Vossmeier, “Freestanding Membranes of Cross-Linked Gold Nanoparticles: Novel Functional Materials for Electrostatic Actuators,” *ACS Appl. Mater. Interfaces*, vol. 7, no. 28, pp. 15123–15128, 2015.
- [2] M. Pilz da Cunha, S. Ambergen, M. G. Debije, E. F. G. A. Homburg, J. M. J. den Toonder, and A. P. H. J. Schenning, “A Soft Transporter Robot Fueled by Light,” *Adv. Sci.*, vol. 1902842, pp. 1–7, 2020.
- [3] K. Chubb, D. Berry, and T. Burke, “Towards an ontology for soft robots: What is soft?,” *Bioinspiration and Biomimetics*, vol. 14, no. 6, 2019.
- [4] C. Laschi, B. Mazzolai, and M. Cianchetti, “Soft robotics: Technologies and systems pushing the boundaries of robot abilities,” *Sci. Robot.*, vol. 1, no. 1, p. eaah3690, 2016.
- [5] M. Wehner *et al.*, “An integrated design and fabrication strategy for entirely soft, autonomous robots,” *Nature*, vol. 536, no. 7617, pp. 451–455, 2016.
- [6] A. D. Marchese and D. Rus, “Design, kinematics, and control of a soft spatial fluidic elastomer manipulator,” *Int. J. Rob. Res.*, vol. 35, no. 7, pp. 840–869, 2016.
- [7] R. F. Shepherd *et al.*, “Multigait soft robot,” *Proc. Natl. Acad. Sci.*, vol. 108, no. 51, pp. 20400–20403, 2011.
- [8] E. Steltz, A. Mozeika, N. Rodenberg, E. Brown, and H. M. Jaeger, “JSEL: Jamming skin enabled locomotion,” in *2009 IEEE/RSJ International Conference on Intelligent Robots and Systems, IROS 2009*, 2009, pp. 5672–5677.
- [9] P. Ohta *et al.*, “Design of a Lightweight Soft Robotic Arm Using Pneumatic Artificial Muscles and Inflatable Sleeves,” *Soft Robot.*, vol. 5, no. 2, pp. 204–215, 2018.
- [10] W. McMahan *et al.*, “Field trials and testing of the OctArm continuum manipulator,” *Proceedings - IEEE International Conference on Robotics and Automation*, vol. 2006, pp. 2336–2341, 2006.
- [11] A. Albu-Schäffer *et al.*, “Soft Robotics: From Torque Feedback Controlled Lightweight Robots to Intrinsically Compliant Systems,” *Robot. Res.*, vol. 70, pp. 185–207, 2011.
- [12] R. Ham, T. Sugar, B. Vanderborght, K. Hollander, and D. Lefeber, “Compliant actuator designs,” *IEEE Robot. Autom. Mag.*, vol. 16, no. 3, pp. 81–94, 2009.
- [13] F. Carpi, D. De Rossi, R. Kornbluh, R. Pelrine, and P. Sommer-Larsen, *Dielectric Elastomers as Electromechanical Transducers*, vol. 23, no. 6. California: Elsevier, 2008.
- [14] S. Seok, C. D. Onal, K. J. Cho, R. J. Wood, D. Rus, and S. Kim, “Meshworm: A peristaltic soft robot with antagonistic nickel titanium coil actuators,” *IEEE/ASME Trans. Mechatronics*, vol. 18, no. 5, pp. 1485–1497, 2013.
- [15] B. Tondu, “Modelling of the McKibben artificial muscle: A review,” *J. Intell. Mater. Syst. Struct.*, vol. 23, no. 3, pp. 225–253, 2012.

- [16] M. Taghavi, T. Helps, and J. Rossiter, "Electro-ribbon actuators and electro-origami robots," *Sci. Robot.*, vol. 3, no. 25, p. eaau9795, Dec. 2018.
- [17] N. Kellaris, V. G. Venkata, G. M. Smith, S. K. Mitchell, and C. Keplinger, "Peano-HASEL actuators: Muscle-mimetic, electrohydraulic transducers that linearly contract on activation," *Sci. Robot.*, vol. 3, no. 14, pp. 1–11, 2018.
- [18] P. Martins, D. Correia, V. Correia, and S. Lanceros-Mendez, "Polymer-based actuators: Back to the future," *Phys. Chem. Chem. Phys.*, vol. 19, 2020.
- [19] A. T. Conn and J. Rossiter, "Harnessing electromechanical membrane wrinkling for actuation," *Appl. Phys. Lett.*, vol. 101, no. 17, pp. 1–5, 2012.
- [20] F. Carpi *et al.*, "Standards for dielectric elastomer transducers," *Smart Mater. Struct.*, vol. 24, no. 10, p. 105025, 2015.
- [21] S. Bauer, S. Bauer-Gogonea, I. Graz, M. Kaltenbrunner, C. Keplinger, and R. Schwödiauer, "25th anniversary article: A soft future: From robots and sensor skin to energy harvesters," *Adv. Mater.*, vol. 26, no. 1, pp. 149–162, 2014.
- [22] P. Brochu and Q. Pei, "Advances in dielectric elastomers for actuators and artificial muscles," *Macromol. Rapid Commun.*, vol. 31, no. 1, pp. 10–36, 2010.
- [23] X. Ji *et al.*, "Stretchable composite monolayer electrodes for low voltage dielectric elastomer actuators," *Sensors Actuators B Chem.*, vol. 261, pp. 135–143, May 2018.
- [24] R. E. Pelrine, R. D. Kornbluh, and J. P. Joseph, "Electrostriction of polymer dielectrics with compliant electrodes as a means of actuation," *Sensors Actuators, A Phys.*, vol. 64, no. 1, pp. 77–85, 1998.
- [25] P. Lotz, M. Matysek, and H. F. Schlaak, "Peristaltic pump made of dielectric elastomer actuators," vol. 7287, p. 72872D, 2009.
- [26] C. Cao, X. Gao, and A. T. Conn, "A Magnetically Coupled Dielectric Elastomer Pump for Soft Robotics," *Adv. Mater. Technol.*, vol. 4, no. 8, pp. 1–6, 2019.
- [27] I. A. Anderson, T. A. Gisby, T. G. McKay, B. M. O'Brien, and E. P. Calius, "Multi-functional dielectric elastomer artificial muscles for soft and smart machines," *J. Appl. Phys.*, vol. 112, no. 4, 2012.
- [28] M. P. Brenner, J. H. Lang, J. Li, and A. H. Slocum, "Optimum design of an electrostatic zipper," vol. 2, no. 1, pp. 371–374, 2004.
- [29] J. Li, "Electrostatic Zipping Actuators and Their Application to MEMS," Massachusetts Institute of Technology, 2004.
- [30] L. Maffli, S. Rosset, and H. R. Shea, "Zipping dielectric elastomer actuators: Characterization, design and modeling," *Smart Mater. Struct.*, vol. 22, no. 10, 2013.
- [31] M. Schenk and S. D. Guest, "Origami folding: A structural engineering approach," *Origami 5 Fifth Int. Meet. Origami Sci. Math. Educ.*, pp. 1–16, 2011.
- [32] P. Rothemund, N. Kellaris, and C. Keplinger, "How inhomogeneous zipping increases the

- force output of Peano-HASEL actuators,” *Extrem. Mech. Lett.*, vol. 31, p. 100542, 2019.
- [33] C. Jin *et al.*, “Tunable, Flexible, and Resilient Robots Driven by an Electrostatic Actuator,” *Adv. Intell. Syst.*, vol. 2, no. 3, p. 1900162, 2020.
- [34] C. Cao, X. Gao, J. Guo, and A. Conn, “De-electroadhesion of flexible and lightweight materials: An experimental study,” *Appl. Sci.*, vol. 9, no. 14, 2019.
- [35] K. Yao, W. Zhu, K. Uchino, Z. Zhang, and L. C. Lim, “Design and fabrication of a high performance multilayer piezoelectric actuator with bending deformation,” *IEEE Trans. Ultrason. Ferroelectr. Freq. Control*, vol. 46, no. 4, pp. 1020–1027, 1999.
- [36] S. Kawakita, T. Isogai, N. Ohya, and N. Kawahara, “Multi-layered piezoelectric bimorph actuator,” *MHS 1997 - Proc. 1997 Int. Symp. Micromechatronics Hum. Sci.*, pp. 73–78, 1997.
- [37] S. Datta, “Piezoelectric Materials: Crystal Orientation and Poling Direction,” *COMSOL Blog*, 2020. [Online]. Available: <https://www.comsol.com/blogs/piezoelectric-materials-crystal-orientation-poling-direction/>. [Accessed: 04-Aug-2020].
- [38] E. V. Ardelean, D. G. Cole, and R. L. Clark, “High performance ‘V-stack’ piezoelectric actuator,” *J. Intell. Mater. Syst. Struct.*, vol. 15, no. 11, pp. 879–889, 2004.
- [39] R. K. Jain, S. Majumder, B. Ghosh, and S. Saha, “Design and manufacturing of mobile micro manipulation system with a compliant piezoelectric actuator based micro gripper,” *Journal of Manufacturing Systems*, vol. 35, pp. 76–91, 2015.
- [40] O. A. Bauchau and J. I. Craig, “Euler-Bernoulli beam theory,” 2009, pp. 173–221.
- [41] S. Kim, C. Laschi, and B. Trimmer, “Soft robotics: A bioinspired evolution in robotics,” *Trends Biotechnol.*, vol. 31, no. 5, pp. 287–294, 2013.
- [42] V. H. Le *et al.*, “A soft-magnet-based drug-delivery module for active locomotive intestinal capsule endoscopy using an electromagnetic actuation system,” *Sensors Actuators, A Phys.*, vol. 243, pp. 81–89, 2016.
- [43] L. Zhang, J. J. Abbott, L. Dong, B. E. Kratochvil, D. Bell, and B. J. Nelson, “Artificial bacterial flagella: Fabrication and magnetic control,” *Appl. Phys. Lett.*, vol. 94, no. 6, pp. 13–15, 2009.
- [44] Y. Kim, H. Yuk, R. Zhao, S. A. Chester, and X. Zhao, “Printing ferromagnetic domains for untethered fast-transforming soft materials,” *Nature*, vol. 558, no. 7709, pp. 274–279, 2018.
- [45] X. Zhao and Y. Kim, “Soft microbots controlled by nanomagnets,” *Nature*, vol. 575, p. 59, 2009.
- [46] Unknown, “Re-configurable mold for complex surfaces using shape memory alloys.” [Online]. Available: <http://fab.cba.mit.edu/classes/961.04/people/will/proposal.htm>. [Accessed: 04-Aug-2020].
- [47] A. Menciassi, S. Gorini, G. Pernorio, and P. Dario, “A SMA actuated artificial earthworm,” *Proc. - IEEE Int. Conf. Robot. Autom.*, vol. 2004, no. 4, pp. 3282–3287, 2004.
- [48] T. Saito, T. Kagiwada, and H. Harada, “Development of an earthworm robot with a shape

- memory alloy and braided tube,” *Adv. Robot.*, vol. 23, no. 12–13, pp. 1743–1760, 2009.
- [49] A. Menciassi, S. Gorini, G. Pernorio, W. Liu, F. Valvo, and P. Dario, “Design, fabrication and performances of a biomimetic robotic earthworm,” *Proc. - 2004 IEEE Int. Conf. Robot. Biomimetics, IEEE ROBIO 2004*, pp. 274–278, 2004.
- [50] A. Menciassi, D. Accoto, S. Gorini, and P. Dario, “Development of a biomimetic miniature robotic crawler,” *Auton. Robots*, vol. 21, no. 2, pp. 155–163, 2006.
- [51] S.-M. Kirsch, F. Welsch, M. Schmidt, P. Motzki, and S. Seelecke, “Bistable SMA Vacuum Suction Cup,” in *ACTUATOR 2018: 16th International Conference on New Actuators*, 2018, no. June, pp. 25–27.
- [52] B. S. R Dornhaus, G Nimtz, *Narrow-Gap Semi conductors*. 2006.
- [53] N. Nasrudin, N. M. Ilis, T. P. Juin, T. T. K. Chun, L. W. Zhe, and F. Z. Rokhani, “Analysis of the light dependent resistor configuration for line tracking robot application,” *Proc. - 2011 IEEE 7th Int. Colloq. Signal Process. Its Appl. CSPA 2011*, pp. 500–502, 2011.
- [54] V. Contributors, “Amorphous silicon,” *Wikipedia*. [Online]. Available: [https://en.wikipedia.org/wiki/Amorphous\\_silicon](https://en.wikipedia.org/wiki/Amorphous_silicon). [Accessed: 04-Aug-2010].
- [55] M. Moreno *et al.*, “Amorphous, Polymorphous, and Microcrystalline Silicon Thin Films Deposited by Plasma at Low Temperatures,” in *Crystalline and Non-crystalline Solids*, InTech, 2016.
- [56] P. Y. Chiou, A. T. Ohta, and M. C. Wu, “Massively parallel manipulation of single cells and microparticles using optical images,” *Nature*, vol. 436, no. 7049, pp. 370–372, 2005.
- [57] P. Y. Chiou, A. T. Ohta, and M. C. Wu, “Massively parallel manipulation of single cells and microparticles using optical images,” *Nature*, vol. 436, no. 7049, pp. 370–372, 2005.
- [58] G. A. Swartz, “Reverse bias and heat treatment to improve performance of a-Si solar cells,” *Appl. Phys. Lett.*, vol. 44, no. 7, pp. 697–699, 1984.
- [59] T. Moehl *et al.*, “Strong photocurrent amplification in perovskite solar cells with a porous TiO<sub>2</sub> blocking layer under reverse bias,” *J. Phys. Chem. Lett.*, vol. 5, no. 21, pp. 3931–3936, 2014.
- [60] L. Furno, M. C. Nielsen, and M. Blanke, “Centralised versus Decentralised Control Reconfiguration for Collaborating Underwater Robots,” *IFAC-PapersOnLine*, vol. 48, no. 21, pp. 732–739, 2015.
- [61] N. S. Nise, *Control System Engineering*. Wiley, 2014.
- [62] R. Jander, “Insect Orientation,” *Annu. Rev. Entomol.*, vol. 8, no. 1, pp. 95–114, Jan. 1963.
- [63] G. Jékely, “Evolution of phototaxis,” *Philos. Trans. R. Soc. B Biol. Sci.*, vol. 364, no. 1531, pp. 2795–2808, Oct. 2009.
- [64] L. Yang *et al.*, “An Autonomous Soft Actuator with Light-Driven Self-Sustained Wavelike Oscillation for Phototactic Self-Locomotion and Power Generation,” *Adv. Funct. Mater.*, vol. 30, no. 15, pp. 1–13, 2020.

- [65] L. Maffli, S. Rosset, M. Ghilardi, F. Carpi, and H. Shea, “Ultrafast all-polymer electrically tunable silicone lenses,” *Adv. Funct. Mater.*, vol. 25, no. 11, pp. 1656–1665, 2015.
- [66] M. P. M. Dicker, J. M. Rossiter, I. P. Bond, and P. M. Weaver, “Biomimetic photo-actuation: Sensing, control and actuation in sun-tracking plants,” *Bioinspiration and Biomimetics*, vol. 9, no. 3, 2014.
- [67] M. Garrad, G. Soter, A. T. Conn, H. Hauser, and J. Rossiter, “A soft matter computer for soft robots,” *Sci. Robot.*, vol. 4, no. 33, 2019.
- [68] M. P. Nemitz, C. K. Abrahamsson, L. Wille, A. A. Stokes, D. J. Preston, and G. M. Whitesides, “Soft Non-Volatile Memory for Non-Electronic Information Storage in Soft Robots,” *2020 3rd IEEE Int. Conf. Soft Robot. RoboSoft 2020*, pp. 7–12, 2020.
- [69] C. Wang *et al.*, “Soft Ultrathin Electronics Innervated Adaptive Fully Soft Robots,” *Adv. Mater.*, vol. 30, no. 13, pp. 1–9, 2018.
- [70] IPC-2221, “Generic Standard on Printed Board Design,” 1998.
- [71] “Oxford Instruments Plasma pro PECVD.” [Online]. Available: <https://plasma.oxinst.com/products/pecvd/plasmapro-100-pecvd>. [Accessed: 02-Feb-2021].
- [72] G. Liu, J. B. Kerr, and S. Johnson, “Dark spot formation relative to ITO surface roughness for polyfluorene devices,” *Synth. Met.*, vol. 144, no. 1, pp. 1–6, Jul. 2004.
- [73] J. Price, P. Y. Hung, T. Rhoad, B. Foran, and A. C. Diebold, “Spectroscopic ellipsometry characterization of Hf<sub>x</sub>Si<sub>y</sub>O<sub>z</sub> films using the Cody–Lorentz parameterized model,” *Appl. Phys. Lett.*, vol. 85, no. 10, pp. 1701–1703, Sep. 2004.
- [74] J. G. Shaw, M. G. Hack, and R. A. Martin, “Metastable effects in high-voltage amorphous silicon thin-film transistors,” *J. Appl. Phys.*, vol. 69, no. 4, pp. 2667–2672, Feb. 1991.
- [75] P. G. Le Comber, “Present and future applications of amorphous silicon and its alloys,” *J. Non. Cryst. Solids*, vol. 115, no. 1–3, pp. 1–13, Dec. 1989.
- [76] “Personal corespondance with Yutian Zhang,” 2019.
- [77] J. Mistrik, S. Kasap, H. E. Ruda, C. Koughia, and J. Singh, “Optical Properties of Electronic Materials: Fundamentals and Characterization,” 2017, pp. 1–1.
- [78] C. D. Gamlath, D. M. Benton, and M. J. Cryan, “Microwave Properties of an Inhomogeneous Optically Illuminated Plasma in a Microstrip Gap,” *IEEE Trans. Microw. Theory Tech.*, vol. 63, no. 2, pp. 374–383, Feb. 2015.
- [79] M. C. Troparevsky, A. S. Sabau, A. R. Lupini, and Z. Zhang, “Transfer-matrix formalism for the calculation of optical response in multilayer systems: from coherent to incoherent interference,” *Opt. Express*, vol. 18, no. 24, p. 24715, 2010.
- [80] J. Mort, I. Chen, A. Troup, M. Morgan, J. Knights, and R. Lujan, “Nongeminate Recombination of a-Si:H,” *Phys. Rev. Lett.*, vol. 45, no. 16, pp. 1348–1351, Oct. 1980.
- [81] P. G. Le Comber, A. Madan, and W. E. Spear, “Electronic transport and state distribution in amorphous Si films,” *J. Non. Cryst. Solids*, vol. 11, no. 3, pp. 219–234, Nov. 1972.

- [82] Kelly Cheung, “Conductance from transmission,” in *Electronic Transport in Mesoscopic Systems*, Vancouver, BC, Canada, V6T1Z1: Cambridge University Press, 1995, pp. 48–116.
- [83] C. Gillespie, A. Marzo, F. Scarpa, J. Rossiter, and A. T. Conn, “High- voltage photonic switching of dielectric elastomers with amorphous silicon thin-films,” *Electroact. Polym. Actuators Devices (EAPAD)*, vol. 10966, 2019.
- [84] P. Brochu and Q. Pei, “Advances in dielectric elastomers for actuators and artificial muscles,” *Macromol. Rapid Commun.*, vol. 31, no. 1, pp. 10–36, 2010.
- [85] R. Pelrine, “High-Speed Electrically Actuated Elastomers with Strain Greater Than 100%,” *Science (80-. )*, vol. 287, no. 5454, pp. 836–839, Feb. 2000.
- [86] A. Muscle, F. Carpi, and D. De Rossi, “Dielectric Elastomers as Electromechanical Transducers,” *Dielectr. Elastomers As Electromechanical Transducers*, 2008.
- [87] A. Hinitt, “Integration and Coupling of High Performance Dielectric Elastomer Actuator Systems,” University of Bristol.
- [88] Q. Pei, M. Rosenthal, S. Stanford, H. Prahlaad, and R. Pelrine, “Multiple-degrees-of-freedom electroelastomer roll actuators,” *Smart Mater. Struct.*, vol. 13, no. 5, pp. N86–N92, Oct. 2004.
- [89] C. Keplinger, T. Li, R. Baumgartner, Z. Suo, and S. Bauer, “Harnessing snap-through instability in soft dielectrics to achieve giant voltage-triggered deformation,” *Soft Matter*, vol. 8, no. 2, pp. 285–288, 2012.
- [90] C. Cao, S. Burgess, and A. T. Conn, “Toward a Dielectric Elastomer Resonator Driven Flapping Wing Micro Air Vehicle,” *Front. Robot. AI*, vol. 5, Jan. 2019.
- [91] A. T. Conn and J. Rossiter, “Towards holonomic electro-elastomer actuators with six degrees of freedom,” *Smart Mater. Struct.*, vol. 21, no. 3, 2012.
- [92] M. Duduta, E. Hajiesmaili, H. Zhao, R. J. Wood, and D. R. Clarke, “Realizing the potential of dielectric elastomer artificial muscles,” *Proc. Natl. Acad. Sci.*, vol. 116, no. 7, pp. 2476–2481, Feb. 2019.
- [93] C. T. Nguyen *et al.*, “A novel bioinspired hexapod robot developed by soft dielectric elastomer actuators,” in *2017 IEEE/RSJ International Conference on Intelligent Robots and Systems (IROS)*, 2017, pp. 6233–6238.
- [94] C. Christianson, N. N. Goldberg, and M. T. Tolley, “Elastomeric diaphragm pump driven by fluid electrode dielectric elastomer actuators (FEDEAs),” in *Electroactive Polymer Actuators and Devices (EAPAD) XX*, 2018, p. 21.
- [95] G. Moretti, M. Righi, R. Vertechy, and M. Fontana, “Fabrication and Test of an Inflated Circular Diaphragm Dielectric Elastomer Generator Based on PDMS Rubber Composite,” *Polymers (Basel)*, vol. 9, no. 12, p. 283, Jul. 2017.
- [96] C. Keplinger, M. Kaltenbrunner, N. Arnold, and S. Bauer, “Röntgen’s electrode-free elastomer actuators without electromechanical pull-in instability,” *Proc. Natl. Acad. Sci.*, vol. 107, no. 10, pp. 4505–4510, 2010.



- [97] G. Kovacs, L. Düring, S. Michel, and G. Terrasi, “Stacked dielectric elastomer actuator for tensile force transmission,” *Sensors Actuators, A Phys.*, vol. 155, no. 2, pp. 299–307, 2009.
- [98] F. Carpi, C. Salaris, and D. De Rossi, “Folded dielectric elastomer actuators,” *Smart Mater. Struct.*, vol. 16, no. 2, 2007.
- [99] G.-K. Lau, H.-T. Lim, J.-Y. Teo, and Y.-W. Chin, “Lightweight mechanical amplifiers for rolled dielectric elastomer actuators and their integration with bio-inspired wing flappers,” *Smart Mater. Struct.*, vol. 23, no. 2, p. 025021, Feb. 2014.
- [100] A. O’Halloran, F. O’Malley, and P. McHugh, “A review on dielectric elastomer actuators, technology, applications, and challenges,” *J. Appl. Phys.*, vol. 104, no. 7, 2008.
- [101] A. T. Conn and J. Rossiter, “Smart radially folding structures,” *IEEE/ASME Trans. Mechatronics*, vol. 17, no. 5, pp. 968–975, 2012.
- [102] Y. Bar-Cohen, K. J. Kim, H. R. Choi, and J. D. W. Madden, “Electroactive polymer materials,” *Smart Mater. Struct.*, vol. 16, no. 2, Apr. 2007.
- [103] H. Godaba, Z. Q. Zhang, U. Gupta, C. C. Foo, and J. Zhu, “Instabilities in dielectric elastomers: Buckling, wrinkling, and crumpling,” *Soft Matter*, vol. 15, no. 36, pp. 7137–7144, 2019.
- [104] H. Godaba, Z. Q. Zhang, U. Gupta, C. Chiang Foo, and J. Zhu, “Dynamic pattern of wrinkles in a dielectric elastomer,” *Soft Matter*, vol. 13, no. 16, pp. 2942–2951, 2017.
- [105] J. D. Suhey, N. H. Kim, and C. Niezrecki, “Numerical modeling and design of inflatable structures - Application to open-ocean-aquaculture cages,” *Aquac. Eng.*, vol. 33, no. 4, pp. 285–303, 2005.
- [106] M. Shrestha, G.-K. Lau, and Z. Lu, “Multifunctional Smart Window based on Dielectric Elastomer Actuator,” in *Proceedings of 1st International Electronic Conference on Actuator Technology: Materials, Devices and Applications*, 2020, p. 8509.
- [107] C. Gillespie, A. Marzo, F. Scarpa, J. M. Rossiter, and A. T. Conn, “Switching of amorphous silicon thin-film actuators for optically functional robotic devices,” in *Electroactive Polymer Actuators and Devices (EAPAD) XXII*, 2020, p. 52.
- [108] S. Miyashita, S. Guitron, M. Ludersdorfer, C. R. Sung, and D. Rus, “An Untethered Miniature Origami Robot that Self-folds, Walks, Swims, and Degrades,” *2015 Ieee Int. Conf. Robot. Autom.*, pp. 1490–1496, 2015.
- [109] Z. Ahmad, “Polymer Dielectric Materials,” in *Dielectric Material*, InTech, 2012.

## Appendix

### Appendix A: ITO ramp test

Alongside the tests conducted on a-Si sample deposited on plane glass substrate voltage ramp testing was also conducted on a-Si sample deposited on ITO coated glass substrate. The samples tested were fabricated to the same specifications presented in section 3.3.1. The sample was then attached to a high voltage amplifier (Ultravolt 5HV-A23-BP1) and the current was measured using a DAQ (National instruments BNC-2111).

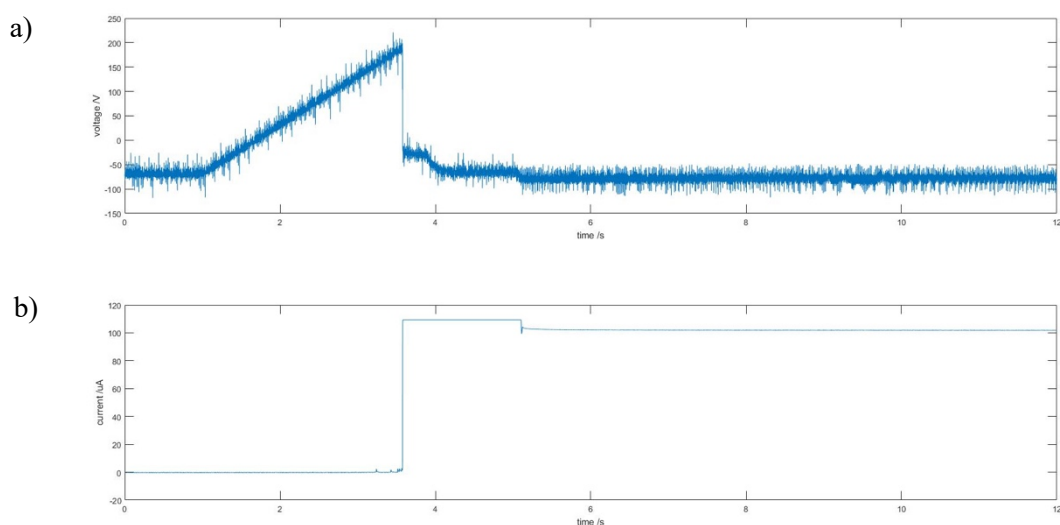


Figure A.1: a) Graph showing the applied Voltage ramp as a function of time for the a-Si sample deposited on ITO coated glass substrate. b) Graph showing the current measured by the DAQ as a function of time for the a-Si sample deposited on ITO coated glass substrate.

Figure A.1 shows the applied voltage to the a-Si/ITO sample in a) and the current recorded in by the DAQ in b). As can be seen by the graph the maximum voltage reached before electrical breakdown of the a-Si/ITO sample was just under 200V after which a sudden drop in the applied voltage in figure A.1 a) is observed with a corresponding spike in current seen in figure A.1 b) at 3.75 seconds. This spike in current shows that the sample has shorted due to an electrical breakdown. This could be due to the ITO layer on the substrate being conductive and therefore providing a path of lower resistance through the thickness of the a-Si compared to the resistance between the gold electrodes. As the applied voltage increased the potential differences between the ITO and the gold electrodes could become significant enough to lead to electrical breakdown through the thickness of the a-Si layer. From this result it was determined that ITO coated glass was not a suitable substrate for use with a-Si at higher applied voltages.

#### Appendix B: Figure 4.2 Experimental method.

The results shown in figure 4.2 are from the high voltage testing of a weighted spot DEA under an applied voltage of 3kV. The weighted spot DEA was fabricated following the same process highlighted in section 4.2.7, The DEA was then attached to a high voltage amplifier (Ultravolt 5HV-A23-BP1) and the current measurements were recorded by a DAQ (National instruments BNC-2111). The displacement of the weighted spot was measured using a laser (Keyence LK-GD152 and LK GD500).

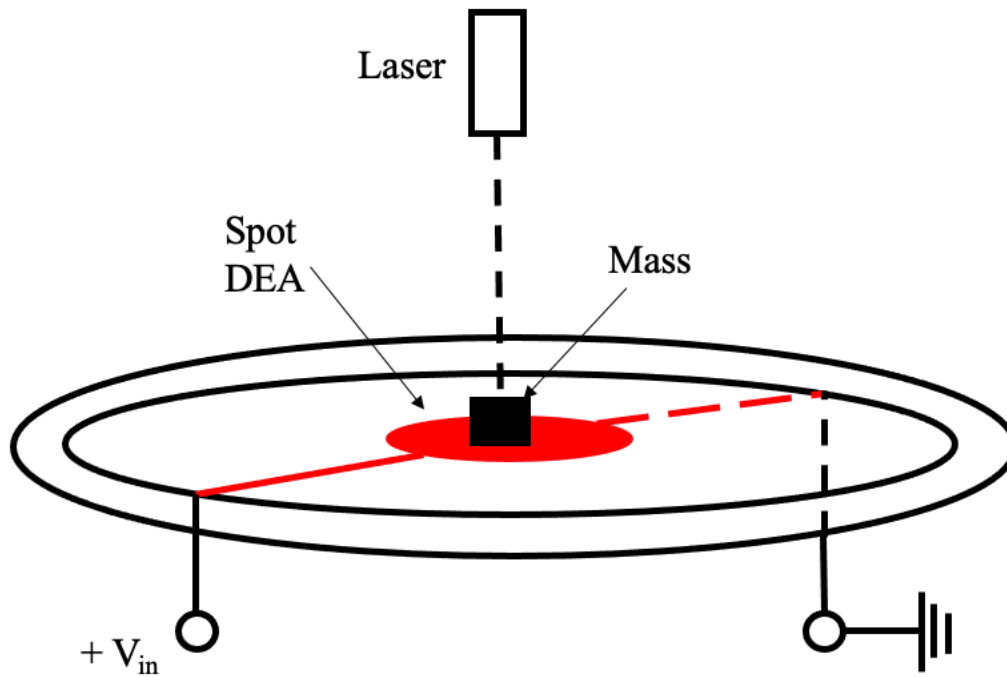


Figure B.1: Schematic showing the experimental set up of a high voltage test of a weighted spot DEA presented in figure 4.2

Figure B.1 shows the experimental set up used to produce the results shown in figure 4.2. The DEA was applied with a voltage of 3kV for a period of 5 seconds with a 2 second off period in between the applied voltage.

#### Appendix C: High frequency testing of wrinkling DEAs

To test the frequency response of the wrinkling DEAs, one of the DEAs was tested at increasing duty cycles to understand how staple the wrinkling is at longer periods of applied voltage. On concern with the unstable actuation of the DEA is that electrical breakdown would occur in the DEA at prolonged periods of applied voltage.

Table C.1: Results of testing the Wrinkling DEA at differing duty cycles

Duty cycle (seconds)	Voltage (kV)	Pass testing without failure
1/1	3.8	Pass
2/1	3.8	Pass
3/1	3.8	Pass
4/1	3.8	Pass, n.b. passive area marked with grease from membrane folding over itself
1/1	3.9	Pass
2/1	3.9	Pass
3/1	3.9	Pass
4/1	3.9	Pass

Table C.1 shows that the DEA passed all duty cycled from 1/1 to 4/1 at both 3.8 kV and 3.9kV. This shows that the unstable actuation can be used at a range of duty cycles without the risk of electrical breakdown with a maximum duty cycle of 4/1 seconds. As noted in table C.1 the membrane of the DEA did fold over itself during extended periods of applied voltage which led to smudging of the carbon grease electrode. Future work could look at the lifespan of a DEA under cyclical loading to better understand how repeatable the wrinkling of the DEAs tested in chapter 5 are, allowing for potential applications as active blinds which would require to have long periods of applied voltages alongside repeatable wrinkling of the DEA.